

TRANSVERSE ISOTROPIC EFFECT ON MECHANICAL PROPERTIES
OF GYPSUM



A Thesis Submitted in Partial Fulfillment of the Requirements for the
Degree of Doctor of Philosophy of Engineering in Civil, Transportation
and Geo-resources Engineering
Suranaree University of Technology
Academic Year 2021

ผลกระทบเชิงทราณซ์เวอร์สไอโซทรอปิกต่อสมบัติเชิงกลของหินยิปซัม



นางสาวลักษิกา สิริธิมงคล


วิทยานิพนธ์นี้เป็นส่วนหนึ่งของการศึกษาตามหลักสูตรปริญญาวิศวกรรมศาสตรดุษฎีบัณฑิต
สาขาวิชาวิศวกรรมโยธา ขนส่ง และทรัพยากรธรณี
มหาวิทยาลัยเทคโนโลยีสุรนารี
ปีการศึกษา 2564


TRANSVERSE ISOTROPIC EFFECT ON MECHANICAL PROPERTIES OF GYPSUM

Suranaree University of Technology has approved this thesis submitted in partial fulfillment of the requirements for the Degree of Doctor of Philosophy.

Thesis Examining Committee



.....
(Assoc. Prof. Dr. Pornkasem Jongpradist)
Chairperson



.....
(Prof. Dr. Kittitep Fuenkajom)
Member (Thesis Advisor)


.....
(Asst. Prof. Dr. Prachya Tepnarong)
Member


.....
(Asst. Prof. Dr. Decho Phueakphum)
Member


.....
(Dr. Thanittha Thongrapha)
Member


.....
(Assoc. Prof. Dr. Chatchai Jothityangkoon)
Vice Rector for Academic
Affairs and Quality Assurance


.....
(Assoc. Prof. Dr. Pornsiri Jongkol)
Dean of Institute of Engineering

ลักษิกา สิทธิมงคล : ผลกระทบเชิงทรานส์เวอร์สไอโซทรอปิกต่อสมบัติเชิงกลของหินยิปซัม
(TRANSVERSE ISOTROPIC EFFECT ON MECHANICAL PROPERTIES OF GYPSUM)
อาจารย์ที่ปรึกษา : ศาสตราจารย์ ดร.กิตติเทพ เฟื่องขจร, 77 หน้า.

คำสำคัญ: ความดันล้อมรอบ/ระนาบชั้นหิน/เกณฑ์การวิบัติของโคลอมบ์/พลังงานความเครียด

วัตถุประสงค์ของการศึกษานี้เพื่อหาผลกระทบของระนาบชั้นหินต่อกำลังรับแรงและสัมประสิทธิ์ความยืดหยุ่นของหินยิปซัม ตัวอย่างหินยิปซัมถูกดำเนินการภายใต้การตรวจวัดความเร็วคลื่นอัลตราโซนิก การทดสอบแรงกดแบบสามแกนและกำลังดึงแบบบลาซิลโดยมีความดันล้อมรอบคงที่ตั้งแต่ 0 ถึง 15 เมกะปาสคาล ผลการทดสอบระบุว่าความเร็วคลื่นมีค่าต่ำสุดเมื่อระนาบชั้นหินตั้งฉากกับแนวความเค้นหลักและมีค่าเพิ่มขึ้นจนกระทั่งมีค่าสูงสุดเมื่อระนาบชั้นหินขนานกับแนวความเค้นหลัก กำลังรับแรงกดมีค่าสูงสุดเมื่อระนาบชั้นหินตั้งฉากและมีค่าต่ำสุดเมื่อแนวตั้งฉากของระนาบชั้นหินทำมุม 60 องศากับแนวความเค้นหลัก ค่าสัมประสิทธิ์ความยืดหยุ่นที่ขนานกับระนาบชั้นหินจะมีค่าสูงกว่าค่าสัมประสิทธิ์ความยืดหยุ่นที่ตั้งฉากกับระนาบชั้นหินเสมอ อัตราส่วนระหว่างความยืดหยุ่นที่ขนานต่อความยืดหยุ่นที่ตั้งฉากกับระนาบชั้นหินมีแนวโน้มลดลงเมื่อความดันล้อมรอบเพิ่มขึ้น เกณฑ์การวิบัติของโคลอมบ์สามารถอธิบายค่ากำลังรับแรงกดของหินในรูปแบบความสัมพันธ์ระหว่างความเค้นยึดติดและการวางตัวของระนาบชั้นหินโดยใช้สมการพหุนาม พลังงานความเครียดที่จุดวิบัติสอดคล้องกับผลลัพธ์ที่ได้จากเกณฑ์การวิบัติของโคลอมบ์ ผลกระทบของทรานส์เวอร์สไอโซทรอปิกต่อเสถียรภาพของความลาดชันที่มีการวางตัวของระนาบชั้นหินถูกแสดงด้วยแบบจำลองของ Phase^{2D}

สาขาวิชา เทคโนโลยีธรณี

ปีการศึกษา 2564

ลายมือชื่อนักศึกษา ลักษิกา สิทธิมงคล

ลายมือชื่ออาจารย์ที่ปรึกษา ดร. กิตติเทพ

LAKSIKAR SITTHIMONGKOL: TRANSVERSELY ISOTROPIC EFFECT ON MECHANICAL PROPERTIES OF GYPSUM. THESIS ADVISOR : PROF. KITTITEP FUENKAJORN, Ph.D., P.E., 77 PP.

Keywords: Confining Pressure/ Bedding Plane/ Coulomb Criterion/ Strain Energy

The objective of this study is to determine the effects of bedding planes on the strengths and elasticity of gypsum. The gypsum specimens are subjected to ultrasonic pulse velocity measurements, triaxial compression, and Brazilian tension tests. The constant confining pressures are maintained between 0 and 15 MPa. The results indicate that wave velocity is smallest when bedding planes are normal to the major principal axis. They gradually increase to the largest when the beds are parallel to the major principal axis. The compressive strengths are maximum when the bedding planes are normal to loading direction and the minimum strengths occur when bedding planes makes an angle of 60 degrees with the loading direction. The elastic modulus parallel to the bedding plane is always higher than those normal to the bedding plane. The ratio of elastic moduli parallel-to-normal to the bedding planes tends to decrease with increasing confining pressures. Coulomb criterion is capable of describing the rock compressive strengths where the cohesion is defined as a polynomial function of bedding plane orientation. Distortional strain energy induced at failure coincides with the results obtained from the Coulomb criterion. The effect of transverse isotropy on stability of slope containing bedding planes is demonstrated by Phase^{2D} simulation.

School of Geotechnology

Academic Year 2021

Student's Signature ลักขิมา สิทธีมงคล

Advisor's Signature ค. ฟูเณจอร์น

ACKNOWLEDGMENTS

I wish to acknowledge the funding support from Suranaree University of Technology (SUT).

I would like to express thanks to Prof. Dr. Kittitep Fuenkajorn, thesis advisor, who gave a critical review. I appreciate his encouragement, suggestions, and comments during the research period. I would like to express thanks to Assoc. Prof. Dr. Pornkasem Jongpradist, Asst. Prof. Dr. Prachya Tepnarong, Asst. Prof. Dr. Decho Phueakphum and Dr. Thanittha Thongrapha for their valuable suggestions and comments on my research works as thesis committee members. Grateful thanks are given to all staffs of Geomechanics Research Unit, Institute of Engineering who supported my work.

Finally, I most gratefully acknowledge my parents and friends for all their support throughout the period of this study.

Laksikar Sitthimongkol

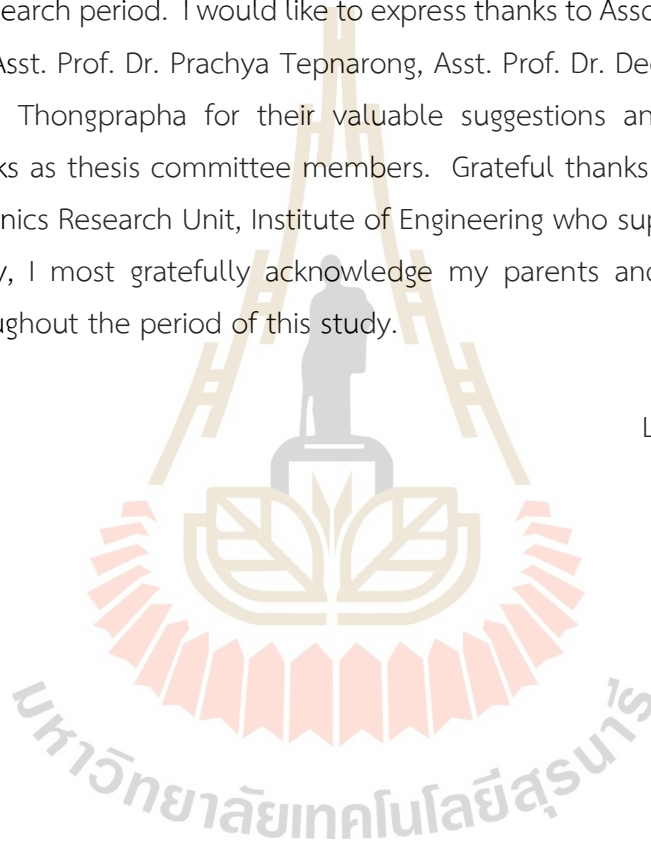


TABLE OF CONTENTS

	Page
ABSTRACT (THAI).....	I
ABSTRACT (ENGLISH).....	II
ACKNOWLEDGEMENTS.....	III
TABLE OF CONTENTS.....	IV
LIST OF TABLES.....	VII
LIST OF FIGURES.....	VIII
SYMBOLS AND ABBREVIATIONS.....	XI
CHAPTER	
1. INTRODUCTION.....	1
1.1 Background and rationale.....	1
1.2 Research objective.....	2
1.3 Scope and limitations.....	2
1.4 Research methodology.....	3
1.4.1 Literature review.....	4
1.4.2 Specimen preparation.....	4
1.4.3 Ultrasonic pulse velocity measurements.....	4
1.4.4 Triaxial compression test.....	4
1.4.5 Brazilian tension test.....	4
1.4.6 Determination of transversely isotropic elastic parameters.....	5
1.4.7 Modelling of slope stability with various bedding plane orientations.....	5
1.4.8 Discussions, conclusion and thesis writing.....	5
1.5 Thesis contents.....	5
2. LITERATURE REVIEW.....	6
2.1 Introduction.....	6
2.2 Definition of rock characteristics.....	6

TABLE OF CONTENTS (Continued)

	Page
2.2.1 Isotropic rock.....	6
2.2.2 Anisotropic rock.....	6
2.3 Effect of transversely isotropic on mechanical properties.....	8
2.4 Effect of transverse isotropy on elastic properties of rocks.....	11
2.5 Numerical modelling.....	12
3. SAMPLE PREPARATION.....	16
3.1 Introduction.....	16
3.2 Gypsum deposit.....	16
3.3 Sample preparation.....	16
4. LABORATORY TEST METHOD AND APPARATUS.....	23
4.1 Introduction.....	23
4.2 Ultrasonic pulse velocity measurements.....	23
4.3 Compression test.....	27
4.4 Brazilian tension test.....	29
5. TEST RESULTS.....	32
5.1 Introduction.....	32
5.2 Ultrasonic pulse velocity results.....	32
5.2.1 Wave velocities.....	32
5.2.2 Dynamic elastic parameters of transversely isotropic rock.....	32
5.3 Compression test results.....	34
5.3.1 Compressive strengths.....	34
5.3.2 Elastic parameters.....	37
5.4 Brazilian tension test results.....	37
5.4.1 Tensile strengths.....	37
5.4.2 Tensile elastic modulus.....	40
6. ANALYSIS OF TEST RESULTS.....	42
6.1 Introduction.....	42

TABLE OF CONTENTS (Continued)

	Page
6.2 Transverse isotropic effect on wave velocities.....	42
6.3 Transverse isotropic effect on elasticity.....	42
6.4 Apparent elastic parameters for transverse isotropy.....	45
6.5 Strength criterion.....	46
6.6 Strength criterion based on strain energy density.....	51
7. NUMERICAL MODELLING.....	54
7.1 Introduction.....	54
7.2 Numerical modelling.....	54
7.3 Material properties.....	54
7.4 Numerical results.....	56
8. DISCUSSIONS AND CONCLUSIONS.....	66
8.1 Discussions.....	66
8.2 Conclusions.....	68
8.3 Recommendations for future studies.....	69
REFERENCES.....	70
BIOGRAPHY.....	77

LIST OF TABLES

Table	Page
3.1 Mineral compositions and calculated porosity of gypsum obtained by XRD Analysis.....	19
3.2 Gypsum specimens prepared for compression test.....	21
3.3 Gypsum specimens prepared for Brazilian tension test.....	22
5.1 Averaged values of P- and S-waves for each orientations.....	33
5.2 Dynamic elastic parameters of transverse isotropic gypsum specimens.....	34
5.3 Compression test results.....	38
6.1 Five intrinsic elastic parameters under test conditions.....	43
6.2 Cohesions and friction angles for different bedding plane orientations.....	50
7.1 Material parameters used for numerical modelling.....	56

LIST OF FIGURES

Figure		Page
1.1	Research methodology.....	3
2.1	Isotropic (a), anisotropic (b), orthotropic (c), and transversely isotropic (d) rocks (Harrison and Hudson, 2002).....	7
2.2	Classification of anisotropy for transversely isotropic rocks (Ramamurthy et al, 1993).....	8
2.3	Four kinds of macro-fracture patterns occurred (Xu et al., 2013).....	9
2.4	Relationship between cohesion and internal friction angle and bedding plane angle (Hao et al., 2020).....	10
2.5	Tensile strengths as a function of bedding plane angles (Ma et al., 2018).....	11
2.6	Elastic modulus as a function of confining pressure (Hu et al., 2017).....	12
2.7	Anisotropic strengths (a) and elastic modulus (b) of cross joint and ubiquitous joints.....	14
2.8	Factors of safety as a function of bedding plane orientations (Wu et al., 2012).....	15
3.1	Depth level of gypsum at SCG Co., Ltd. (a). Stratigraphy and location of Tak Fa formation of the Saraburi group (Kuroda et al., 2017) (b).....	17
3.2	Open pit mine at SCG mine, the height of the bench is 5 m.....	17
3.3	The XRD pattern of gypsum powder.....	19
3.4	Gypsum specimens prepared for compression test (a) and Brazilian tension test (b).....	20
4.1	Wave velocity measurement device: sonic viewer and transmitter and receiver transducers.....	24
4.2	Four independent parameters used in the ultrasonic wave velocity measurements (Grgic et al., 2019), for $\beta = 0^\circ$ and 90°	24
4.3	Diagram showing the relationship between the phase velocity V_{p45° and the group velocity $V(\phi)$ (Song et al., 2004).....	25
4.4	Laboratory arrangement for compression testing.....	28
4.5	Definition of elastic parameters under compression test.....	29

LIST OF FIGURES (Continued)

Figure	Page
4.6	Laboratory arrangement for Brazilian tension testing (a) and locations of two strain gages on specimen with $\beta=90^\circ$ (b).....30
4.7	Notations of elastic parameters for some Brazilian tension test specimens with $\beta = 0^\circ$ (a), 30° (b), and 90° (c).....31
5.1	Wave velocities as a function of bedding plane orientations.....33
5.2	Stress-strain curves of gypsum specimens with $\beta = 0^\circ$ (a), 30° (b), 45° (c), 60° (d), and 90° (f). Notations used in Table 5.3 (d).....35
5.3	Compressive strengths as a function of bedding plane orientations β36
5.4	Some post-test specimens with different bedding plane angles.....36
5.5	Stress-strain curves from Brazilian tension test.....39
5.6	Brazilian tensile strengths (σ_B) as a function of bedding plane orientations.....39
5.7	Post-tests Brazilian tension test specimens for various bedding plane angles β40
5.8	Tensile elastic modulus (a) and Poisson's ratio (b) as a function of bedding plane orientations.....41
6.1	Wave velocities as a function of bedding plane orientations.....43
6.2	Ratio of elastic moduli parallel and normal to bedding plane (E/E') as a function of confining pressures.....44
6.3	Elastic moduli obtained along the major principle (E_1) as a function of confining pressure (σ_3).....45
6.4	Polar plots of apparent elastic moduli (E_y) under different bedding plane angles (β) of three test conditions: (a) wave velocity measurements, (b) compression test, and (c) Brazilian tension test.....47
6.5	Polar plots of apparent Poisson's ratios ν_{yx} and ν_{yz} under different bedding plane angles (β) on three test conditions: (a,b) wave velocity measurements, (c,d) compression test, and (e,f) Brazilian tension test.....48
6.6	Major principal stresses at failure ($\sigma_{1,f}$) as a function of confining pressure (σ_3). Lines are Coulomb criterion.....49
6.7	Cohesions and friction angles as a function of bedding plane orientation.....50

LIST OF FIGURES (Continued)

Figure	Page
6.8 Effect of anisotropy on critical stress state values (Hudson and Harrison, 1997).....	51
6.9 Distortional strain energy (W_d) at failure as a function of mean strain energy (W_m).....	53
7.1 Geometry of the rock slope (a) and finite element mesh and boundary condition (b).....	55
7.2 Contours of maximum shear strain with $\beta = 0^\circ$ (a), 60° (b), and 90° (c) at the slope face of 60°	57
7.3 Contours of maximum shear strain with $\beta = 0^\circ$ (a), 60° (b), and 90° (c) at the slope face of 70°	58
7.4 Contours of maximum shear strain with $\beta = 0^\circ$ (a), 60° (b), and 90° (c) at the slope face of 80°	59
7.5 Contours of maximum shear strain with $\beta = 0^\circ$ (a), 60° (b), and 90° (c) at the slope face of 90°	60
7.6 Factors of safety as a function of bedding plane orientations.....	61
7.7 Contours of slope displacements (centimeter) with $\beta = 0^\circ$ (a), 60° (b), and 90° (c) at the slope face of 60°	62
7.8 Contours of slope displacements (centimeter) with $\beta = 0^\circ$ (a), 60° (b), and 90° (c) at the slope face of 70°	63
7.9 Contours of slope displacements (centimeter) with $\beta = 0^\circ$ (a), 60° (b), and 90° (c) at the slope face of 80°	64
7.10 Contours of slope displacements (centimeter) with $\beta = 0^\circ$ (a), 60° (b), and 90° (c) at the slope face of 90°	65
8.1 Degrees of rock anisotropy (E/E') as a function of confining pressure. ① Hornfel, ② Schist, ③ Garnet hornfel (Fereidooni et al., 2016); ④ Mudstone (Miller et al., 2013); ⑤ Quartzitic schist, ⑥ Biotite schists (Nasseri et al., 2003); ⑦ Phyllite (Xu et al., 2018); ⑧ Meta-siltstone, ⑨ Schist (Usoltseva et al., 2017); ⑩ Sandstone (Hu et al., 2017).....	67

SYMBOLS AND ABBREVIATIONS

ϕ	=	friction angle
β	=	the angle between the normal of bedding planes and the major principal stress
W_m	=	Mean strain energy
W_i	=	Weight of each mineral in specimen obtained from XRD
W_d	=	Distortional strain energy
VSh_{90°	=	S-wave velocities for the bedding-parallel
VSh_{0°	=	S-wave velocities for the bedding-perpendicular
V_s	=	Shear (S-wave) wave velocity
VP_{90°	=	P-wave velocities for the bedding-parallel
VP_{45°	=	P-wave along the direction $\theta=45^\circ$
VP_{0°	=	P-wave velocities for the bedding-perpendicular
V_p	=	Compressional (P-wave) wave velocity
S.G. _i	=	Specific gravity of each mineral
n	=	Porosity
G'	=	Shear modulus on the plane normal to transverse isotropic plane
G	=	Shear modulus on transverse isotropic plane
E_y	=	Apparent Young's modulus
$E_{T(90-\beta)}$	=	Tensile elastic modulus with strain gage (lateral) normal to loading axis
$E_{C(b)}$	=	Compressive elastic modulus, obtained from the uniaxial test condition
E_{3P}	=	Elastic moduli along the two minor principal (lateral) axes parallel to bedding plane strike
E_{30}	=	Elastic moduli along the two minor principal (lateral) axes normal to bedding plane strike
E_1	=	Elastic moduli along the major principal (axial) direction

SYMBOLS AND ABBREVIATIONS (Continued)

E'	=	Elastic moduli normal to strike of transverse isotropic plane
E	=	Elastic moduli parallel to strike of transverse isotropic plane
c_{0°	=	Cohesion obtained from specimens with $\beta = 0^\circ$
c	=	Cohesion
ν_{yz}	=	Apparent Poisson's ratios in y-z coordinate system
ν_{yx}	=	Apparent Poisson's ratios in y-x coordinate system
ϵ_y	=	Strain in y-direction (axial)
σ_y	=	Compression with the magnitudes of three times the Brazilian tensile stress
ϵ_x	=	Strain in x-direction (lateral)
σ_x	=	Brazilian tensile stress
ν_T	=	Poisson's ratios on the plane between the loading axis and the directions that are normal to loading axis
ρ_{rock}	=	Density of specimen
$\gamma_{\text{oct, f}}$	=	Octahedral shear strain at failure
$\tau_{\text{oct, f}}$	=	Octahedral shear stress at failure
$\epsilon_{m, f}$	=	Mean strain
$\sigma_{m, f}$	=	Mean stress
$\nu_{3P,3O}$	=	Poisson's ratio between the directions that are parallel and normal to the bedding plane strike
ϵ_{3P}	=	Strains measured parallel to the strike of bedding planes.
ϵ_{3O}	=	Strains measured normal to the strike of bedding planes.
σ_3	=	Minor principal stresses
$\sigma_{1, f}$	=	Major principal stress at failure
$\nu_{1,3P}$	=	Poisson's ratios on the planes between the major principal axis and the directions parallel to the strike of bedding planes

SYMBOLS AND ABBREVIATIONS (Continued)

$\nu_{1,3P}$	=	Poisson's ratios on the planes between the major principal axis and the directions normal to the strike of bedding planes
ϵ_1	=	Major principal strain
σ_1	=	Major principal stresses
ψ	=	Slope angle
ν	=	Poisson's ratio on transverse isotropic plane
ν'	=	Poisson's ratio on the plane normal to transverse isotropic plane
δ	=	Constant parameter
θ	=	Angle between the wave vector normal to the wavefront and the symmetry axis along x-direction

CHAPTER I

INTRODUCTION

1.1 Background and rational

Anisotropy is one of features that has effect on geological civil, mining, and petroleum engineering. Thus, knowledge of the mechanical behavior of anisotropic rocks plays significant role in geological engineering. Rock is mostly intersected by various layers and joints (discontinuities) due to the geological features and tectonic movements. The main of geological features divided into 3 features: (1) Primary structure (rock fabric anisotropy, texture, schistosity and fissility), (2) Second structure (cracks, bedding planes, shear planes and faults) and (3) Discontinuity frequency (discontinuity spacing) (Khanlari et al., 2014). Igneous rocks have few possibilities of anisotropy feature. But in some cases (such as granite), the anisotropy may be found due to layering when the lava flows and moves as highly viscous masses (Walhlstrom, 1973). Sedimentary rocks often show bedding planes occur sedimentation processes of different layers or different minerals with various grain sizes. And metamorphic rocks are mostly anisotropy. Both of schistosity and cleavage are form in the influence of directed stress field and temperatures (Singh et al., 1989; Ramamurthy et al., 1993). Most of researchers report that anisotropy feature may also affect physical and mechanical properties. The P-wave velocity measured perpendicular to bedding are slightly lower than parallel to bedding (Crampin, 1981; Singhal and Gupta, 2010; Khanlari et al., 2014 and Abbass et al., 2018). Strength and deformation of rocks are depending on angle between bedding planes and the major principal stress (β). When the load is parallel to bedds, the opening of the bedding planes is the controlling damage mechanism, when the load is normal to the bedd, the bedding planes close up, and hence sliding along bedding planes is an important factor (Zhang et al., 2015).

Gypsum deposits in Thailand has been found in Phichit, Nakhon Sawan, Surat Thani and Nakhon Si Thammarat provinces. They are used in a variety of applications such as plaster, plasterboard, gypsum fiberboard, and gypsum block. The nature of gypsum is deposited from hypersaline lagoons. Most of the gypsum beds have been affected by tectonic movements and forming domes or irregular anticlines (Utha-aroon

and Ratanajaruraks, 1996). This feature shows the effect of bedding plane orientation on gypsum properties. It also affects stability of pit walls for quarry mining.

1.2 Research objective

This study is aimed at determining transversely isotropic effect on the strength and static and dynamic elasticity of gypsum. Ultrasonic pulse velocity measurement, triaxial compression test, and Brazilian tension test are performed to determine the mechanical properties of gypsum specimens with various bedding plane orientations. The elastic moduli and Poisson's ratios are based on Amadei's solutions. The Coulomb criterion and strain energy density are used to describe the transversely isotropic effect under confinements. The findings can be used as numerical parameters to simulate the slope stability with different bedding plane orientations.

1.3 Scope and limitations

1) Laboratory experiments are carried out on gypsum specimens obtained from SCG Cement Co., Ltd, Nakhon Sawan province, Thailand.

2) For compression test, cylindrical specimen is 54 mm in diameter and 108 mm in length. For Brazilian tension test, cylindrical specimen is 100 mm in diameter and 50 mm in length with different directions with respect to the bedding plane orientation to major principal stress (β) of 0, 30, 45, 60 and 90°.

3) Triaxial compression tests are performed with the confining pressures varying from 0, 3, 5, 7, 12 to 15 MPa.

4) Testing procedure follow the relevant ASTM standard practice, as much as, practical.

5) All tests are conducted under ambient temperature.

6) Phase^{2D} program is used in the simulations.

7) The research findings are published in conference paper or journal.

1.4 Research methodology

The research methodology shown in Figure 1.1 comprises 7 steps; including 1) literature review, 2) sample preparation, 3) laboratory testing (ultrasonic pulse velocity measurements, triaxial compression, and Brazilian tension tests), 4) determination of transversely isotropic elastic parameters, 5) modelling of slope stability with various bedding plane orientations, 6) discussions and conclusions, and 7) thesis writing and presentation.

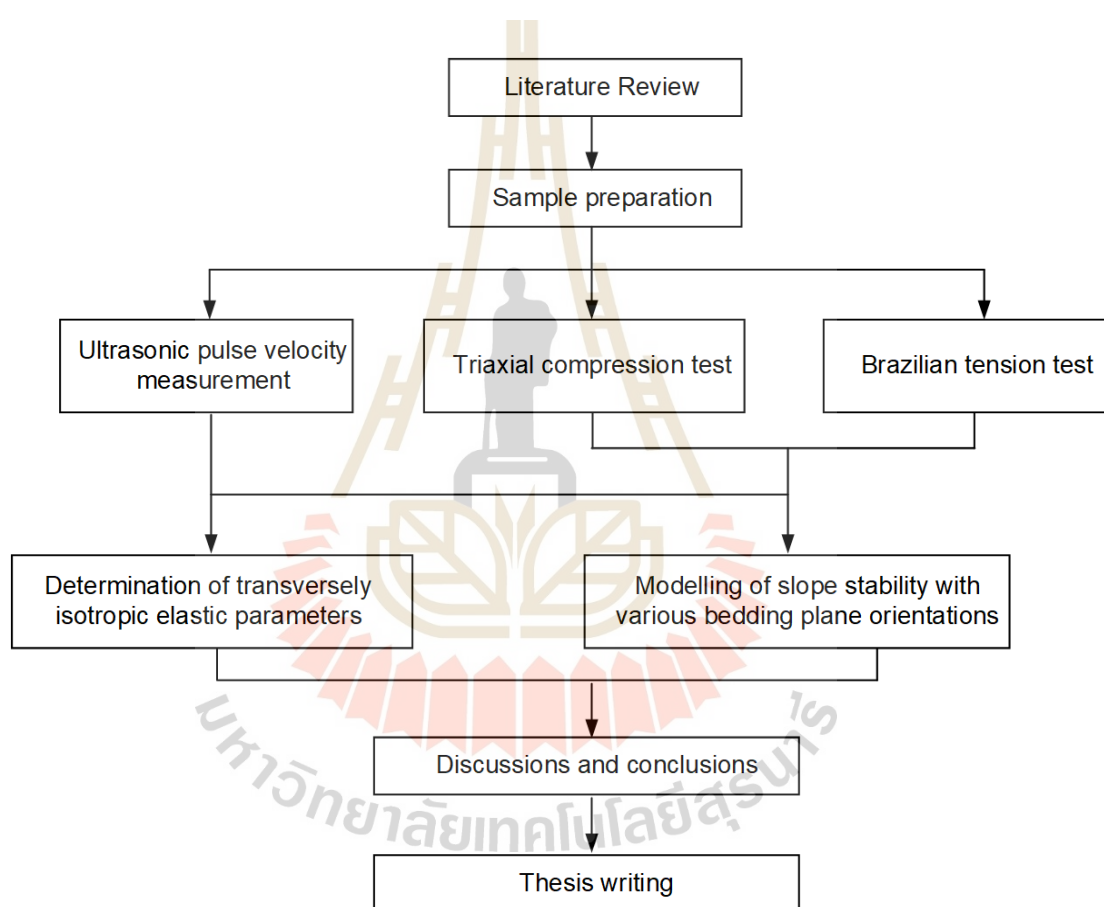


Figure 1.1 Research methodology.

1.4.1 Literature review

Literature review is carried out to study previous researches on effects of anisotropy on physical and mechanical properties of rocks and numerical simulation. The sources of information are from textbooks, journals, technical reports and conference papers. A summary of the literature review is given in chapter two.

1.4.2 Specimen preparation

Rock samples used here have been obtained from Siam Cement Public Company Limited, Thailand. Sample preparation is carried out in the laboratory at Suranaree University of Technology. The specimens are divided into 2 groups: (1) the cylindrical specimens with diameters of 54 mm and 108 mm in length and (2) disk specimens with 100 mm diameter and 50 mm in thickness with the bedding plane orientations (β) of 0, 30, 45, 60 and 90° respect to the major principal stress.

1.4.3 Ultrasonic pulse velocity measurements

Wave velocity measurement is performed on the compression specimens before loading. Sonic viewer 170 (Model 5338) is used to measure the P- and S-wave velocities. The end surfaces of the specimens are flattened and smoothen to provide tight contacts with transmitter and receiver transducers. The direct transmission method is conducted for measuring of compressional (P-wave) and shear (S-wave) wave velocities to calculate the dynamic elastic parameters of the specimen based on the standard practice (ASTM D2845-08).

1.4.4 Triaxial compression test

The compressive strengths are determined by axially loading the specimens under constant rate of 0.5-1 MPa/s. The samples are placed in a triaxial cell with confining pressures from 0, 3, 5, 7, 12 to 15 MPa. The tests are performed by increasing the axial stress until failure occurs. The axial and lateral displacements are monitored using dial gauges and strain gages, respectively. The results are used to determine the elastic modulus and Poisson's ratio.

1.4.5 Brazilian tension test

The Brazilian tension test is performed to determine tensile strengths and elastic parameters of the gypsum specimens under tension. The load configuration uses flat platens. The loading rate is controlled at approximately 0.1 MPa/s (ASTM D3967-16). Strain gages are installed to measure tensile and compressive strains at the center of the specimen.

1.4.6 Determination of transversely isotropic elastic parameters

The five elastic parameters based on generalized Hooke's law and the apparent elastic parameter based on Amadei (1996) solutions are applied to evaluate the elastic moduli and Poisson's ratios under various orientations of bedding planes.

1.4.7 Modelling of slope stability with various bedding plane orientations

The finite element model is formulated in Phase^{2D} program. Coulomb criterion is used to determine the stability of slope with different bedding angles by creating the ubiquitous joint model.

1.4.8 Discussions, conclusion and thesis writing

All study activities, methods, and results are documented and compiled in the thesis.

1.5 Thesis contents

This research thesis is divided into eight chapters. **Chapter II** includes background and rationale, research objectives, scope and limitations and research methodology. **Chapter III** presents the results of the literature review to improve an understanding of the physical and mechanical properties of transversely isotropic rock. **Chapter IV** describes the sample preparations. **Chapter V** describes the test methods, apparatus, and calculation of strengths and elastic parameters on transverse isotropic specimens. **Chapter VI** presents the results of laboratory experiments. **Chapter VII** describes the transverse isotropic effect on gypsum elasticity and strength criteria. **Chapter VIII** demonstrate the effect of transverse isotropy on stability conditions of slope forming by bedding planes. **Chapter IX** presents discussions, conclusions, and recommendations for future studies.

CHAPTER II

LITERATURE REVIEW

2.1 Introduction

In this chapter the relevant research and information about previous studies related to the effect of transversely isotropic on mechanical properties of rock are reviewed and summarized. These include strength, wave velocity, and elastic parameters. The effect of bedding plane orientations on rock slope and tunnel by using numerical simulations. The review results are summarized below.

2.2 Definition of rock characteristics

This section describes the rock characteristics in engineering works. The main properties emphasize here are the elastic properties in x-y-z directions based on Hooke's law.

2.2.1 Isotropic rock

Isotropic is materials which have identical properties in all directions (Figure 2.1a). Analysis of rock deformation under loading usually involves elastic theory that assumes rock as a linear elastic and continuum medium. It is important to consider rock anisotropy (Liao et al., 1997). The isotropy of the rock shows that $E_x = E_y = E_z = E$, $\nu_{xy} = \nu_{xz} = \nu_{yz} = \nu$, and $G_{xy} = G_{xz} = G_{yz}$, where E_x , E_y , and E_z are elastic moduli, ν_{xy} , ν_{xz} , and ν_{yz} are Poisson's ratios and G_{xy} , G_{xz} , and G_{yz} are shear moduli in referenced to x-y-z axes. For these rocks, the Young's modulus: E and Poisson's ratios: ν are needed.

2.2.2 Anisotropic rock

Many rocks are anisotropic. Their properties vary with direction. This variation is often related to the existence of well-defined rock fabric in forms of bedding, layering, schistosity planes, foliation, fissuring and jointing. These features show clear evidence of anisotropy with one or several apparent directions of symmetry (Turner and Weiss, 1963), as shown in Figure 2.1b. Deformability, a fourth order tensor C_{ijkl} that relates stress tensor s_{ij} to strain tensor e_{kl} , is an important parameter in the analysis of stress. C_{ijkl} is defined in a Cartesian coordinates system (x,y,z). These tensors can be written in a matrix form. Rock with 21 constants in C_{ijkl} is called anisotropic. The number of elastic constants can be reduced if the elastic material has some form of symmetry.

Anisotropic rock can be mostly modeled as orthotropic or transversely isotropic materials (Liao et al., 1997), as follows:

1. Orthotropic material has three mutually perpendicular planes of symmetry, but different properties along each of three principal directions, such as rock mass with three sets of orthogonal fracture having different properties (Figure 2.1c). For the orthotropic materials, nine properties are required (Young's moduli: E_x , E_y and E_z , shear moduli: G_{yx} , G_{yz} and G_{xz} , Poisson's ratios: ν_{yx} , ν_{yz} and ν_{xz}).

2. Transversely isotropic material used to describe the symmetry of rocks with one dominate system layers, such as foliated and sedimentary rocks or rock masses with one joint set (Figure 2.1d). The layer (e_2 , e_3) is assumed to coincide with the plane of transverse isotropy. Properties are identical in all directions in this plane (Amadei, 1996). For such materials, five properties are required (Young's moduli: E_x and E_y , shear moduli: G_{yx} , Poisson's ratios: ν_{yx} and ν_{xz}).

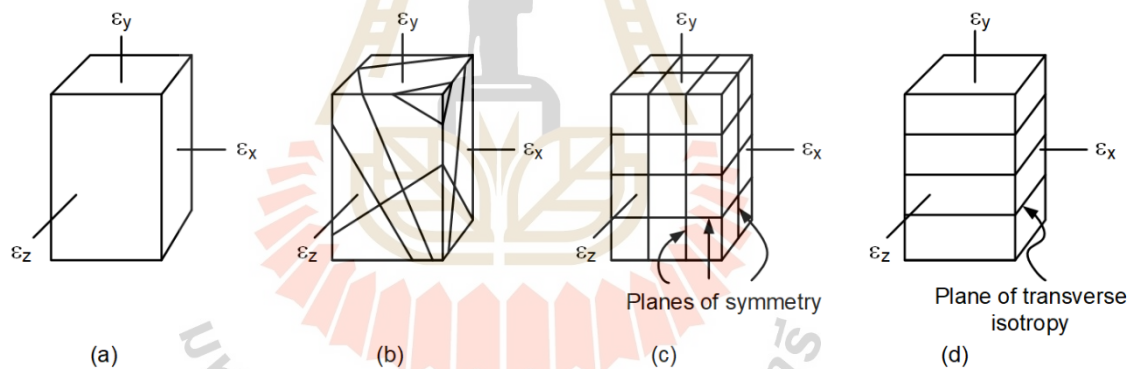


Figure 2.1 Isotropic (a), anisotropic (b), orthotropic (c), and transversely isotropic (d) rocks (Harrison and Hudson, 2002).

2.3 Effect of transversely isotropic on mechanical properties

The compressive strength on transversely isotropic rocks have been studied. e.g. Vales et al. (2004), Zhang et al. (2015), Ismael et al. (2017b), Xu et al. (2019) as well as Li et al. (2020a) on shale; Dehler and Labus (2007) and Kanlari et al. (2014) on sandstones; Berčáková et al. (2020) on gneiss. A review state that the maximum strengths are either bedding planes normal or parallel to the major principal stress ($\beta = 0^\circ$ or 90°) and minimum strength is β varies from 45° to 60° . The curve of anisotropy is classified by Ramamurthy et al. (1993). It divides into 3 types: shoulder type, U-type, and Wavy type (Figure 2.2). The U-type is observed in slate, phyllite and schist. The shoulder type is observed in shale and sandstone. And wavy type is observed in coal and diatomite (Ramamurthy, 2010). Xu et al. (2019) proposed that the changing trend of compressive strength is related to micro-crack mechanism of rocks. For $\beta=90^\circ$, the fractures occur tensile splitting along bedding plane, while for $\beta=0^\circ$ fracturing occur

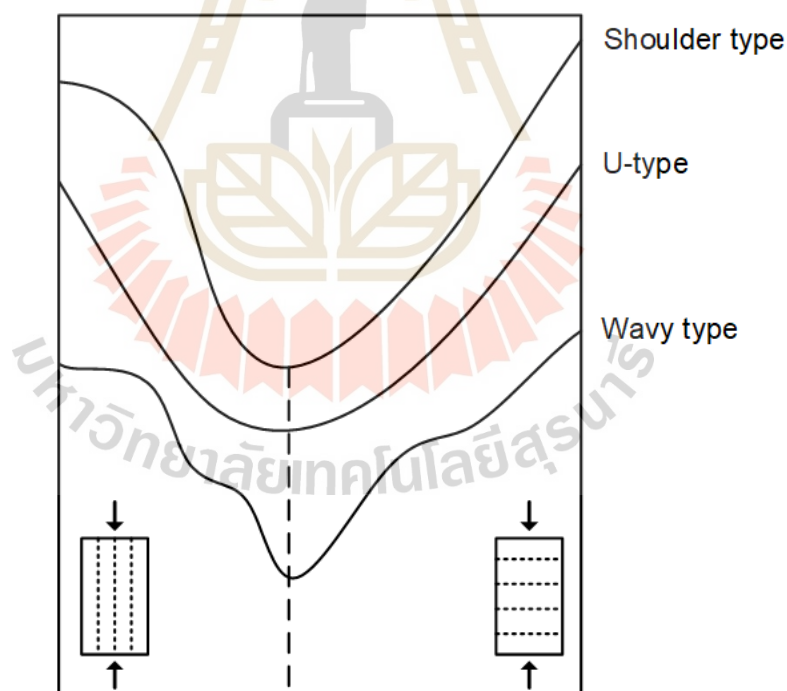


Figure 2.2 Classification of anisotropy for transversely isotropic rocks (Ramamurthy et al., 1993).

composite tensile splitting across and along bedding plane. For inclination angle ($0^\circ < \beta < 90^\circ$), the fractures occur composite sliding-shear and shear failure across bedding plane (Figure 2.3), which results reduce rock strength more than $\beta = 0^\circ$ or 90° . These reasons agree well with Xiao et al. (2014) and Khanlari et al. (2014). Yang et al. (2019) and Hao et al. (2020) study the influence of compressive strength on transversely isotropic rock under confining pressure. The anisotropic effect of the compressive strength will disappear at a sufficiently high confining pressure (Cheng et al., 2017 and Yaşar, 2001). Based on Mohr–Coulomb criterion, the cohesion and friction angle can be determined. The cohesion displays U-shaped curve and friction angle decrease while increasing bedding angle (Figure 2.4).

Many researchers have studied the effect of bedding plane orientation on tensile strength using the point load (Saroglou and Tsiambaos, 2008; Khanlari et al., 2014) and Brazilian test (Varvoort et al., 2014; Mahjoub et al., 2015; Tan et al., 2015; Kundu et al., 2018; Ma et al., 2017). They observed that the tensile strength is maximum when the loading direction is perpendicular to bedding plane and decreases rapidly with increases in the angle of bedding plane. This is because of fracture pattern on the rock specimens, as shown in Figure 2.5. Specimens with bedding plane angles parallel and perpendicular to the loading direction crack in tension, whereas other orientations crack in a mixed tension and shear. For bedding plane parallel to loading direction, the tension cracks along bedding plane, which is lower the tensile strength than those of perpendicular ones.

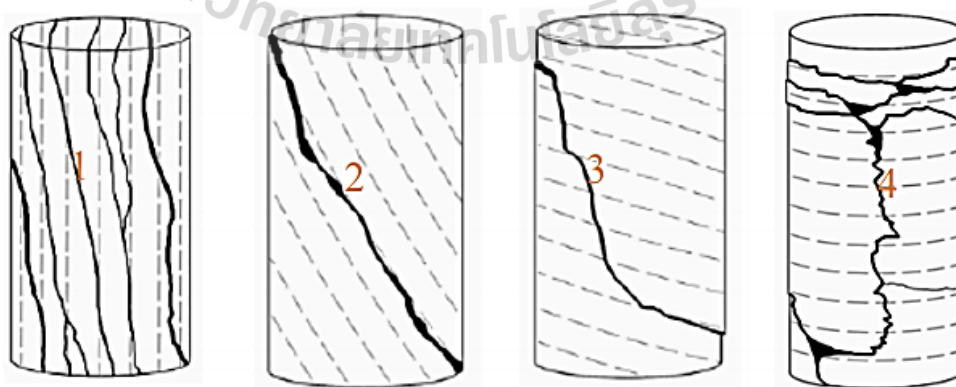


Figure 2.3 Four kinds of macro-fracture patterns occurred (Xu et al., 2019).

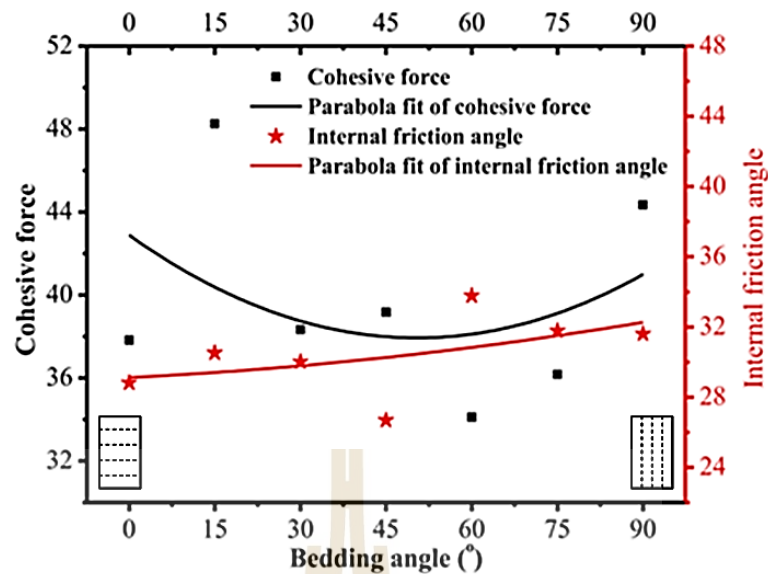


Figure 2.4 Relationship between cohesion and internal friction angle and bedding plane angle (Hao et al., 2020).

The effect of bedding planes orientations on the wave velocities have been investigated. Song et al. (2004), Song and Suh (2014), and Mokhtari et al. (2014) measured the ultrasonic pulse velocity of different rock types in two directions, parallel and perpendicular to bedding plane. They found that both P- and S- wave velocities are lowest when perpendicular to bedding whereas they are higher when parallel to bedding planes. Grgic et al. (2019), Abbass et al. (2020), Li et al. (2020b), and Wang and Han (2020) also study the ultrasonic pulse velocity with different bedding plane orientations and concluded that wave velocities increase with increasing bedding plane orientations. To understand the mechanism of the bedding angle affecting wave propagation characteristics, Li et al. (2020b) proposed the acoustic theory, in which the rock matrix and bedding plane are different acoustic characteristics. The rock matrix is usually considered to have higher wave velocity and lower attenuation than those in the bedding plane because the matrix has a higher elastic modulus. The reflection and refraction of the acoustic waves occur at the interface between the matrix and the bedding plane which results in wave energy loss. The larger bedding angle is associated with fewer interfaces when waves propagate through the specimen from top to bottom, which means weaker reflection and refraction of waves. Thus, waves with a higher bedding plane have lower attenuation and higher wave velocities.

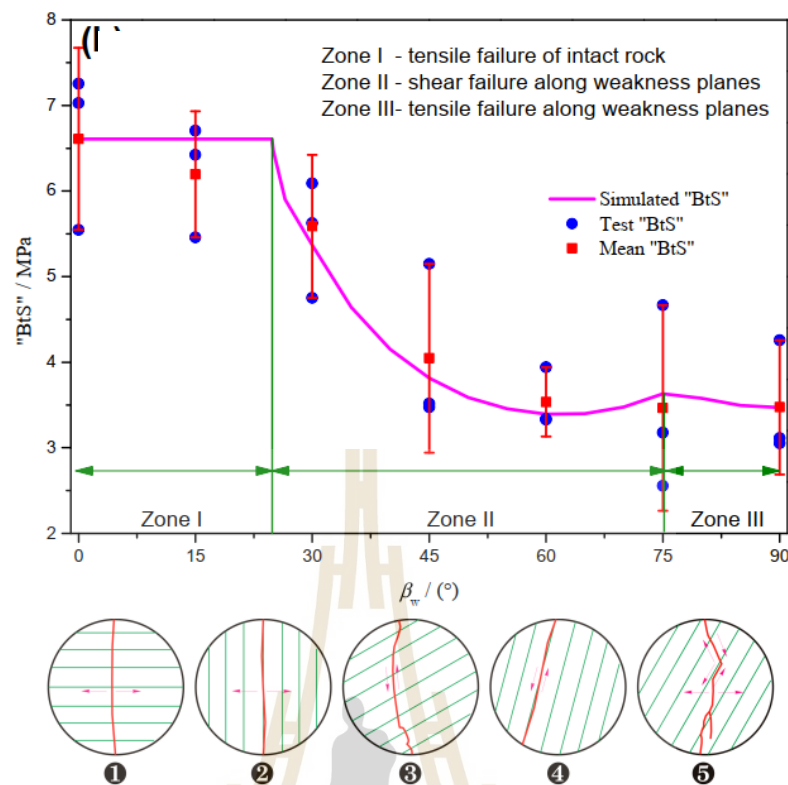


Figure 2.5 Tensile strengths as a function of bedding plane angles (Ma et al., 2018).

2.4 Effect of transverse isotropy on elastic properties of rocks

The deformability of rocks is related to the bedding plane orientation. Existing studies have focused on the elastic properties carried out compression tests with various bedding plane angles (Heng et al., 2015; Wang et al., 2016; Cheng et al., 2017; Hu et al., 2017; Meng et al., 2018). They conclude that elastic modulus increases and Poisson's ratio slightly decrease with increasing bedding plane angle and that the minimum elastic modulus is obtained when $b = 0^\circ$ (perpendicular to the bedding plane). This is because when bedding is perpendicular to the loading direction, bedding plane is easily compressed by normal stress. Therefore, the axial deformation turns to be large and leads to smaller elasticity modulus.

Amadei et al. (1987) proposes the degree of anisotropy of rock that can be determined by the ratio of maximum to minimum elastic modulus (E_{90°/E_0°). The results state that the degree of anisotropy decreases with increasing confining pressure. Due to the elastic modulus at angle $b = 0^\circ$ is more sensitive to confining pressure. The

elastic modulus increases significantly with increasing confining pressure (Figure 2.6). These agree well with Hu et al. (2017) and Yang et al. (2019).

2.5 Numerical modelling

Numerical models can be simulated the effect of bedding plane orientation on rock mass. Furthermore, many researchers proposed constitutive models for layered jointed rock masses. Ubiquitous joint model is commonly used to represent the bedding plane and assumes a direction of bedding plane with no associated joint spacing, length, and stiffness (Clark, 2006; Sainsbury, 2008; Wang et al., 2012; Wu et al., 2012; Ismael and Konietzky, 2017a; Leng et al., 2021; Zhou et al., 2021).

Sainsbury and Sainsbury (2017) simulate the numerical uniaxial compression under ubiquitous joints and cross joints with various joint spacing by UDEC software. The compressive strength and deformation of the samples are analyzed. The results indicated that the predicted compressive strengths under two joints have similar trends (Figure 2.7a), and the U-shaped curve is according to lab experiment. However, the elastic modulus obtained from ubiquitous joints depends on the bedding angle while cross joints tend to be independent of them (Figure 2.7b). They recommend that the ubiquitous joint as bedding plane is greater the those with cross joints and it is not observed in the rock mass specimen.

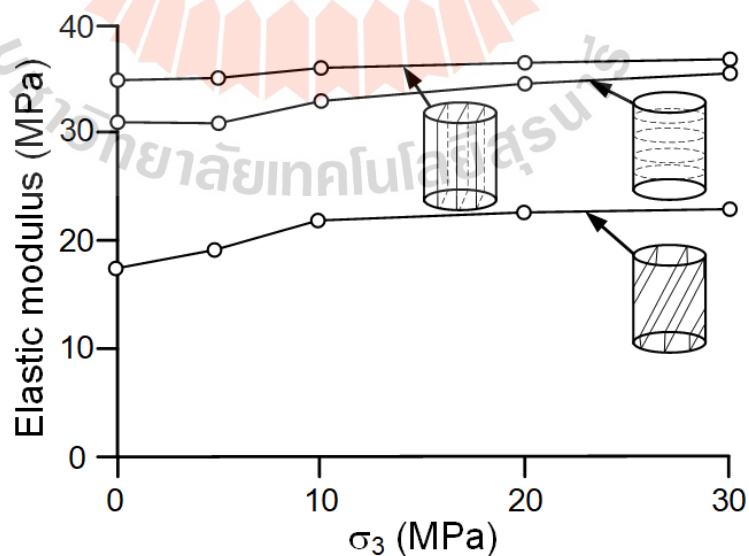
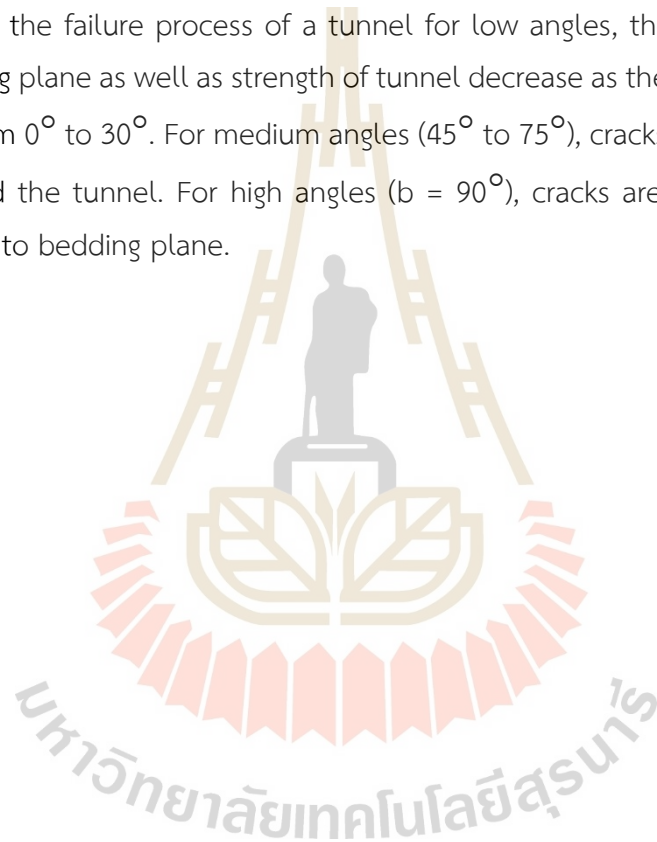


Figure 2.6 Elastic modulus as a function of confining pressure (Hu et al., 2017).

Wu et al. (2012) and Zhou et al. (2021) who study the numerical simulation for the effect of bedding plane orientation on slope stability state that the bedding plane has impact on the factor of safety of slope. When bedding angle is 50° , the factor of safety is the smallest, as shown in Figure 2.8. As the bedding angle increase, the shape of sliding surface changes from circular mode to a mixed-mode of circular and planner. Furthermore, Wang et al. (2012) simulate the failure of circular tunnels under different bedding plane angles. The results indicated that the strengths of tunnel decrease when bedding angle increase from 0° to 60° , and start to increase beyond this range. In the failure process of a tunnel for low angles, the cracks can develop along bedding plane as well as strength of tunnel decrease as the bedding plane angle increases from 0° to 30° . For medium angles (45° to 75°), cracks mainly caused shear stress around the tunnel. For high angles ($b = 90^\circ$), cracks are tensile cracking that occurs along to bedding plane.



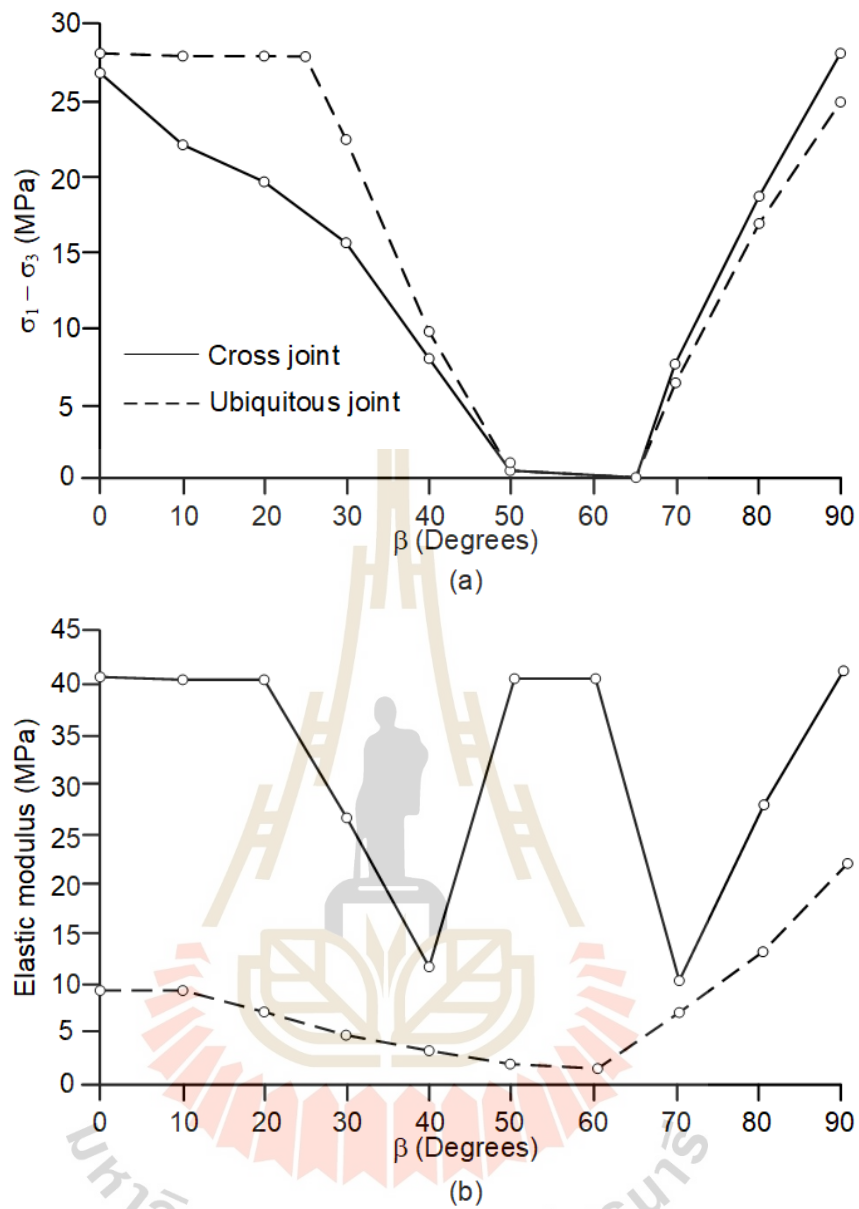


Figure 2.7 Anisotropic strengths (a) and elastic modulus (b) of cross joint and ubiquitous joints (Sainsbury and Sainsbury, 2017).

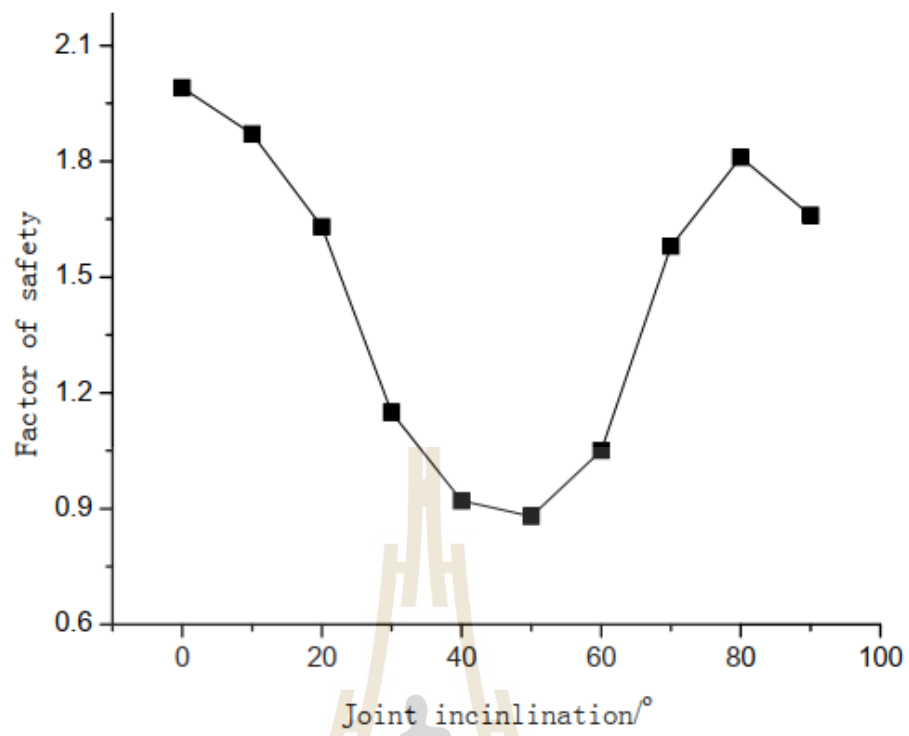


Figure 2.8 Factors of safety as a function of bedding plane orientations (Wu et al., 2012).

CHAPTER III

SAMPLE PREPARATION

3.1 Introduction

This chapter describes the gypsum preparation used in this study. Origin and description of gypsum deposit are described. Physical and chemical properties and dimensions of the rock specimens are determined.

3.2 Gypsum deposit

The sulfate deposits in Thailand are located in Pichit-Nakhon Sawan area, Nakhon Si Thamrat. Surat Thani area, and Loei-Wang Saphung area. According to the geological map by Kuroda et al. (2017), sulfate evaporites are precipitation of pristine gypsum from seawater during the Serpukhovian (Last Mississippian) at the margin of the Indochina block. Then, transformation of the gypsum to anhydrite through dehydration at an early stage of burial and rehydration of the top part of anhydrite to form secondary gypsum near surface. This occurs at Nakhon Sawan province.

Gypsum specimens used in this study are prepared from Tak Fa formation of the Saraburi group in northeastern Nakhon Sawan province. There is small sulfate deposit up to 60 m thick with gypsum-anhydrite beds and covered by unconsolidated soil (Figure 3.1). Figure 3.2 shows open pit wall at Siam Cement Group (SCG) mine. Gypsum-anhydrite facies as laminae of white gypsum and dark gray anhydrite are formed. This implies that the top part of the anhydrite body has been rehydrated to gypsum due to exhumation.

3.3 Sample preparation

The gypsum blocks have been collected from opening mine of SCG Co., Ltd. Gypsum is alabaster variety with fine-grained ranging from 0.1-0.5 mm. The specimens have a bulk density of 2.25 ± 0.03 g/cc, which is determined by the ratio of dry mass and volume. The effective porosity according ASTM standard method (ASTM C97) are not observed. Because gypsum are low permeability and porosity, the effect of water saturation is neglected. Chamwan (2020) proposes new technique to obtained the

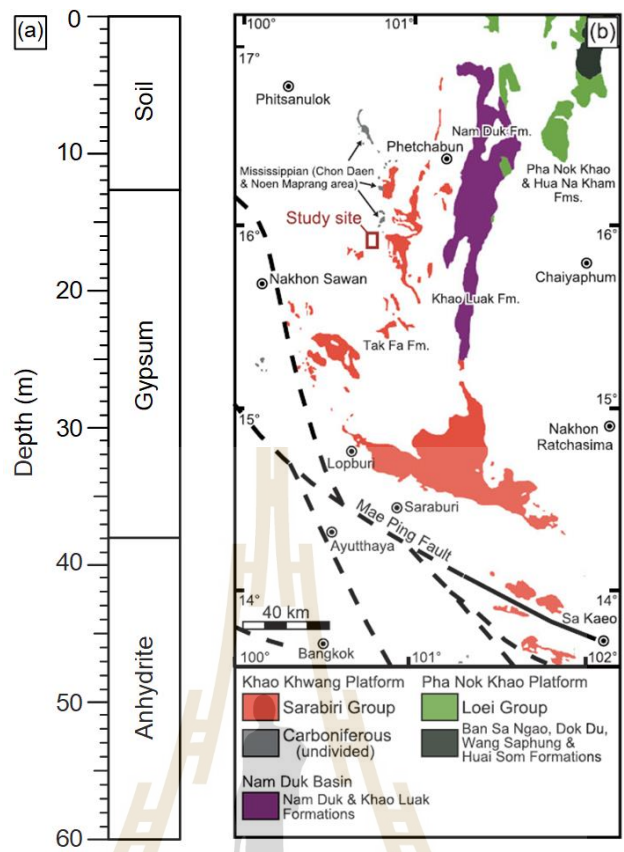


Figure 3.1 Depth level of gypsum at SCG Co., Ltd. (a). Stratigraphy and location of Tak Fa formation of the Saraburi group (Kuroda et al., 2017) (b).

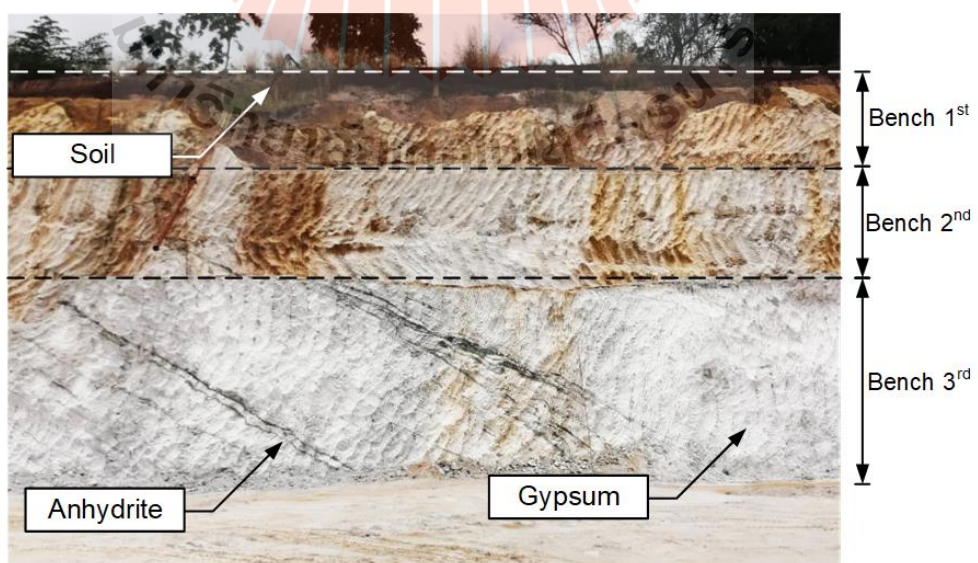


Figure 3.2 Open pit mine at SCG mine, the height of the bench is 5 m.

volume of pore space of the rock by data from X-ray diffraction (XRD). This is an indirect method. The calculated porosity (n) can be determined, as follows:

$$n = [1 - (\rho_{\text{rock}} \cdot \sum_{i=1}^n W_i / S.G._i)] \times 100 \quad (\%) \quad (3.1)$$

where i is number of minerals. W_i is weight of each mineral in specimen obtained from XRD (%), $S.G._i$ is specific gravity of each mineral, and ρ_{rock} is density of specimen (g/cc). Table 3.1 gives chemical compositions of the specimens as analyzed by X-ray diffraction (XRD). Data is collected in the $10\text{-}80^\circ 2\theta$ range (0.02° step size), as shown in Figure 3.3.

The gypsum samples are drilled from the collected blocks in 5 directions, with angle of 0° , 30° , 45° , 60° , and 90° with respect to the bedding planes, where β is the angle between the normal of bedding planes and the major principal stress (called here at to angle β). For compression test, cylindrical specimen is 54 mm in diameter and 108 mm in length (Figure 3.4a). Six specimens are prepared for each β , with a total of 30 specimens. For Brazilian tension test, cylindrical specimen is 100 mm in diameter and 50 mm in length (Figure 3.4b). Five samples are prepared for Brazilian tension test. Tables 3.2 and 3.3 show the dimensions and weigh of the specimen for compression and Brazilian tension test.

Table 3.1 Mineral compositions and calculated porosity of gypsum obtained by XRD analysis.

Mineral composition (%)		Specific gravity of mineral	Calculated porosity (%)
Gypsum	88.9	2.32	4.47
Chlorite	3.0	2.60	
Calcite	7.98	2.71	
Anhydrite	0.12	2.89	

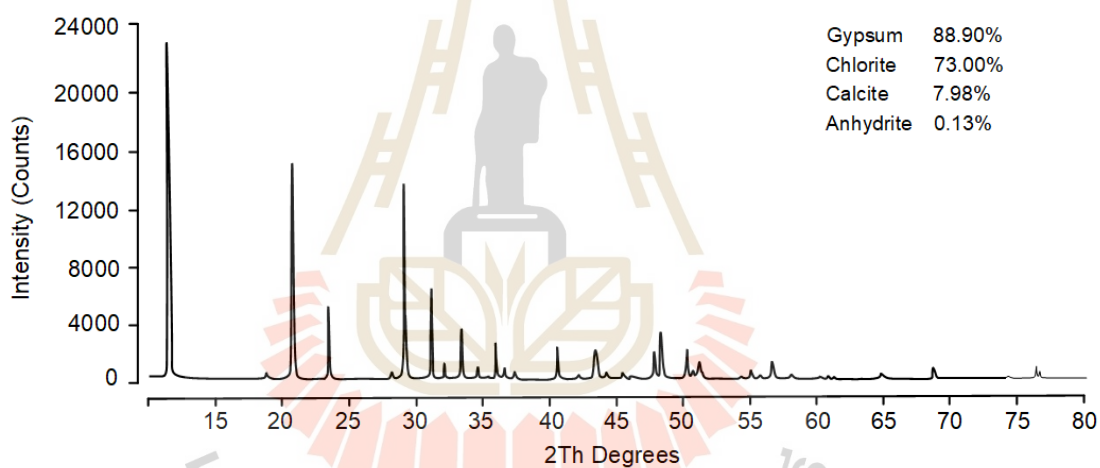


Figure 3.3 The XRD pattern of gypsum powder.

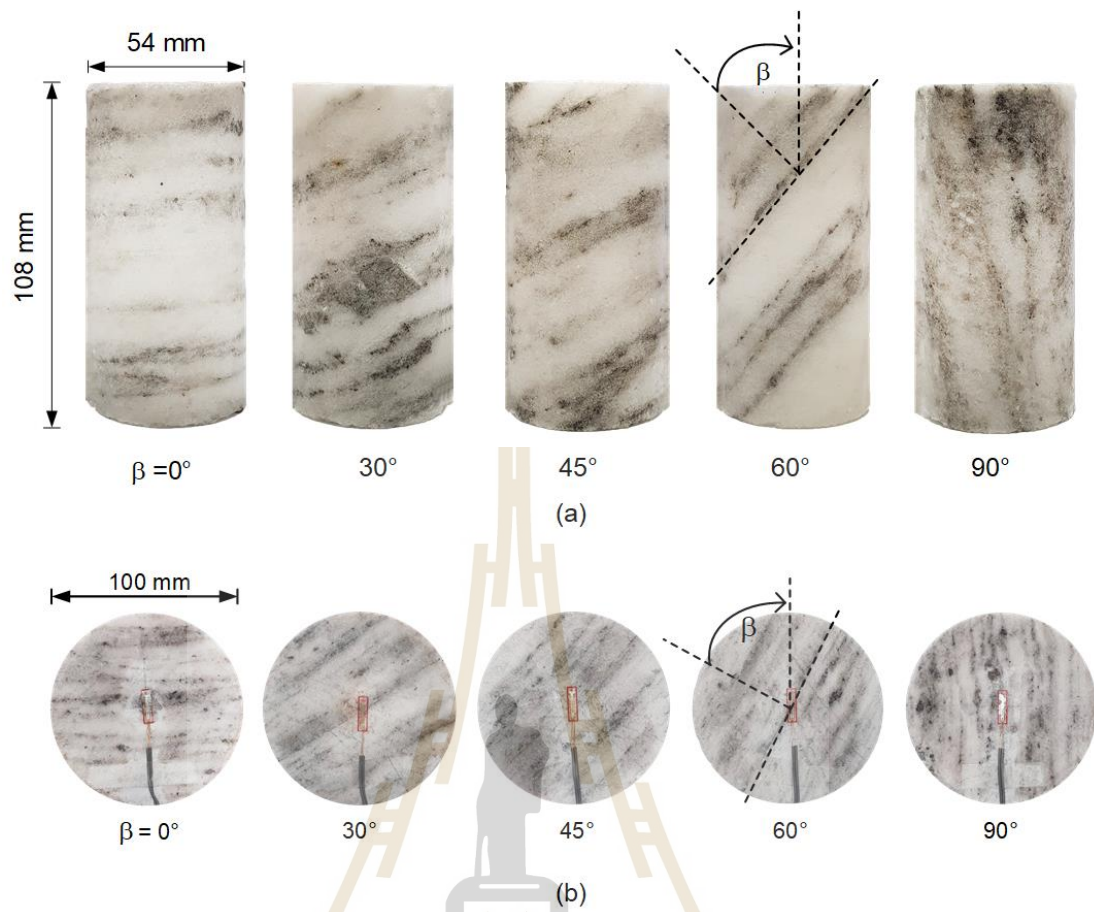


Figure 3.4 Gypsum specimens prepared for compression test (a) and Brazilian tension test (b).

Table 3.2 Gypsum specimens prepared for compression test.

Specimen No.	β (Degrees)	Diameter (mm)	Length (mm)	Weight (g)	Density (g/cc)
UCS-0-0	0	54.84	133.26	708.60	2.25
TRI-0-3	0	54.74	133.44	720.10	2.29
TRI-0-5	0	54.82	133.48	705.99	2.24
TRI -0-7	0	55.26	133.64	721.22	2.25
TRI -0-12	0	54.80	132.00	716.02	2.30
TRI -0-15	0	54.80	134.12	721.53	2.28
UCS-30-0	30	53.64	138.64	707.60	2.26
TRI -30-3	30	53.70	105.80	538.41	2.25
TRI -30-5	30	54.02	111.18	572.05	2.24
TRI -30-7	30	53.66	106.18	545.34	2.27
TRI -30-12	30	53.66	106.70	544.86	2.26
TRI -30-15	30	53.62	107.26	532.06	2.20
UCS-45-0	45	53.64	134.58	702.07	2.31
TRI -45-3	45	53.64	131.80	672.50	2.26
TRI -45-5	45	53.64	136.50	684.85	2.22
TRI -45-7	45	53.54	126.46	649.26	2.28
TRI -45-12	45	53.64	98.54	473.04	2.12
TRI -45-15	45	53.74	106.00	543.14	2.26
UCS -60-0	60	53.64	131.38	672.31	2.26
TRI -60-3	60	53.64	133.52	674.71	2.24
TRI -60-5	60	53.64	132.60	674.98	2.25
TRI -60-7	60	53.74	100.38	512.96	2.25
TRI -60-12	60	53.64	104.60	532.89	2.25
TRI -60-15	60	53.64	105.20	533.63	2.24
UCS-90-0	90	53.68	103.64	529.67	2.26
TRI -90-3	90	54.92	106.00	540.67	2.15
TRI -90-5	90	53.64	108.14	549.42	2.25
TRI -90-7	90	53.64	107.40	542.13	2.23
TRI -90-12	90	53.64	104.50	527.79	2.23
TRI -90-15	90	54.00	100.96	502.79	2.17

Table 3.3 Gypsum specimens prepared for Brazilian tension test.

Specimen No.	β (Degrees)	Diameter (mm)	Length (mm)	Weight (g)	Density (g/cc)
BZ-0	0	99.34	51.22	887.51	2.24
BZ-30	30	99.42	48.46	867.45	2.31
BZ-45	45	98.90	50.03	846.00	2.20
BZ-60	60	98.82	49.44	877.55	2.32
BZ-90	90	99.42	49.82	874.56	2.26



CHAPTER IV

LABORATORY TEST METHOD AND APPARATUS

4.1 Introduction

This chapter describes the test methods, apparatus, and calculation of strengths and elastic parameters on transverse isotropic specimens, of which include: under ultrasonics pulse velocity measurements, compression test under various confining pressures, and Brazilian tension test. The five elastic parameters based on generalized Hooke's law, considered here, include E and E' (elastic moduli parallel and normal to strike of transverse isotropic plane), ν and G (Poisson's ratio and shear modulus on transverse isotropic plane), and ν' and G' (Poisson's ratio and shear modulus on the plane normal to transverse isotropic plane).

4.2 Ultrasonic pulse velocity measurements

Wave velocity measurement is performed on the compression specimens before loading. The specimens have $L/D = 2.0$. Sonic viewer 170 (Model 5338) is used to measure the P- and S-wave velocities, as shown in Figure 4.1. The end surfaces of the specimens are flattened and smoothen to provide tight contacts with transmitter and receiver transducers. The direct transmission method is conducted for measuring of compressional (P-wave) and shear (S-wave) waves velocities to calculate the dynamic elastic parameters of the specimen based on the standard practice (ASTM D2845).

Liao et al. (1997) proposed a testing method to determine the 5 dynamic elastic constants based on generalized Hooke's law for transverse isotropic rock, using the 5 independent ultrasonics wave phase velocities. These parameters include:

- VP_{0° and VP_{90° represent P-wave velocities for the bedding-perpendicular and the bedding-parallel (Figure 4.2), respectively.
- VSh_{0° and VSh_{90° represent S-wave velocities for the bedding-perpendicular and the bedding-parallel, respectively. They are called intrinsic parameters.

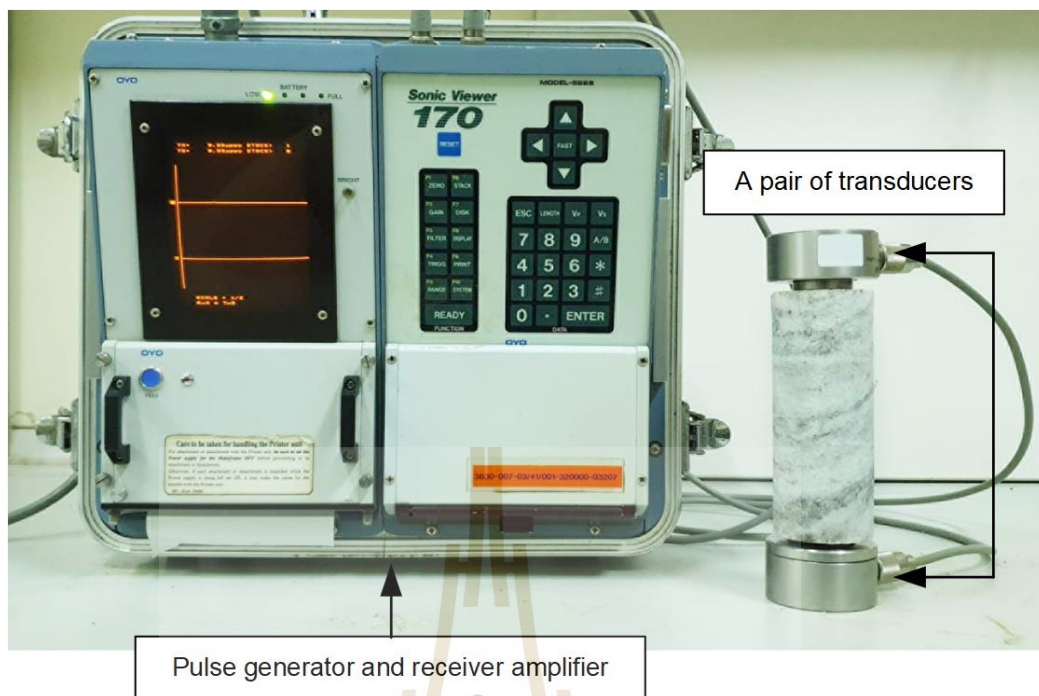


Figure 4.1 Wave velocity measurement device: sonic viewer and transmitter and receiver transducers.

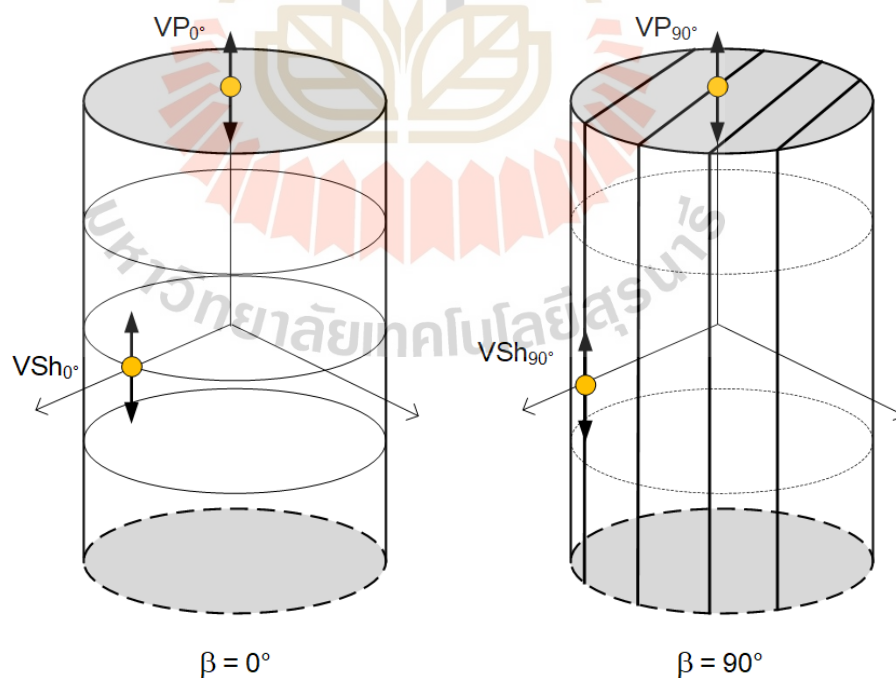


Figure 4.2 Four independent parameters used in the ultrasonics wave velocity measurements (Grgic et al., 2019), for $\beta = 0^\circ$ and 90° .

- VP_{45° is a P-wave along the direction $\theta=45^\circ$, where θ is the angle between the wave vector normal to the wavefront and the symmetry axis along x-direction (Figure 4.3). However, the direct measurement of the phase velocity along oblique direction is very complicated. To determine VP_{45° , Byun (1984) and Byun and Cheng (1986) present the concept of the wave surface determined by group (ray) velocity, which is the velocity of the actual energy propagation. The assumption is that the actual wave surface of energy propagation from a point source is an ellipsoid. The phase velocity (VP_{45°) is obtained by following equations:

$$VP_{45^\circ} = V(\phi) \cos(\phi - 45^\circ) \quad (4.1)$$

where

$$V(\phi) = [(VP_{90^\circ}^4 + VP_{0^\circ}^4) / (VP_{90^\circ}^2 + VP_{0^\circ}^2)]^{0.5}$$

$$\phi = \tan^{-1}(VP_{90^\circ}^2 / VP_{0^\circ}^2)$$

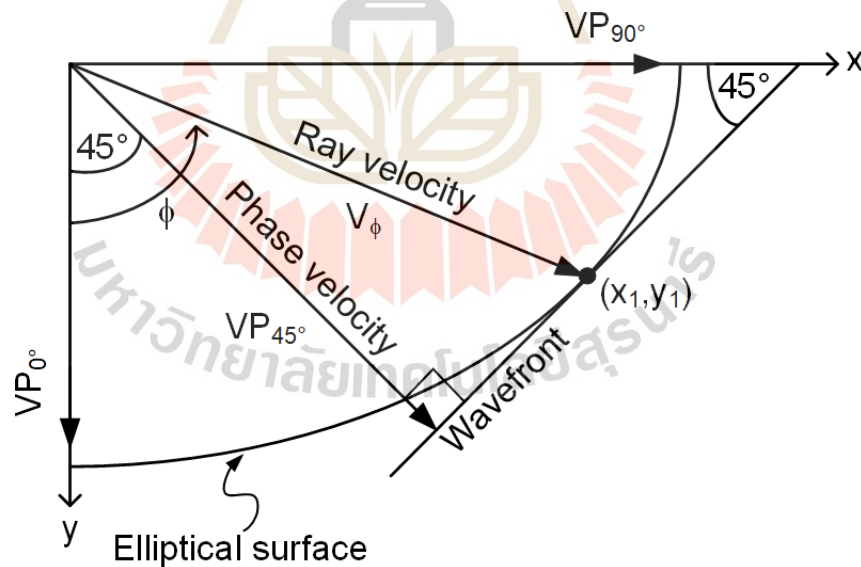


Figure 4.3 Diagram showing the relationship between the phase velocity VP_{45° and the group velocity $V(\phi)$ (Song et al., 2004).

For wave velocity applications, Hooke's law may be rewritten in terms of the stress-strain relationship according to the Voigt reduced notations as;

$$\begin{bmatrix} \sigma_1 \\ \sigma_2 \\ \sigma_3 \\ \sigma_4 \\ \sigma_5 \\ \sigma_6 \end{bmatrix} = \begin{bmatrix} C_{11} & C_{12} & C_{13} & 0 & 0 & 0 \\ C_{12} & C_{11} & C_{13} & 0 & 0 & 0 \\ C_{13} & C_{13} & C_{33} & 0 & 0 & 0 \\ 0 & 0 & 0 & C_{44} & 0 & 0 \\ 0 & 0 & 0 & 0 & C_{44} & 0 \\ 0 & 0 & 0 & 0 & 0 & \frac{C_{11}-C_{12}}{2} \end{bmatrix} \begin{bmatrix} \varepsilon_1 \\ \varepsilon_2 \\ \varepsilon_3 \\ \varepsilon_4 \\ \varepsilon_5 \\ \varepsilon_6 \end{bmatrix} \quad (4.2)$$

where σ and ε are stresses and strains, C_{ij} is elasticity stiffness matrix ($i, j = 1, 2, 3$). Equation (4.2) also contains 5 compliance components: C_{11} , C_{12} , C_{13} , C_{33} , and C_{44} . These components are directly related to a set of elastic constants E , E' , ν , ν' and G' . Determination of 5 compliance components can be made using the Christoffels equations (Tsvankin, 2001):

$$C_{11} = \rho \cdot VP_{90}^2 \quad (4.3)$$

$$C_{12} = C_{11} - 2\rho \cdot VSh_{90}^2 \quad (4.4)$$

$$C_{33} = \rho \cdot VP_0^2 \quad (4.5)$$

$$C_{44} = \rho \cdot VSh_0^2 \quad (4.6)$$

$$C_{13} = -C_{44} + [4\rho^2 \cdot VP_{45}^4 - 2\rho \cdot VP_{45}^2 (C_{11} + C_{33} + 2C_{44}) + (C_{11} + C_{44})(C_{33} + C_{44})]^{0.5} \quad (4.7)$$

From Equations (4.3) through (4.7), the five elastic constants can be obtained as:

$$E = 1/a_{11} ; E' = 1/a_{33} ; \nu = a_{12}/a_{11} ; \nu' = -a_{13}/a_{33} ; G' = 1/a_{44} \quad (4.9)$$

where

$$a_{11} = (C_{11}C_{33} - C_{13}^2) / [(C_{11} - C_{12})(C_{11}C_{33} + C_{12}C_{33} - 2C_{13}^2)]$$

$$a_{33} = (C_{11} + C_{12}) / (C_{11}C_{33} + C_{12}C_{33} - 2C_{13}^2)$$

$$a_{12} = (C_{13}^2 - C_{12}C_{33}) / [(C_{11} - C_{12})(C_{11}C_{33} + C_{12}C_{33} - 2C_{13}^2)]$$

$$a_{13} = (-C_{13}) / (C_{11}C_{33} + C_{12}C_{33} - 2C_{13}^2)$$

$$a_{44} = 1/C_{44}$$

4.3 Compression test

The uniaxial and triaxial compressive strengths and elastic parameters are determined by axially loading the specimens under constant rate of 0.1 MPa/s (ASTM D7012-14e1). The specimens are loaded under confining pressures from 0, 3, 5, 7, 12 to 15 MPa. The tests are performed by increasing the axial stress until failure occurs. The axial and lateral displacements are monitored using dial gauges and strain gages, respectively. Strain gages are installed parallel and normal to bedding planes (Figure 4.4).

The stresses and strains under triaxial compression can be calculate the elastic parameters of transverse isotropy based on general Hooke's law, as follows (Jaeger et al., 2007):

$$\varepsilon_1 = \sigma_1/E_1 - \nu_{1,3P} \sigma_3/E_{3P} - \nu_{1,3O} \sigma_3/E_{3O} \quad (4.10)$$

$$\varepsilon_{3P} = -\nu_{1,3P} \sigma_1/E_1 + \sigma_3/E_{3P} - \nu_{3P,3O} \sigma_3/E_{3O} \quad (4.11)$$

$$\varepsilon_{3O} = -\nu_{1,3O} \sigma_1/E_1 - \nu_{3P,3O} \sigma_3/E_{3P} + \sigma_3/E_{3O} \quad (4.12)$$

where σ_1 and σ_3 are the major and minor principal stresses, ε_1 is the major principal strain, and ε_{3P} and ε_{3O} are the strains measured parallel and normal to the strike of bedding planes. Assuming that the specimens are linearly elastic, E_1 is the elastic moduli along the major principal (axial) direction, and E_{3O} and E_{3P} are along the two minor principal (lateral) axes normal and parallel to bedding plane strike, respectively. $\nu_{1,3P}$ and $\nu_{1,3O}$ are Poisson's ratios on the planes between the major principal axis and the directions that are parallel and normal to the strike of bedding planes. The $\nu_{3P,3O}$ is Poisson's ratio between the directions that are parallel and normal to the bedding plane strike. The notations and directions of elastic parameters are shown in Figure 4.5.

For $\beta = 0^\circ$ and 90° , the elastic moduli and Poisson's ratios under unconfined conditions can be readily calculated from equation (4.10) to (4.12). Regression analysis using SPSS code (Wendai, 2000) are performed to determine the elastic parameters of the specimens with $0^\circ < \beta < 90^\circ$. The regression uses the stresses and their corresponding strains obtained from linear portion of the curves for each specimen at

about 40-50% peak stress. The parameters E and E' are equivalent to E_1 values for $\beta = 90^\circ$ and 0° , and ν and ν' are equivalent to $\nu_{1,3P}$ and $\nu_{1,30}$ for $\beta = 90^\circ$. The G' is often expressed in term of E , E' , ν , ν' through the following equations:

$$1/G' = 1/E + 1/E' + 2\nu'/E' \quad (4.13)$$

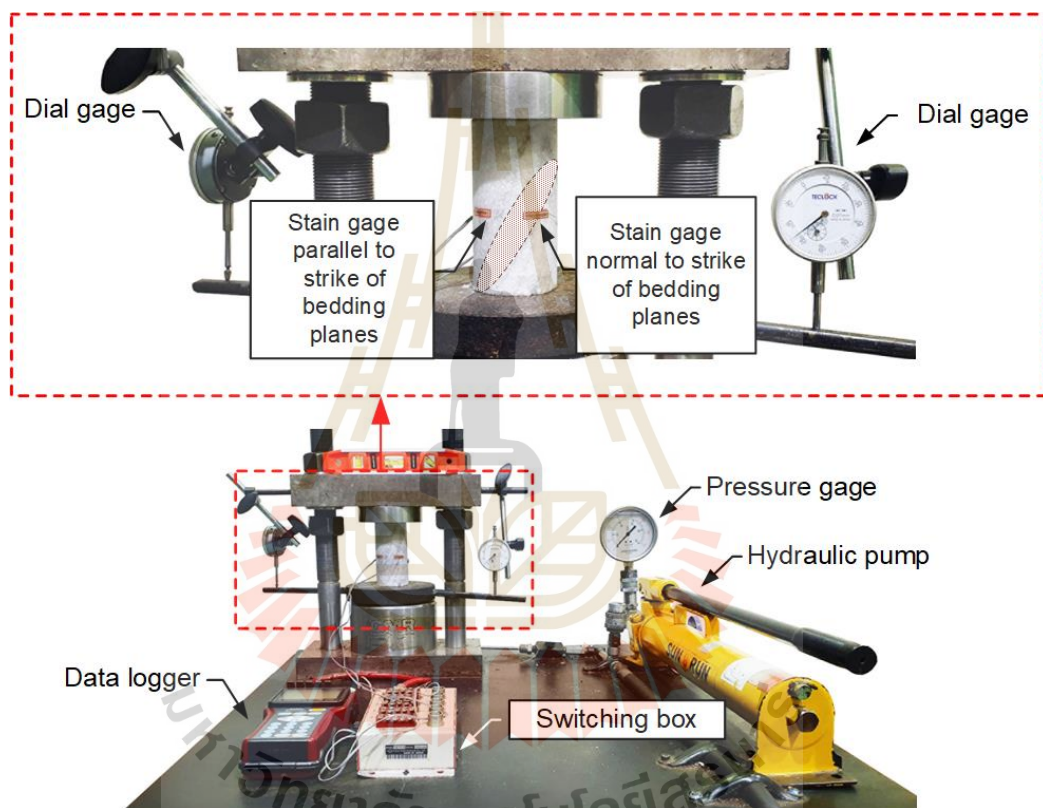


Figure 4.4 Laboratory arrangement for compression testing.

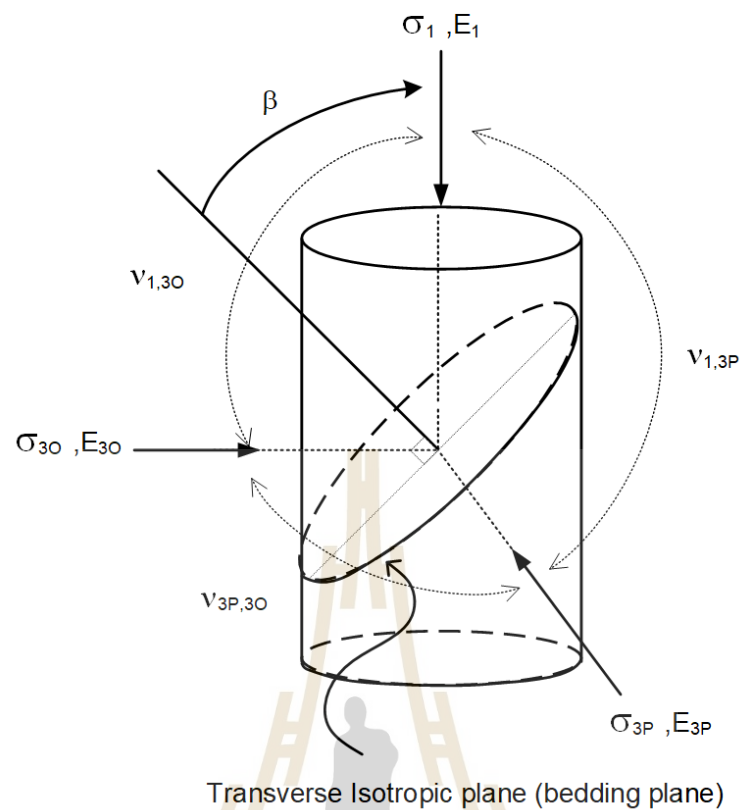


Figure 4.5 Definition of elastic parameters under compression test.

4.4 Brazilian tension test

The Brazilian tension test is performed to determine tensile strengths and elastic parameters of the gypsum specimens under tension. The load configuration uses flat platens (Figure 4.6a). The loading rate is controlled at approximately 0.1 MPa/s (ASTM D3967-16). Strain gages are installed to measure tensile and compressive strains at the center of the specimen. Gage length is 10 mm. The gages are installed parallel and normal to the loading direction (Figure 4.6b).

The strain results are induced by compressive and tensile stresses at the specimen center as result of the applied the vertical stresses at the specimen center. The tensile elastic parameters can be determined based on the general Hooke's law, as follows (Jaeger et al., 2007):

$$\varepsilon_x = \sigma_x / E_{T(90-\beta)} - \nu_T \sigma_y / E_{C(\beta)} \quad (4.14)$$

$$\varepsilon_y = \sigma_y / E_{C(\beta)} - \nu_T \sigma_x / E_{T(90-\beta)} \quad (4.15)$$

where ε_x is strain in x-direction (lateral), ε_y is strain in y-direction (axial). $E_{T(90-\beta)}$ is tensile elastic modulus with strain gage (lateral) normal to loading axis where the angle β is the angle between loading direction and the normal of bedding planes, as shown in Figure 4.7. The parameter ν_T is the Poisson's ratios on the plane between the loading axis and the directions that are normal to loading axis, σ_x is the Brazilian tensile stress, σ_y is compression with the magnitudes of three times the Brazilian tensile stress. $E_{C(b)}$ is compressive elastic modulus, obtained from the uniaxial test condition. The parameters E and E' under tensile condition are equivalent to E_T values for $\beta = 0^\circ$ and 90° , and ν and ν' are equivalent to ν_T for $\beta = 0^\circ$ and 90° . The intrinsic shear modulus G' can be determined by using Equation (4.13).

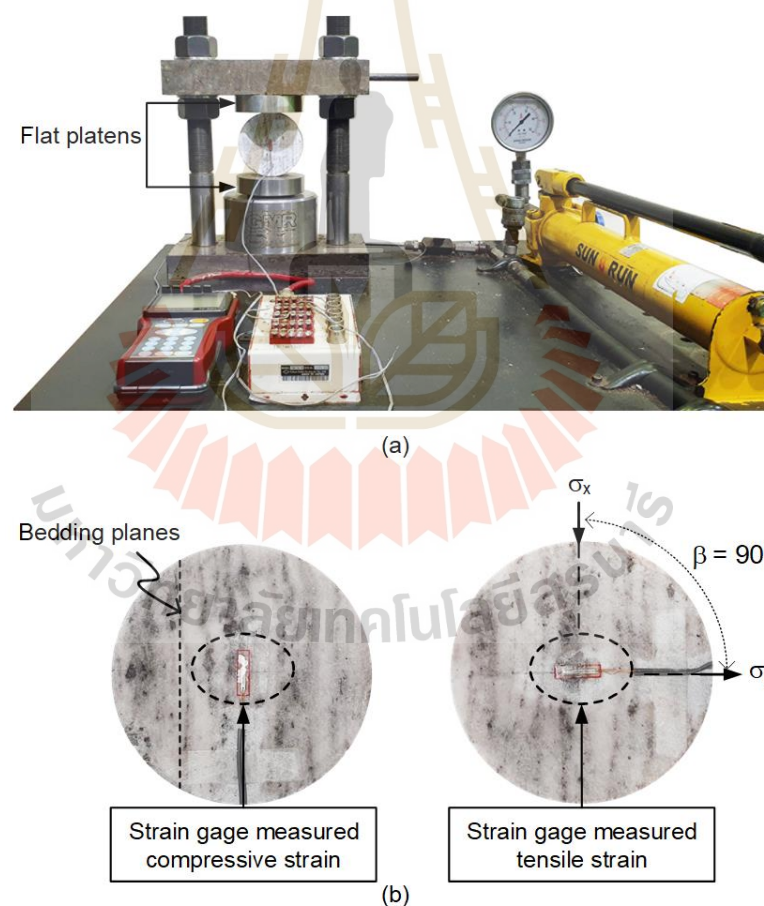


Figure 4.6 Laboratory arrangement for Brazilian tension testing (a) and locations of two strain gages on specimen with $\beta=90^\circ$ (b).

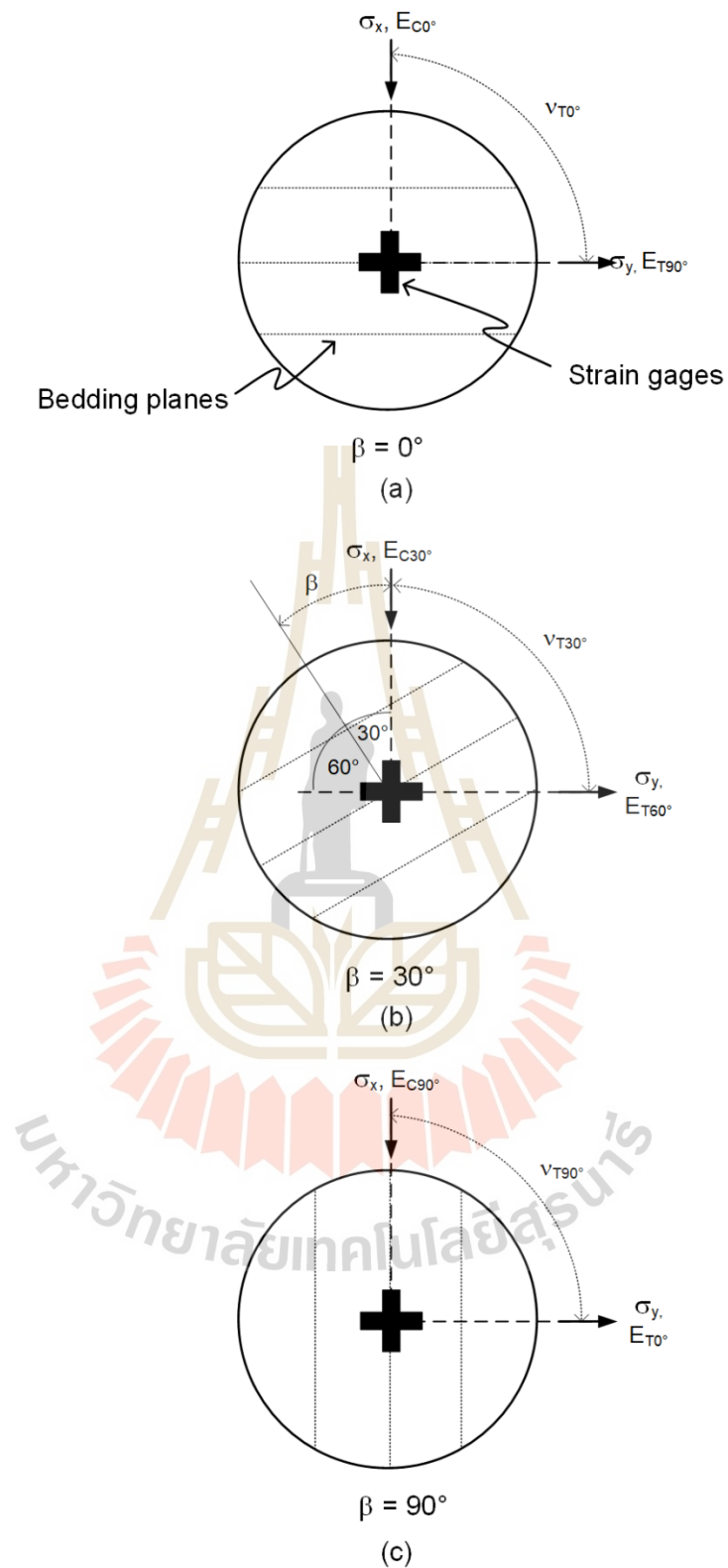


Figure 4.7 Notations of elastic parameters for some Brazilian tension test specimens with $\beta = 0^\circ$ (a), 30° (b), and 90° (c).

CHAPTER V

TEST RESULTS

5.1 Introduction

Described in this chapter are the results of laboratory experiments. The effects of bedding plane orientations on wave velocities, compressive and tensile strengths, and elastic parameters are also determined from the results.

5.2 Ultrasonic pulse velocity results

5.2.1 Wave velocities

The averaged values of P- and S-waves of the specimens for each bedding plane angle are presented in Table 5.1. The specimens with $\beta = 0^\circ$ have the lowest V_p and V_s of 1.98 and 1.07 km/s. When $\beta = 90^\circ$, the specimens have the highest V_p and V_s equal to 2.83 and 1.54 km/s. Figure 5.1 indicates that the wave velocities increase with increasing bedding plane dip angles. The highest values are about 1.5 times of the lowest ones. The change of wave velocity is may be due to the reflection and refraction of waves occur at the interface between the bedding planes, consequently the wave energy is loss. For $\beta=90^\circ$, the specimens give higher wave velocities than those with $\beta=0^\circ$ because $\beta=90^\circ$ they have fewer interfaces when wave propagate through the specimen.

5.2.2 Dynamic elastic parameters of transversely isotropic rock

The measured velocities in Table 5.1 are used to determine the 5 compliance components using Equations (4.3) through (4.7). The dynamic elastic parameters are determined from the known complete compliance components using Equations (4.9). Table 5.2 shows the calculated results. The elastic moduli and Poisson's ratio parallel to the bedding plane strike (E and ν) are greater than those normal to the strike (E' and ν').

Table 5.1 Averaged values of P- and S-waves for each orientations.

β (Degrees)	Vp (km/s)	Vs (km/s)
0	1.98 ± 0.11	1.07 ± 0.06
30	2.14 ± 0.16	1.24 ± 0.08
45	2.34 ± 0.18	1.31 ± 0.12
60	2.46 ± 0.17	1.38 ± 0.12
90	2.83 ± 0.19	1.54 ± 0.15

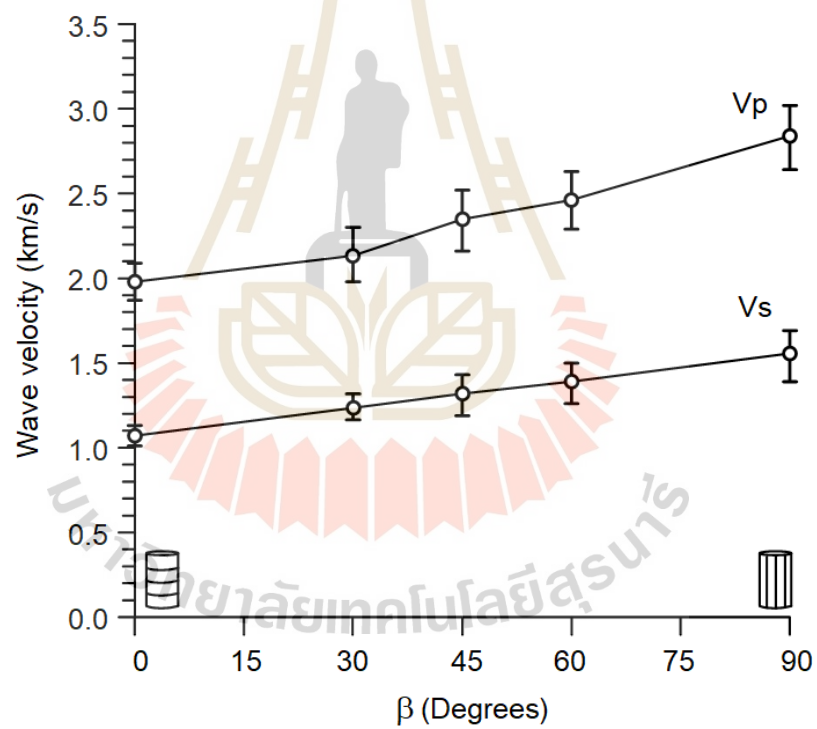


Figure 5.1 Wave velocities as a function of bedding plane orientations.

Table 5.2 Dynamic elastic parameters of transverse isotropic gypsum specimens.

Five independent wave velocities		Compliance components		Dynamic elastic parameters	
VP _{0°}	1.98	C ₁₁	18.02	E (GPa)	13.98
VP _{90°}	2.83	C ₁₂	7.35	E' (GPa)	7.05
VSh _{0°}	1.07	C ₃₃	8.82	ν	0.19
VSh _{90°}	1.54	C ₄₄	2.58	ν'	0.31
VP _{45°}	2.34	C ₁₃	4.74	G' (GPa)	2.58

5.3 Compression test results

5.3.1 Compressive strengths

Typical stress-strain curves under various bedding orientations and confining pressures of 0, 3, 5, 7, 12, and 15 MPa are shown in Figure 5.2. The lateral strains are smaller than the axial strains, reflecting brittleness of rocks. Axial strains are largest in case of the $\beta=0^\circ$ due to crack closure and compaction of the void along the bedding planes. When $\beta=90^\circ$, the axial strain is enhanced by the bedding planes.

The plots of compressive strengths as a function of angle β at different confining pressures are presented in Figure 5.3. The results show that the maximum strengths are observed at $\beta=0^\circ$ and the minimum strengths are observed at $\beta=60^\circ$. All bedding plane orientations show that the strengths increase with increasing confining pressures. The shape of compressive strengths is U-shaped pattern in the lower range of confining pressures. The changing trend of compressive strengths is related to failure pattern. For angle $\beta=0^\circ$, parallel extensile cracks across the beds and locally shearing cracks along beds. For $\beta=30^\circ$, shear failure occurs across beds while fractures on angles $\beta=45-60^\circ$ are along the interface of the beds because shear stresses are greater than shear strength of the interface. As a result sliding failure occurred. When angle $\beta=90^\circ$, the failure mode is extensile splitting failure along the beds (Figure 5.4).

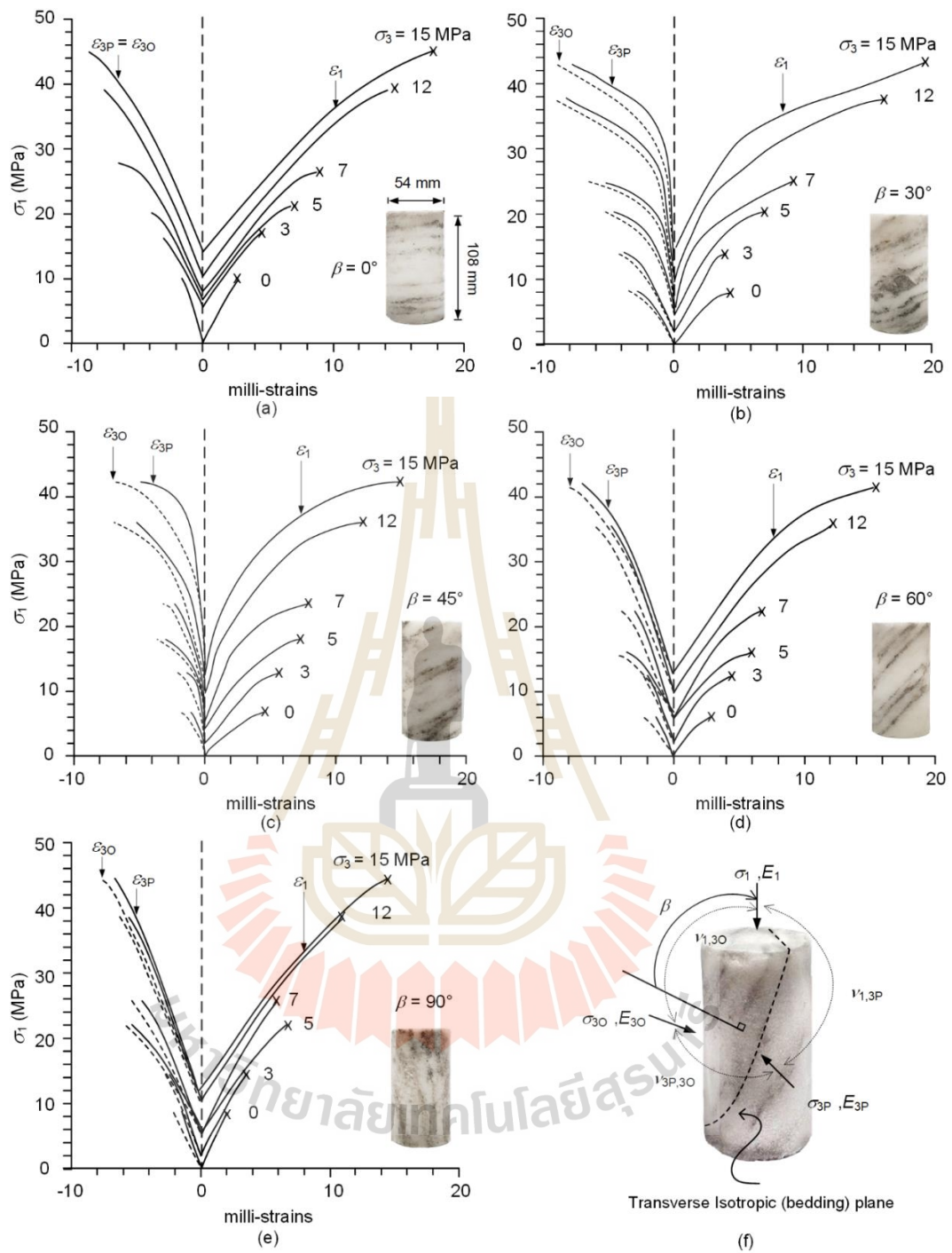


Figure 5.2 Stress-strain curves of gypsum specimens with $\beta = 0^\circ$ (a), 30° (b), 45° (c), 60° (d), and 90° (e). Notations used in Table 5.3 (f).

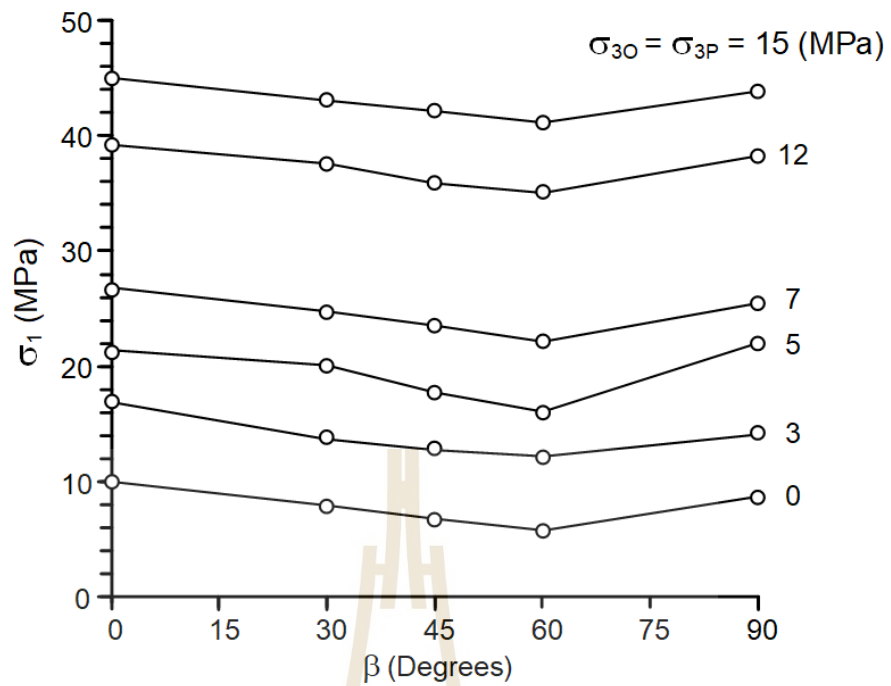


Figure 5.3 Compressive strengths as a function of bedding plane orientations β .



Figure 5.4 Some post-test specimens with different bedding plane angles.

5.3.2 Elastic parameters

Table 5.3 gives the elastic parameters calculated from Equations (4.10) through (4.12). Under low confining pressures, the elastic moduli parallel to bedding plane strike (E_{3P}) are greater than those normal to the strike (E_{30}) which can be clearly observed for $\beta = 90^\circ$. The stiffness discrepancies decrease with the angles β . The two moduli are equal for $\beta = 0^\circ$ (σ_1 is normal to bedding planes). Under high confinement, the elastic moduli for all angles are comparable.

Similar behavior is observed for the Poisson's ratios. Under low confining pressures, the Poisson's ratios parallel to bedding plane strike ($\nu_{1,3P}$) are slightly lower than those normal to the bedding plane strike ($\nu_{1,30}$). For $\beta = 0^\circ$, the two Poisson's ratios are equal while $\nu_{3P,30}$ is lower than the two. Under high confinement, the Poisson's ratios measured from all planes are comparable.

5.4 Brazilian tension test results

5.4.1 Tensile strengths

Figure 5.5 shows the stress-strain curves from Brazilian tension test. The tensile strength changes with bedding plane orientations. It is observed that the tensile strength is maximum (0.77 MPa) when $\beta = 0^\circ$ and decreases rapidly with increasing angle β (Figure 5.6). Figure 5.7 presents the fracture pattern on one side of the specimens. The smaller angles, $\beta = 0^\circ$ and 30° , the stress states tend to be under compression and the interface cannot easily fail. While larger angle, $\beta = 45^\circ - 90^\circ$, the stress states are under shearing and tension and interface more easily slip due to shearing and tension. Due to the shear and tensile strengths of bedding planes are weak.

Table 5.3 Compression test results

β	σ_3 (MPa)	$\sigma_{1,f}$ (MPa)	E_1 (GPa)	E_{3P} (GPa)	E_{3O} (GPa)	$\nu_{1,3P}$	$\nu_{1,3O}$	$\nu_{3P,3O}$
0°	0	9.86	3.34	-	-	0.27	0.27	-
	3	16.90	4.00	8.06	8.06	0.26	0.26	0.21
	5	21.13	4.85	8.11	8.11	0.26	0.26	0.20
	7	26.51	5.54	8.28	8.28	0.25	0.25	0.20
	12	39.14	6.69	8.46	8.46	0.24	0.24	0.20
	15	44.89	7.85	8.93	8.93	0.22	0.22	0.20
30°	0	7.89	3.79	-	-	0.26	0.30	-
	3	13.71	4.48	8.04	6.07	0.25	0.29	0.23
	5	20.10	5.33	8.12	6.74	0.24	0.27	0.23
	7	24.68	6.01	8.29	7.24	0.25	0.26	0.22
	12	37.48	7.10	8.47	7.89	0.23	0.24	0.21
	15	42.96	8.22	8.93	8.73	0.22	0.22	0.21
45°	0	6.71	4.49	-	-	0.25	0.32	-
	3	12.78	5.34	8.03	5.07	0.24	0.29	0.24
	5	17.79	5.94	8.10	5.89	0.23	0.28	0.23
	7	23.39	6.67	8.28	6.51	0.24	0.27	0.23
	12	35.86	7.31	8.46	7.42	0.22	0.25	0.30
	15	42.09	8.31	8.93	8.54	0.21	0.23	0.20
60°	0	5.84	6.32	-	-	0.24	0.31	-
	3	12.12	6.66	8.05	4.44	0.23	0.29	0.26
	5	15.98	7.03	8.08	5.29	0.22	0.28	0.25
	7	22.10	7.27	8.28	5.97	0.22	0.27	0.23
	12	35.00	7.72	8.45	7.03	0.22	0.24	0.23
	15	41.11	8.51	8.96	8.36	0.20	0.22	0.23
90°	0	8.51	8.02	-	-	0.20	0.27	-
	3	14.28	8.06	8.06	4.00	0.21	0.26	0.21
	5	22.04	8.11	8.11	4.85	0.20	0.25	0.20
	7	25.48	8.28	8.28	5.54	0.20	0.25	0.20
	12	38.16	8.46	8.46	6.69	0.20	0.24	0.20
	15	43.81	8.93	8.93	7.85	0.20	0.22	0.20

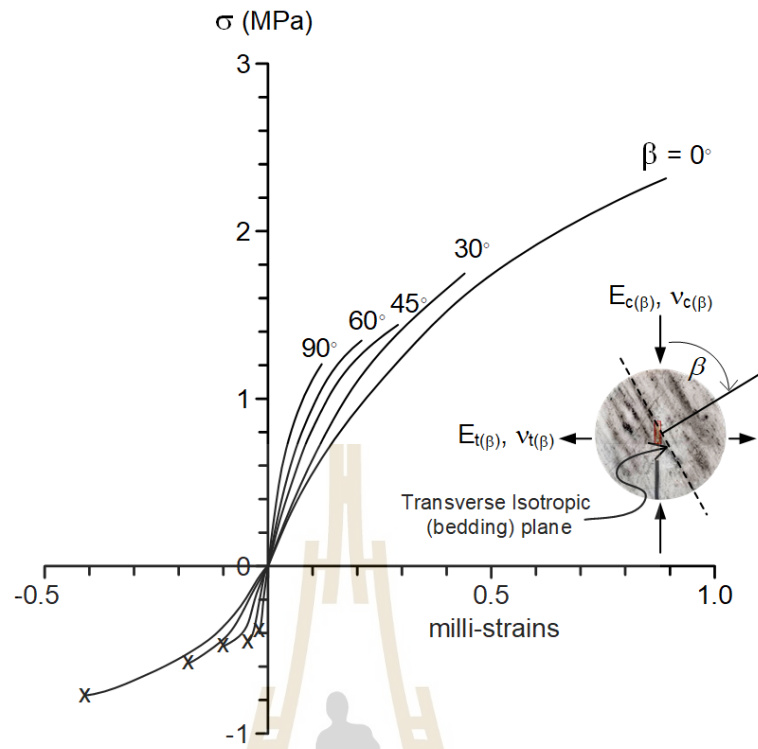


Figure 5.5 Stress-strain curves from Brazilian tension test.

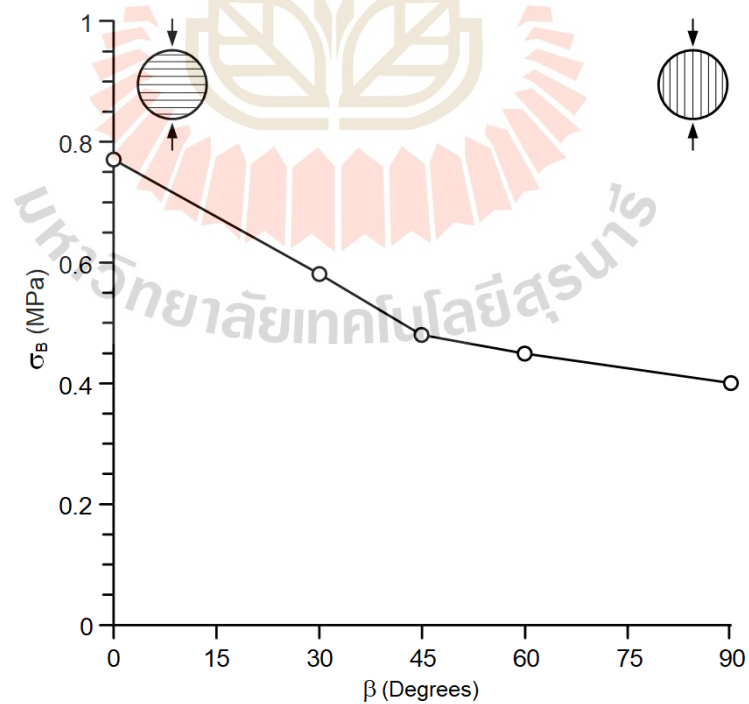


Figure 5.6 Brazilian tensile strengths (σ_B) as a function of bedding plane orientations.

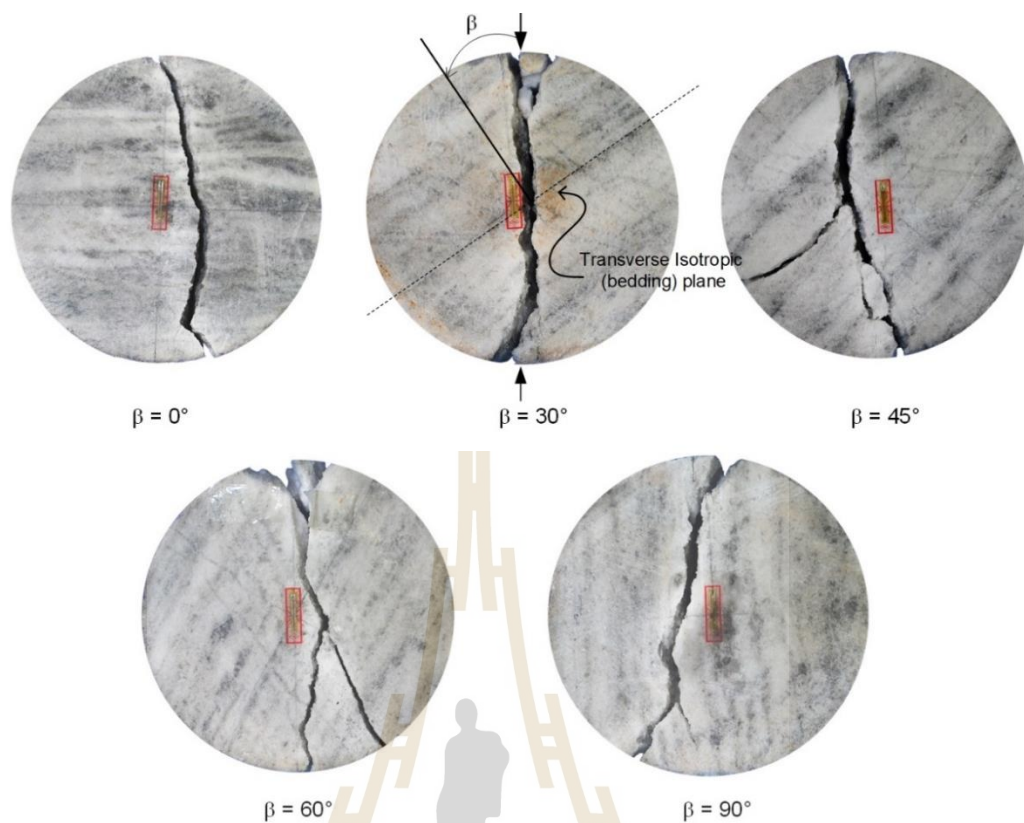


Figure 5.7 Post-tests Brazilian tension test specimens for various bedding plane angles β .

5.4.2 Tensile elastic modulus

The compressive elastic modulus (E_1 , shown in Table 5.3) can be substituted to Eq (4.14) through (4.15) to calculate the tensile elastic and Poisson's ratio for each bedding plane orientation. According to the Brazilian tension test, the tension elastic modulus tends to occur at the center of the disc perpendicular to the loading direction. For angle $\beta = 0^\circ$, the tensile elastic modulus occurs parallel to the bedding plane. For angle $\beta = 90^\circ$, the tensile elastic modulus occurs perpendicular to the bedding plane. Figure 5.8a shows that the tensile elastic modulus parallel to the bedding plane (E_{T90°) at angle $\beta = 0^\circ$ is maximum and decreases until the tensile elastic modulus is perpendicular to the bedding plane (E_{T0°) at angle $\beta = 90^\circ$. Poisson's ratio decreases with increasing angle β (Figure 5.8b).

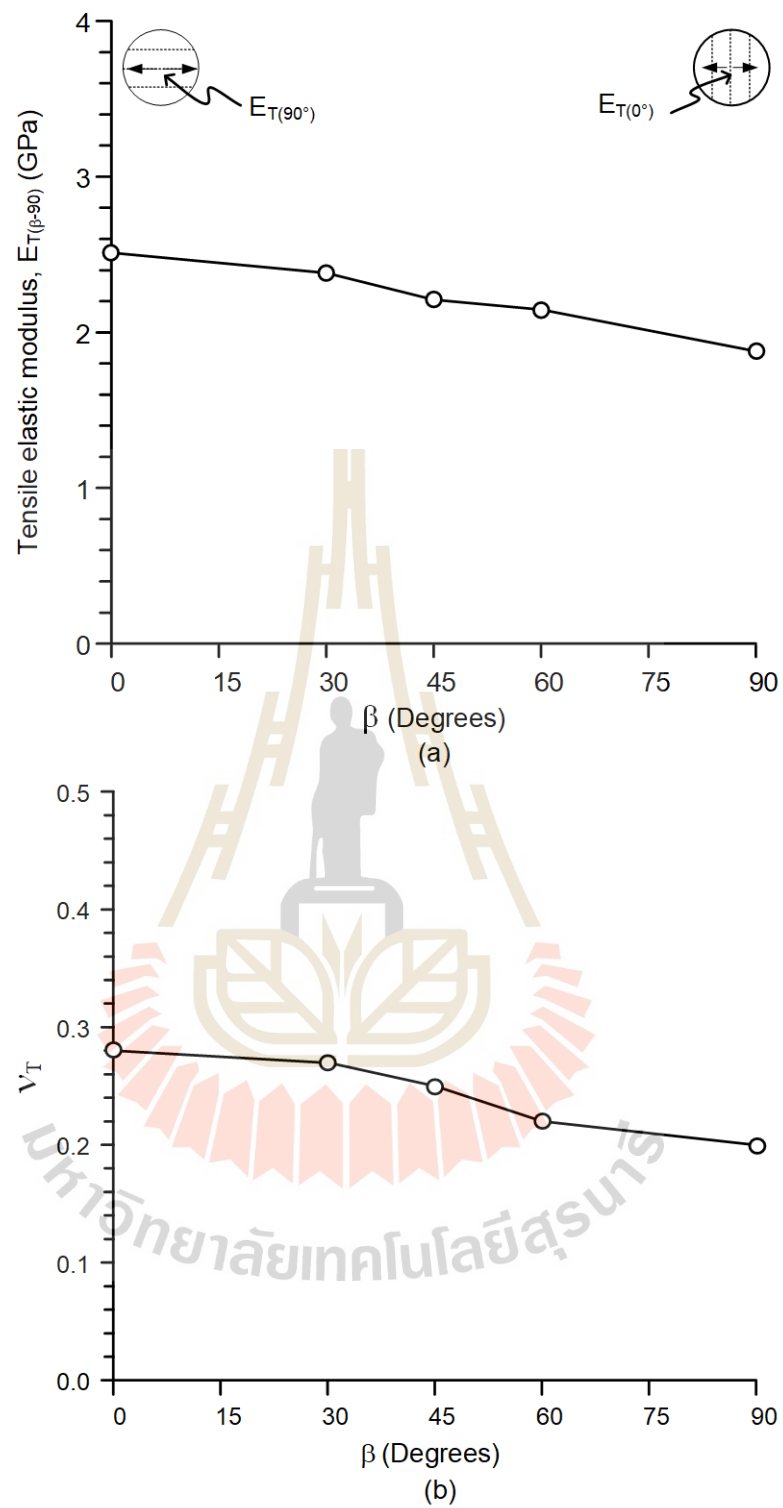


Figure 5.8 Tensile elastic modulus (a) and Poisson's ratio (b) as a function of bedding plane orientations.

CHAPTER VI

ANALYSIS OF TEST RESULTS

6.1 Introduction

The objective of this chapter is to determine the effect of transverse isotropic on ultrasonic wave velocity, elastic modulus, and strength parameters under different bedding plane directions. An approximate solution proposed by Amadei (1996) is used to calculate the apparent elastic moduli and Poisson's ratio. The Coulomb and strain energy criteria are used to describe the strengths and elastic parameters obtained from various bedding plane orientations.

6.2 Transverse isotropic effect on wave velocities

The linear relationships are proposed to correlate the P- and S-wave velocities with the bedding plane orientations. The results indicate that the increase of bedding plane orientations increases the P- and S-wave velocities. Good correlations are obtained from both P- and S-wave velocities ($R^2 = 0.972$ and $R^2 = 0.999$), as shown in Figure 6.1. The following equations represent their relationship:

$$V_p = 9.6 \times 10^{-3} \cdot \beta + 1.920 \quad \text{km/s} \quad (6.1)$$

$$V_s = 5.2 \times 10^{-3} \cdot \beta + 1.076 \quad \text{km/s} \quad (6.2)$$

6.3 Transverse isotropic effect on elasticity

Based on the test results reported in previous chapter, the calculated five elastic parameters are summarized in Table 6.1. To understand the characteristics of anisotropy rock, the degree of anisotropy is selected as an illustration. Degree of anisotropy can be represented in terms of elastic modulus ratios as E/E' , where E and E' are measured parallel and normal to the bedding plane (Amadei et al., 1986). The results show that the E/E' ratios are between 1.1 and 2.4. This agrees well with Amadei et al. (1986) who states that the ratio for transverse isotropic rocks are between 1 and 4. Figure 6.2 plots the ratio of E/E' as a function of confining pressures.

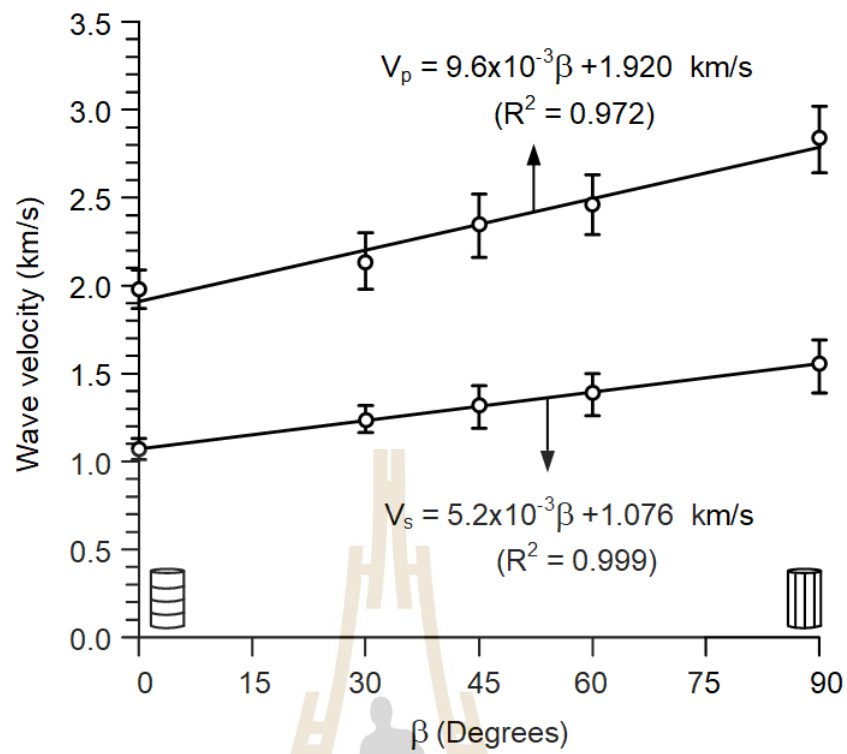


Figure 6.1 Wave velocities as a function of bedding plane orientations.

Table 6.1 Five intrinsic elastic parameters under test conditions.

Test condition	E (GPa)	E' (GPa)	ν	ν'	G' (GPa)	E/E'	
Wave velocity measurements	13.98	7.05	0.19	0.31	2.58	2.0	
Compression test	$\sigma_3 = 0$	8.02	3.34	0.20	0.27	1.71	2.4
	$\sigma_3 = 3$	8.06	4.00	0.21	0.26	1.98	2.0
	$\sigma_3 = 5$	8.11	4.85	0.20	0.25	2.31	1.7
	$\sigma_3 = 7$	8.28	5.54	0.20	0.25	2.55	1.5
	$\sigma_3 = 12$	8.46	6.69	0.20	0.24	2.95	1.3
	$\sigma_3 = 15$	8.93	7.85	0.20	0.22	3.38	1.1
Brazilian tension test	2.51	1.88	0.2	0.28	0.87	1.3	

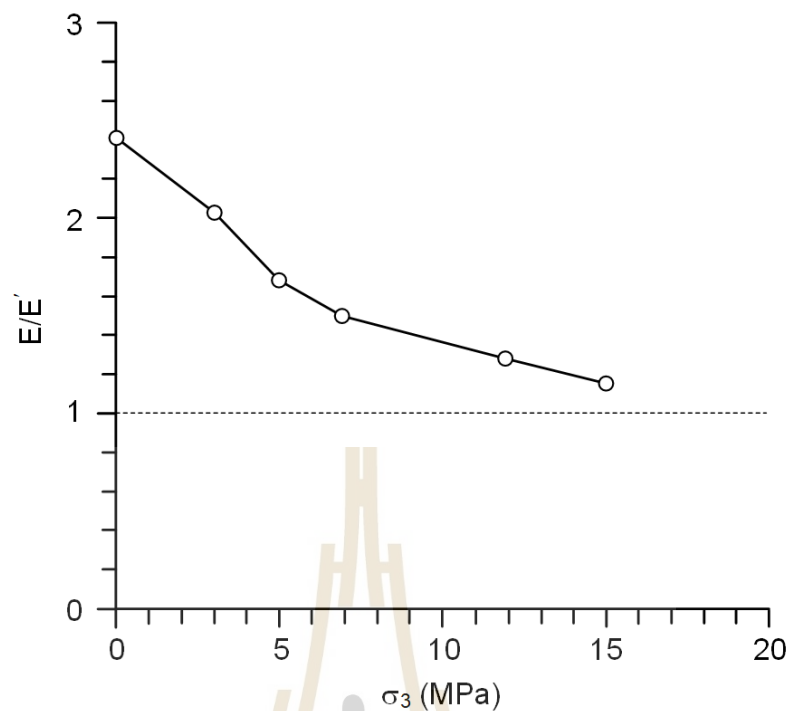


Figure 6.2 Ratio of elastic moduli parallel and normal to bedding plane (E/E') as a function of confining pressures.

They reduce from 2.4 under unconfined condition to 1.1 under confining pressure of 15 MPa. Gypsum tends to become more isotropic as the confining pressure increases. To understand how the degree of anisotropy reduces as the confining pressure increases, the elastic moduli obtained along the major principal (E_1) direction for different angles β are plotted as a function of confining pressure in Figure 6.3. Under unconfined condition, E_{90} (the bedding planes parallel to major principle) is the highest. They slightly increase with confining pressure. The lowest elastic moduli are E_0 (the bedding planes normal to major principle). These elastic moduli increase, as the beds dip away from the major principal axis, as shown by E_{30} , E_{45} and E_{60} . They also increase rapidly toward E_{90} as the confining pressures increase. This indicates that the elastic modulus of a specimen with $\beta = 0^\circ$ is more sensitive to confining pressure. This is because when bedding planes are perpendicular to σ_1 , the pore space in bedding planes is compacted by confining pressure.

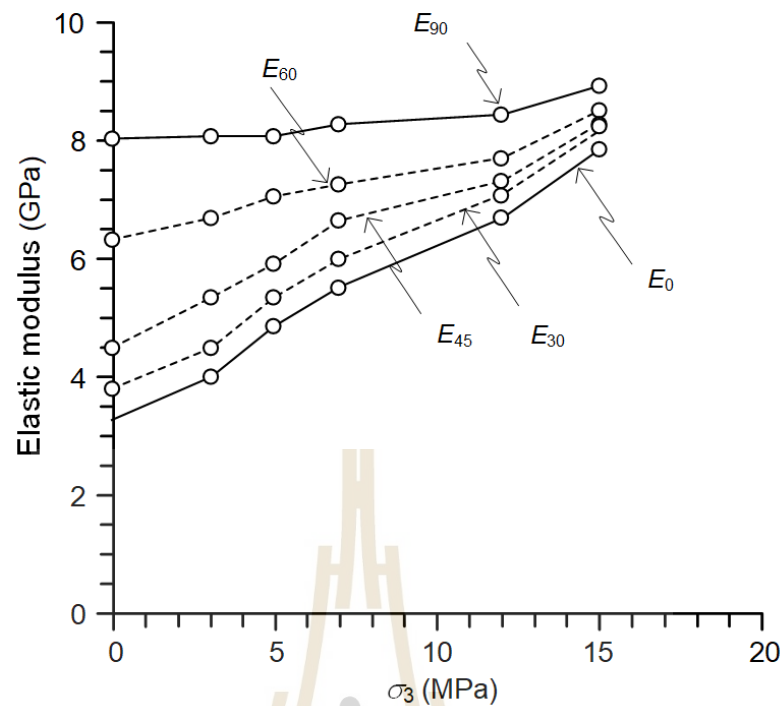


Figure 6.3 Elastic moduli obtained along the major principle (E_1) as a function of confining pressure (σ_3).

6.4 Apparent elastic parameters for transverse isotropy

The theoretical predictions of apparent elastic parameters can be calculated as described by Amadei (1996). He proposes sets of equations to determine the apparent elastic moduli and Poisson's ratios under different orientations of transverse isotropic planes. To accomplish such calculation the intrinsic elastic parameters for angles β equal to 0° and 90° must be known. From generalized Hook's law, Amadei (1996) proposes three initial variables:

$$E_y = 1/a_{22} \quad (6.3)$$

$$\nu_{yx} = a_{12}/a_{22} \quad (6.4)$$

$$\nu_{yz} = a_{23}/a_{22} \quad (6.5)$$

where E_y is apparent Young's modulus, ν_{yx} and ν_{yz} are apparent Poisson's ratios in x-y-z coordinate system, a_{12} , a_{22} and a_{23} are compliance components. These components can be represented in term of transverse isotropic plane angle (β) as follows:

$$a_{22} = \cos^4 \beta / E' + \sin^4 \beta / E + \sin^2 2\beta / 4 (1/G' - 2\nu' / E') \quad (6.6)$$

$$a_{12} = (\nu' / E') \sin^4 \beta - (\nu' / E') \cos^4 \beta + (\sin^2 2\beta / 4) (1/E + 1/E' - 1/G') \quad (6.7)$$

$$a_{23} = (\nu' / E') \cos 2\beta - (\nu / E) \sin^2 \beta \quad (6.8)$$

The five elastic parameters are given in Table 6.1. Substituting these parameters into equation (6.6) through (6.8) and subsequently into equation (6.3) through (6.5), the apparent elastic moduli and Poisson's ratios under all test conditions and bedding plane angles can be determined.

Polar plot provided in Figure 6.4 gives the apparent elastic moduli comparing with the test results from different test conditions. The predictions (solid line) agree well with the experimented test (data point) under all test conditions. The apparent elastic moduli are lower in direction normal than those parallel to bedding plane. The apparent elastic moduli for compression test (Figure 6.4b) show all bedding plane angles become similar as the confining pressure increases to 15 MPa.

The apparent Poisson's ratios on y-x plane (ν_{yx}) and y-z plane (ν_{yz}) slightly depend on the bedding plane orientations (β) (Figure 6.5). However, Poisson's ratio at $0^\circ < \beta < 90^\circ$ cannot be measured under wave velocity measurement (Figure 6.5a,b) and Brazilian tension test (Figure 6.5f). Under compression test, their transverse isotropic responses tend to reduce as the confining pressure increases toward 15 MPa. This agrees with the Amadei's prediction.

6.5 Strength criterion

Strength criteria are used to describe rock failure under different confinements. Here the transverse isotropic effects are incorporated into the Coulomb criterion. The major principal stress at failure ($\sigma_{1,f}$) can be expressed as a function of confining pressure (σ_3) as (Jaeger et al., 2007):

$$\sigma_{1,f} = [(1 + \sin \phi) / (1 - \sin \phi)] \cdot \sigma_3 + (2c \cdot \cos \phi) / (1 - \sin \phi) \quad (6.9)$$

where c and ϕ are cohesion and internal friction angle. Figure 6.6 plots the Coulomb criterion for all bedding plane angles, β . The regression results show good correlations ($R^2 > 0.9$). The multiplier of σ_3 represents slope of the curves and the last term on the right side of equation (6.3) is the intercept on $\sigma_{1,f}$ axis.

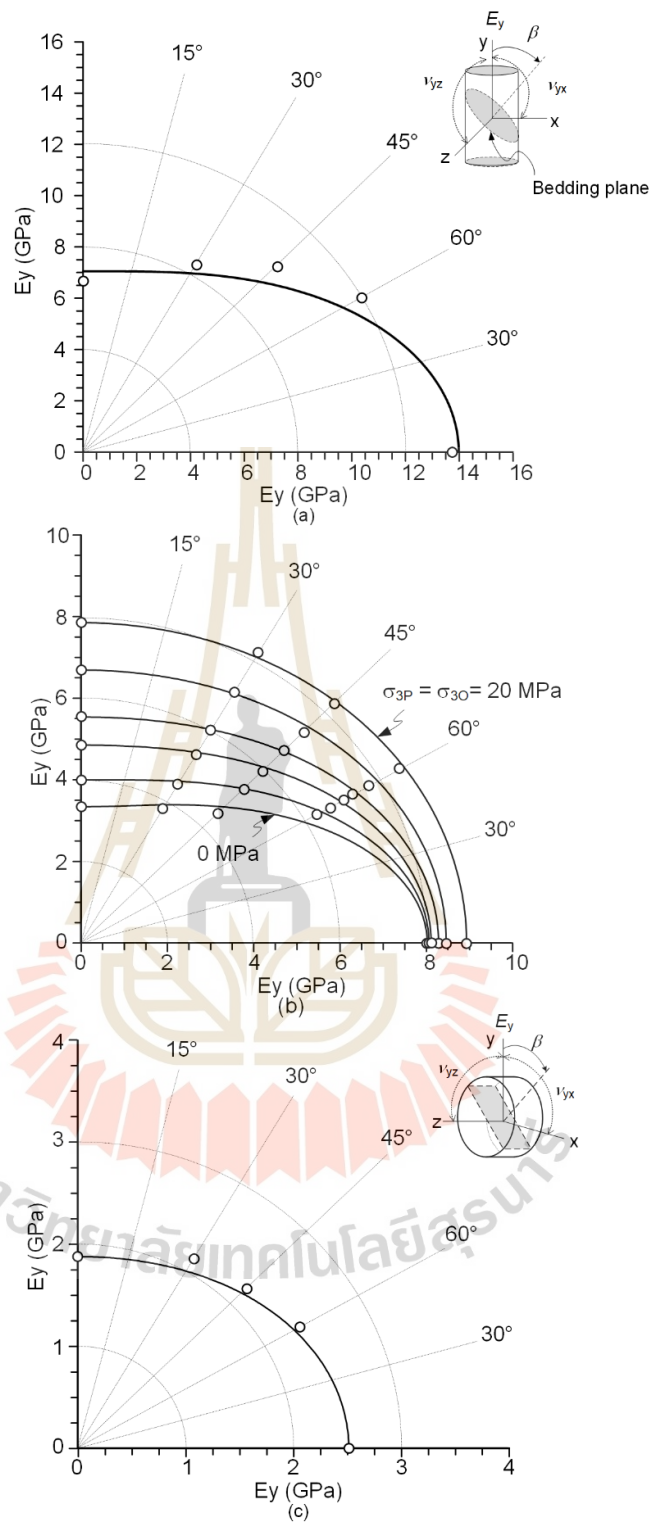


Figure 6.4 Polar plots of apparent elastic moduli (E_y) under different bedding plane angles (β) of three test conditions: (a) wave velocity measurements, (b) compression test, and (c) Brazilian tension test.

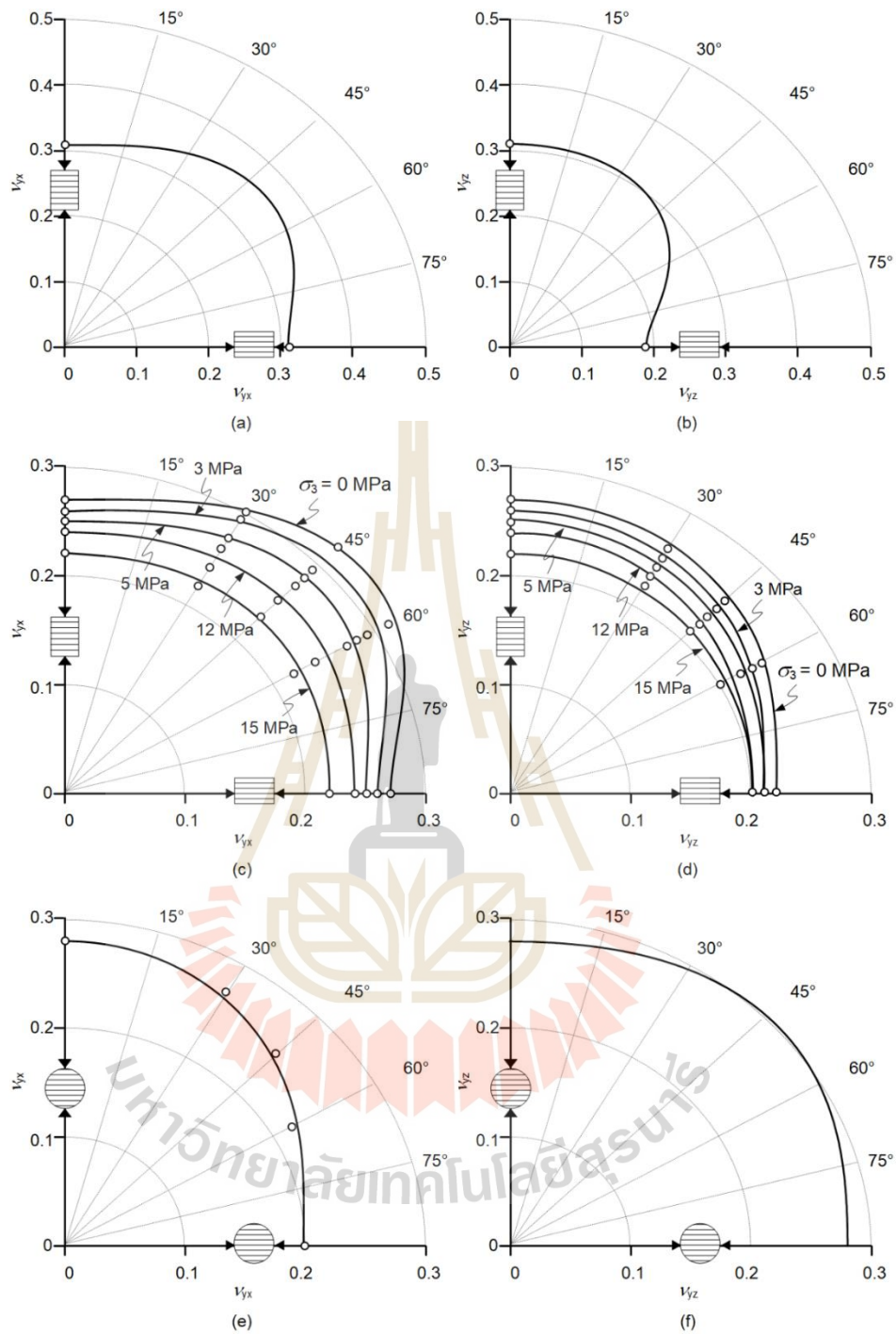


Figure 6.5 Polar plots of apparent Poisson's ratios v_{yx} and v_{yz} under different bedding plane angles (β) on three test conditions: (a,b) wave velocity measurements, (c,d) compression test, and (e,f) Brazilian tension test.

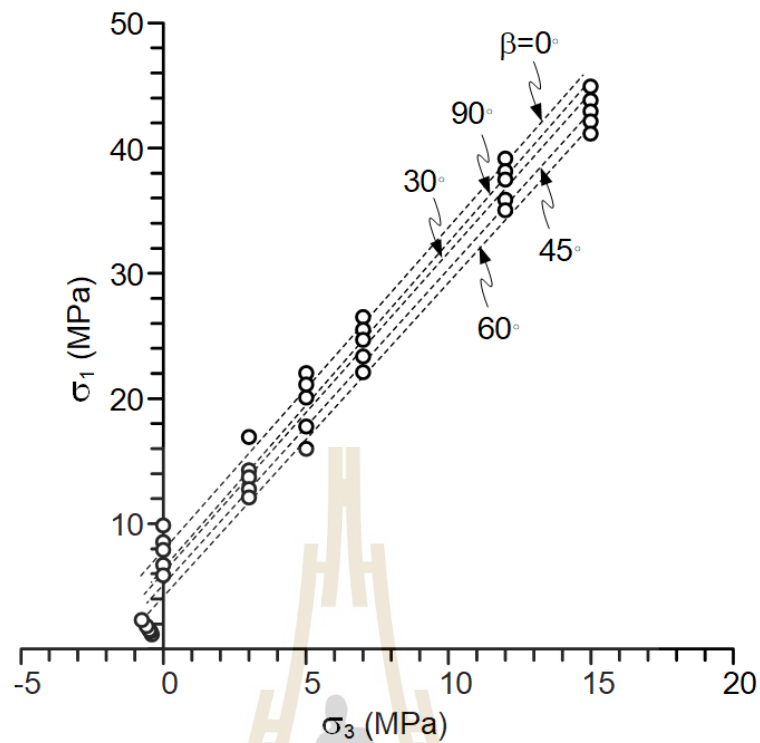


Figure 6.6 Major principal stresses at failure ($\sigma_{1,f}$) as a function of confining pressure (σ_3). Lines are Coulomb criterion.

The strength parameters can be determined by regression analysis of the compressive and tensile strength data. The cohesion and friction angles for each angle are summarized in Table 6.2, and are plotted as a function of the bedding plane orientation in Figure 6.7. The results indicate that the friction angles tend to be independent of the angle β , where their average value is 26 degrees. The cohesions, however, vary with the bedding plane orientation. The lowest cohesions are obtained from the specimens with $\beta = 60^\circ$, and the highest ones are from those with $\beta = 0^\circ$. A third-degree polynomial equation can best describe the relationship between the cohesions and angle β as:

$$c = c_0^\circ - 2.8 \times 10^{-3} \cdot \beta - 7 \times 10^{-7} \cdot \beta^2 + 8 \times 10^{-6} \cdot \beta^3 \quad (6.10)$$

where c_0° is the cohesion obtained from specimens with $\beta = 0$. Good correlation is obtained ($R^2 > 0.990$).

Table 6.2 Cohesions and friction angles for different bedding plane orientations.

β (Degrees)	Cohesion, c (MPa)	Friction angle, f (Degrees)	R^2
0	2.47	26	0.985
30	1.92	26	0.988
45	1.57	26	0.993
60	1.33	25	0.994
90	2.00	26	0.977

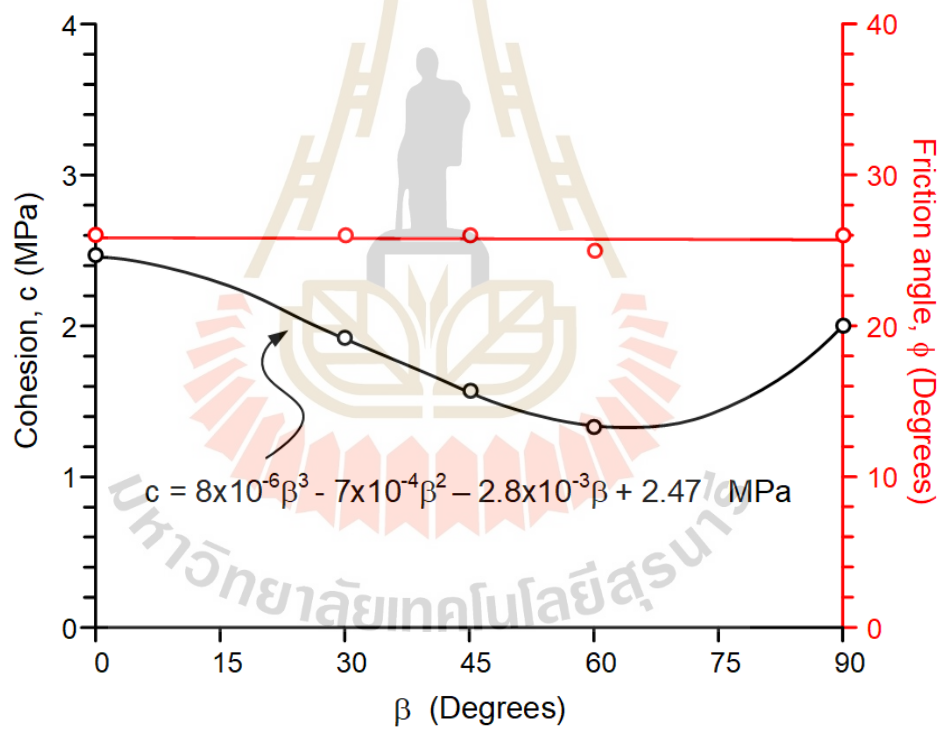


Figure 6.7 Cohesions and friction angles as a function of bedding plane orientation.

The bedding plane angle at minimum strength is associated with the friction angle. Theoretically, the plane of weakness is associated with the failure of bedding plane. The lowest strength is related to the bedding plane angle of $45^\circ + (\phi/2)$, as shown in Figure 6.8. The lowest strengths of gypsum in this study ($\beta = 60^\circ$) are obtained at weakness orientation ($\beta_w = 58^\circ$). It can be concluded that when $\beta = 60^\circ$, the fracture is easily sheared and slipped on the plane of weakness.

6.6 Strength criterion based on strain energy density

In order to consider both stresses and strains, the strain energy principle is applied to describe the gypsum failure under different bedding plane orientations. Distortional strain energy (W_d) and mean strain energy (W_m) at failure are calculated for each specimen using the following equations (Jaeger et al. 2007):

$$W_d = (3/2) \cdot \tau_{\text{oct}, f} \cdot \gamma_{\text{oct}, f} \quad (6.11)$$

$$W_m = (3/2) \cdot \sigma_{m, f} \cdot \epsilon_{m, f} \quad (6.12)$$

where $\tau_{\text{oct}, f}$ and $\gamma_{\text{oct}, f}$ are octahedral shear stress and strain at failure, and $\sigma_{m, f}$ and $\epsilon_{m, f}$ are mean stress and mean strain. They are calculated by:

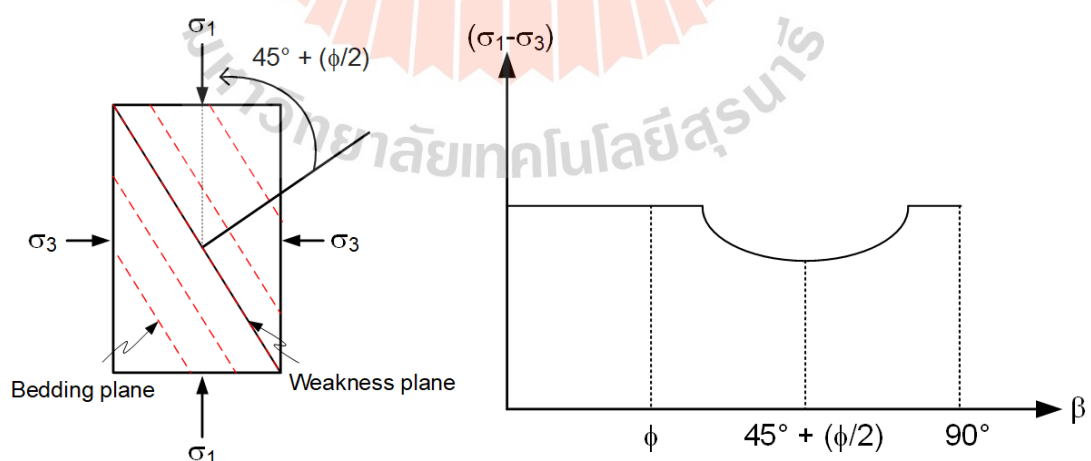


Figure 6.8 Effect of anisotropy on critical stress state values (Hudson and Harrison, 1997).

$$\tau_{\text{oct},f} = (1/3)[2(\sigma_{1,f} - \sigma_3)^2]^{1/2} \quad (6.13)$$

$$\gamma_{\text{oct},f} = (1/3)[(\epsilon_{1,f} - \epsilon_{3P,f})^2 + (\epsilon_{1,f} - \epsilon_{3O,f})^2 + (\epsilon_{3P,f} - \epsilon_{3O,f})^2]^{1/2} \quad (6.14)$$

$$\sigma_{m,f} = (\sigma_{1,f} + 2\sigma_3)/3 \quad (6.15)$$

$$\epsilon_{m,f} = (\epsilon_{1,f} + \epsilon_{3P,f} + \epsilon_{3O,f})/3 \quad (6.16)$$

where $\epsilon_{1,f}$, $\epsilon_{3P,f}$, and $\epsilon_{3O,f}$ are principal strains at failure.

The test results show that the distortional strain energy increases linearly with the mean strain energy for all bedding plane orientations (Figure 6.9). Linear equation is proposed to represent W_d as a function of W_m :

$$W_d = \delta \cdot W_m + \alpha \quad (6.17)$$

where δ represents slope of W_d - W_m relations, and α is W_d for $W_m = 0$. Correlation coefficients (R^2) are greater than 0.990. The diagram indicates that the W_d - W_m relation obtained at $\beta = 60^\circ$ shows the lowest value but gives the steepest slope ($\delta = 1.611$). As a result, the higher W_d - W_m relations for $\beta = 45^\circ$, 30° , 90° and 0° would terminate on the 60° W_d - W_m relation at $W_m = 0.063$, 0.064 , 0.079 and 0.088 MPa, respectively. It seems that, W_d for $\beta = 60^\circ$ continues to increase linearly with W_m beyond these termination points, suggesting that it would be able to describe the gypsum strength from transverse isotropic to isotropic behavior. The W_d - W_m failure criterion agrees well with those of the Coulomb criterion proposed earlier. Both suggest that gypsum failure and deformability obtained for $\beta = 60^\circ$, where it exhibits the lowest strength, can be extended to the condition where it mechanically responds as isotropic material under higher confinement beyond the range tested here.

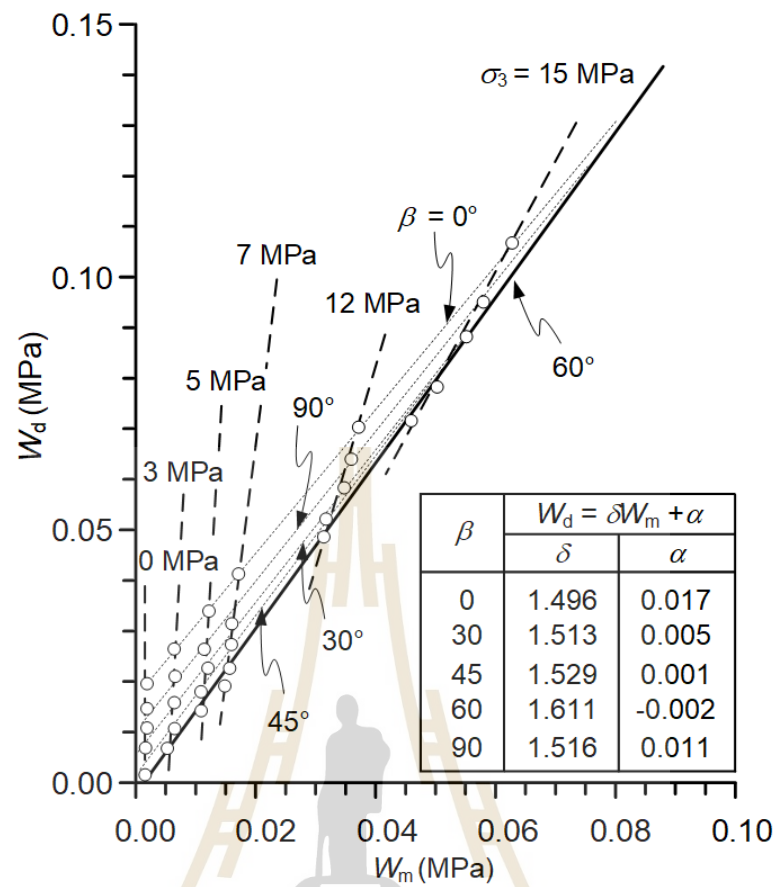


Figure 6.9 Distortional strain energy (W_d) at failure as a function of mean strain energy (W_m).

CHAPTER VII

NUMERICAL MODELLING

7.1 Introduction

The objective of this chapter is to demonstrate the effect of transverse isotropy on stability conditions of slope forming by bedding planes. The simulations use Phase^{2D} program. The factor of safety of rock slope is calculated under different bedding plane angles and slope angles.

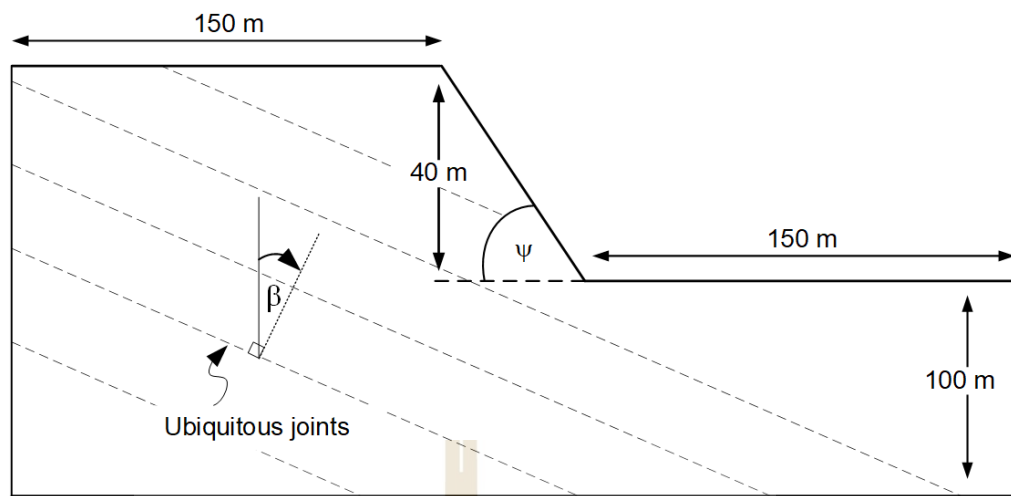
7.2 Numerical modelling

The finite element model is formulated in Phase^{2D} program. Coulomb criterion is used to determine the stability of slope with different bedding plane angles by creating the ubiquitous joint model. The ubiquitous joint model is commonly used to represent the discontinuous nature of a naturally global occurring response of anisotropic and foliated rock masses, while does not consider the effects of joint spacing, length, and stiffness.

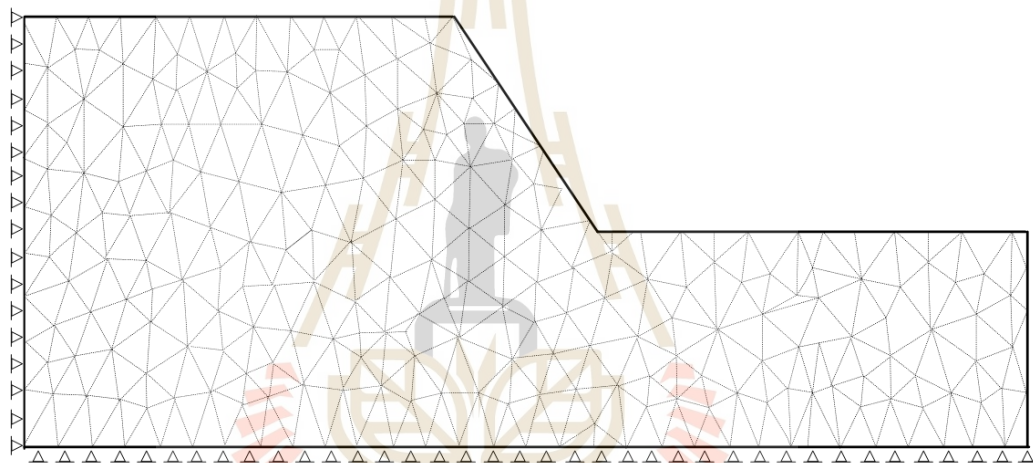
The slope model having height of 40 m is selected as a case study. The slope geometry is shown in Figure 7.1. The slope angles (ψ) vary from 60°, 70°, 80°, to 90°. In the model, ubiquitous joints are represented as the bedding planes. Bedding plane angles (β) vary from 0° to 90°, with an interval of 15°. The models are discretized using uniform three noded triangular meshing elements. The fixed boundary conditions are assumed at the base and left side of the model which restricts displacement in x and y-directions. The analysis is performed considering gravity load only, which represents the main driving force (Figure 7.1b).

7.3 Material properties

The material properties are obtained from those of the compression test under unconfined and Brazilian tension test. The material parameters are divided into two parts: (1) intact rock is represented by the specimen at angle $\beta = 0^\circ$, and (2) the ubiquitous joint is simulated by the specimen at angle $\beta = 60^\circ$. The intact rock is



(a)



(b)

Figure 7.1 Geometry of the rock slope (a) and finite element mesh and boundary condition (b).

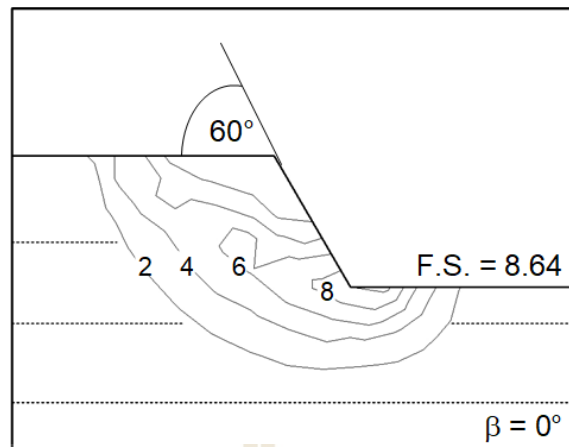
assumed to have high strength parameters as compared to the ubiquitous joint. The material parameters are given in Table 7.1.

7.4 Numerical results

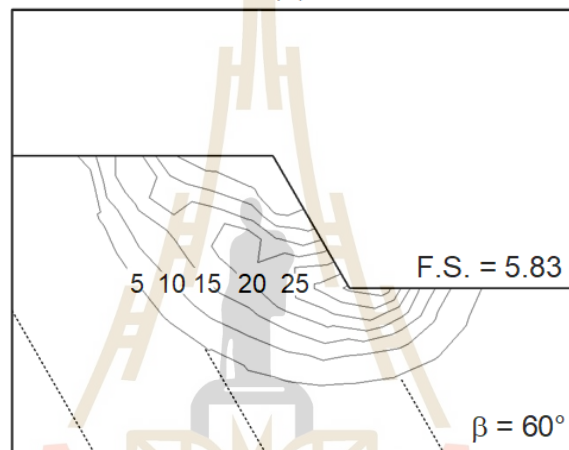
Regarding the prediction of the sliding mechanism of slope, the contours of the maximum shear strain obtained via Phase^{2D} is presented in Figures 7.2 through 7.5. It can be observed that the maximum shear strain and factor of safety change with bedding plane angles. The factor of safety increase as the slope angle increases. The results are carried out by strength reduction method using Mohr-Coulomb parameters to determine the factor of safety. Figure 7.6 plots the factors of safety as a function of bedding plane angle. The results indicate that the factor of safety decreases with the increase of the slope angle. For all slope angles, the factor of safety shows trend of initial decrease and later increase. When the angle $\beta = 60^\circ$, the factor of safety is the smallest which corresponds to the largest slope displacements (Figures 7.7 through 7.10). The numerical model results agree well with those results obtained from compression test that the orientations of transverse isotropic plane do affect the strength of rock.

Table 7.1 Material parameters used for numerical modelling.

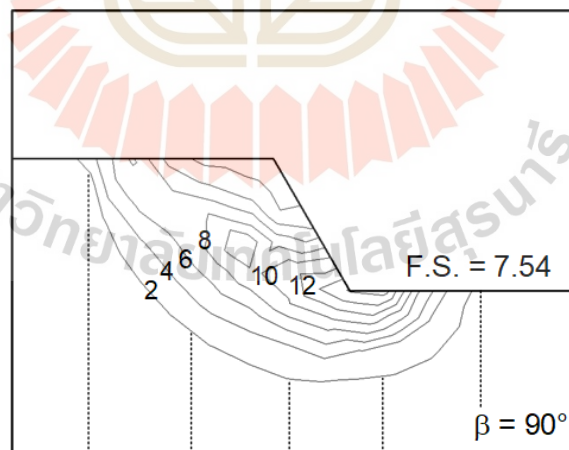
Properties		Intact rock	Ubiquitous joint
Unit weight (g/cc)		2.25	-
Elastic properties (Transversely isotropic)	E (GPa)	8.02	-
	E' (GPa)	3.34	-
	G' (GPa)	1.71	-
	ν	0.20	-
	ν'	0.26	-
Strength parameters	s_t (MPa)	0.77	-
	Cohesion (MPa)	2.47	1.34
	Friction angle	26°	26°



(a)



(b)



(c)

Figure 7.2 Contours of maximum shear strain with $\beta = 0^\circ$ (a), 60° (b), and 90° (c) at the slope face of 60° .

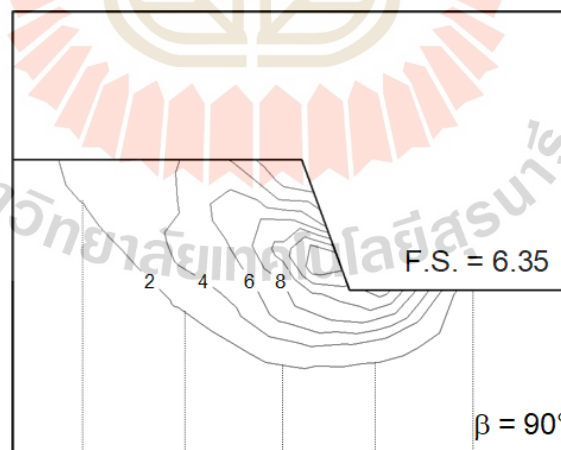
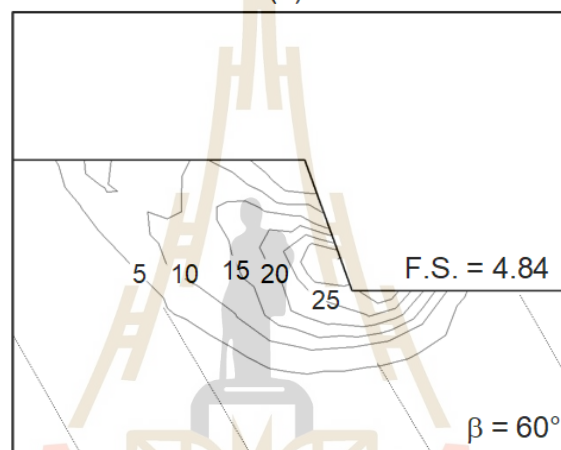
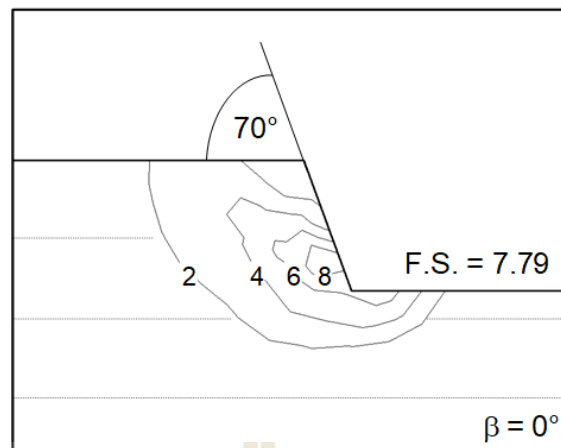


Figure 7.3 Contours of maximum shear strain with $\beta = 0^\circ$ (a), 60° (b), and 90° (c) at the slope face of 70° .

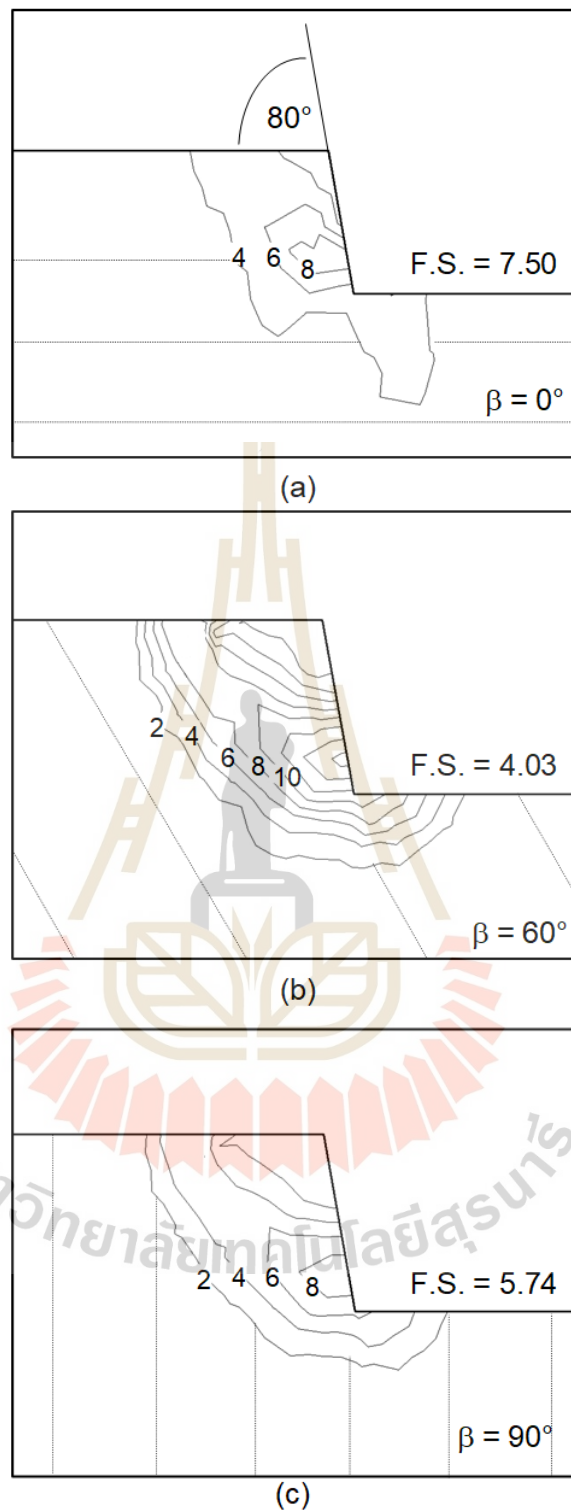


Figure 7.4 Contours of maximum shear strain with $\beta = 0^\circ$ (a), 60° (b), and 90° (c) at the slope face of 80° .

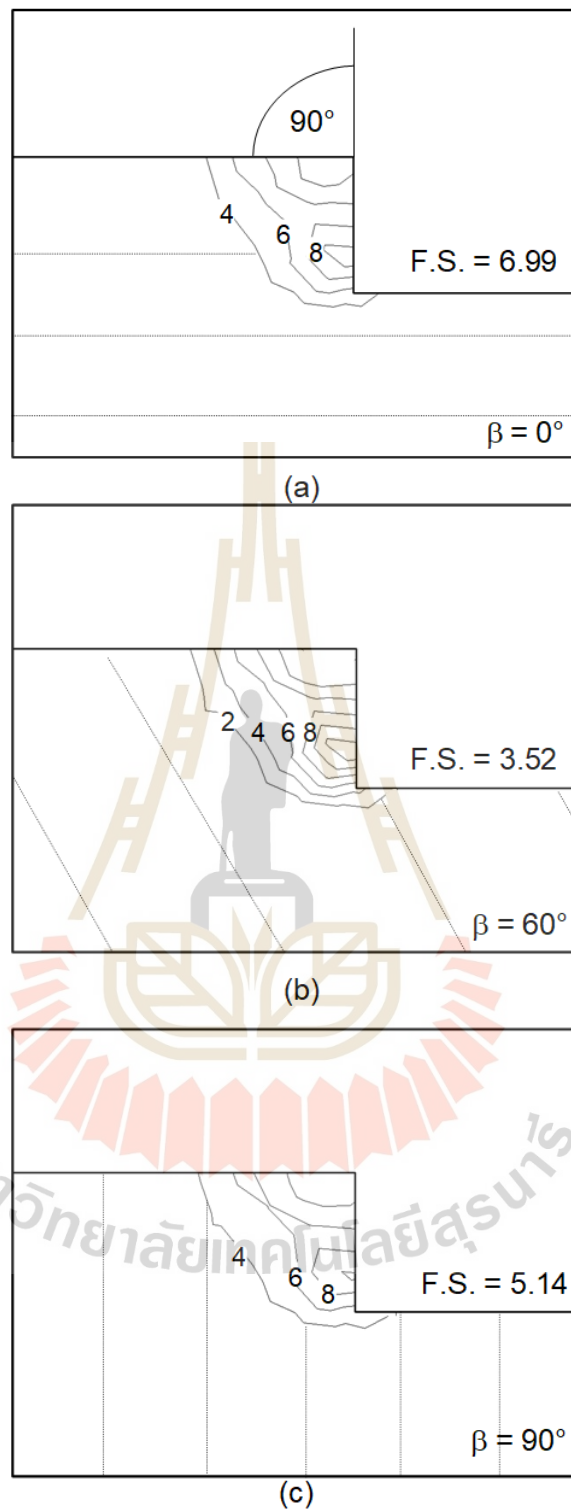


Figure 7.5 Contours of maximum shear strain with $\beta = 0^\circ$ (a), 60° (b), and 90° (c) at the slope face of 90° .

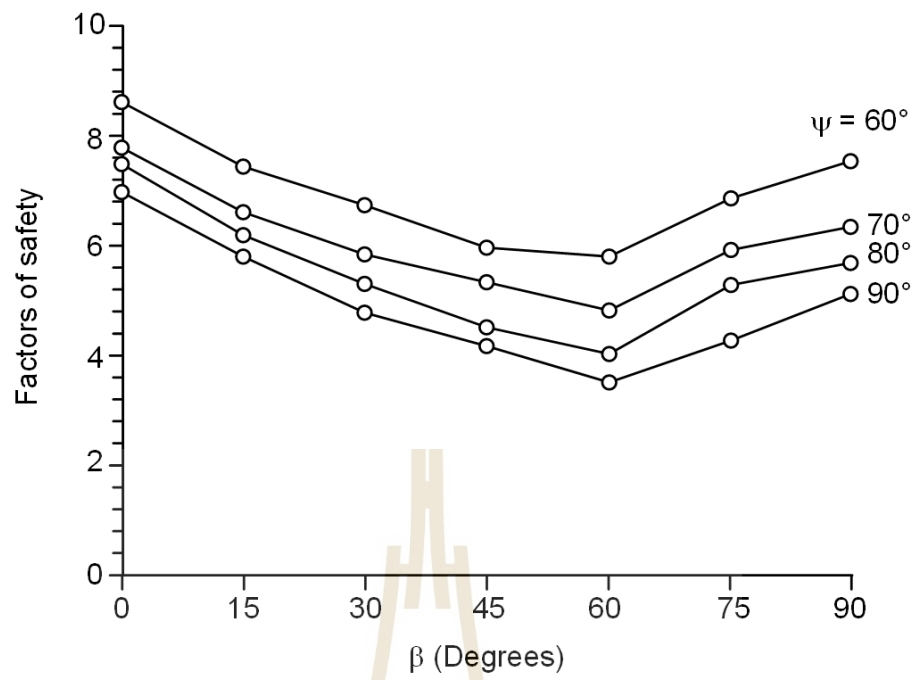


Figure 7.6 Factors of safety as a function of bedding plane orientations.

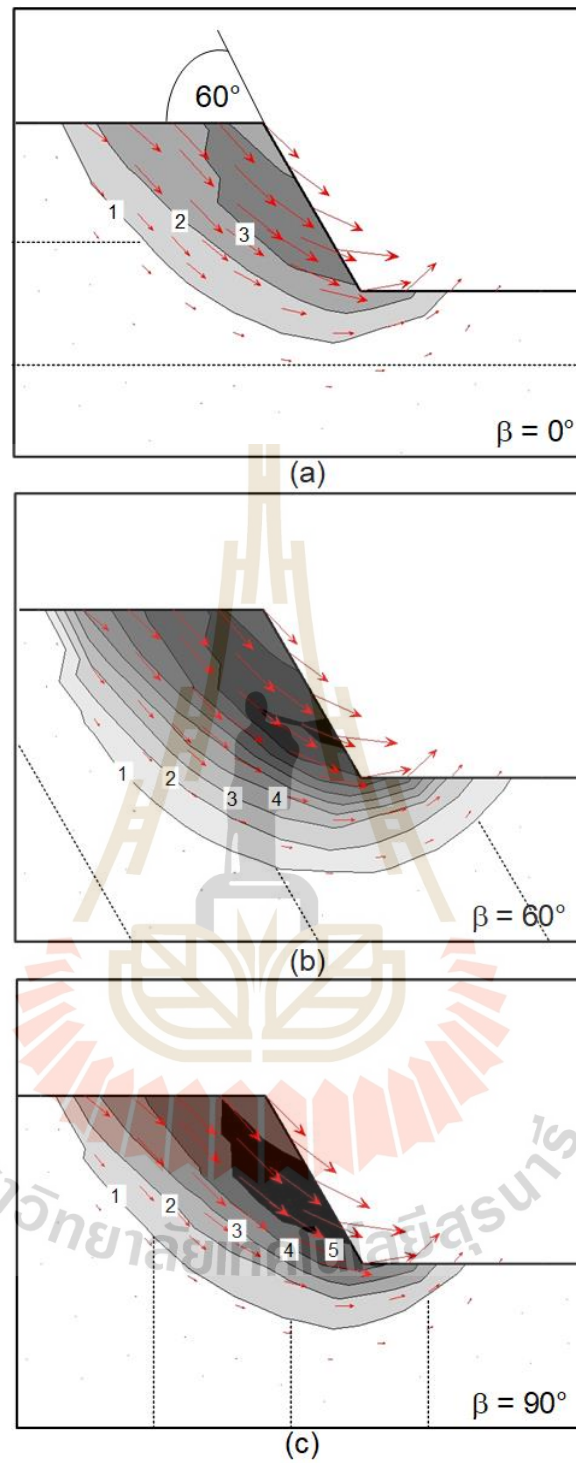


Figure 7.7 Contours of slope displacements (centimeter) with $\beta = 0^\circ$ (a), 60° (b), and 90° (c) at the slope face of 60° .

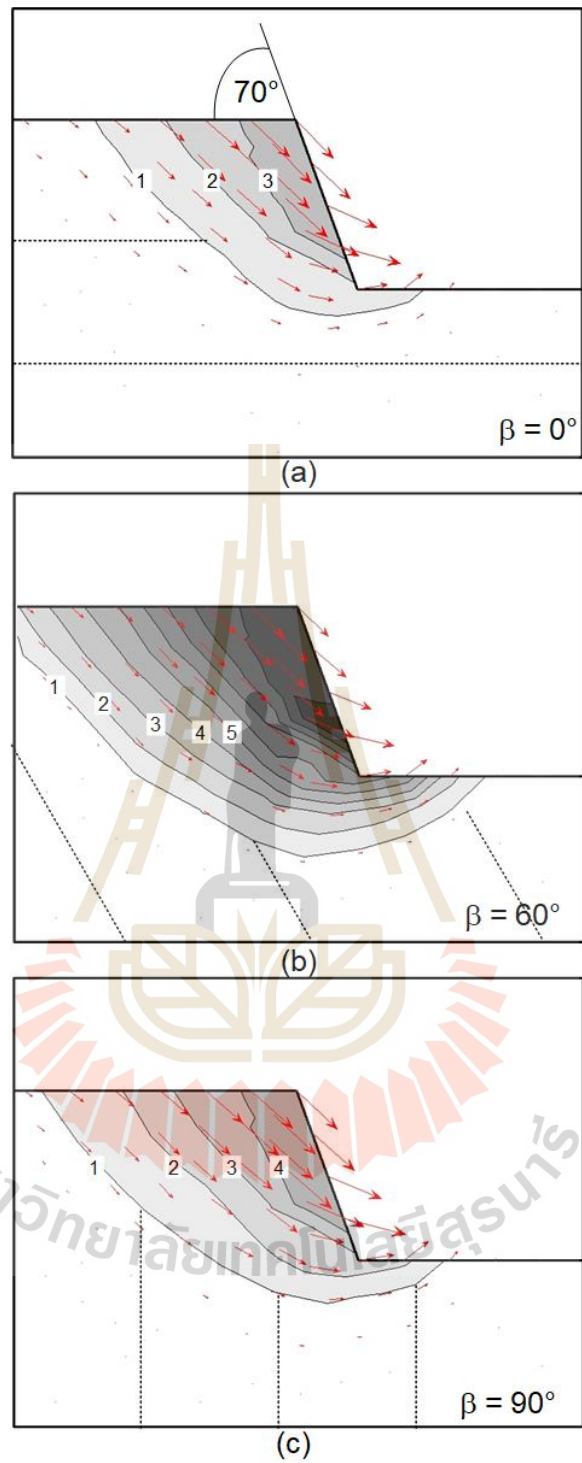


Figure 7.8 Contours of slope displacements (centimeter) with $\beta = 0^\circ$ (a), 60° (b), and 90° (c) at the slope face of 70° .

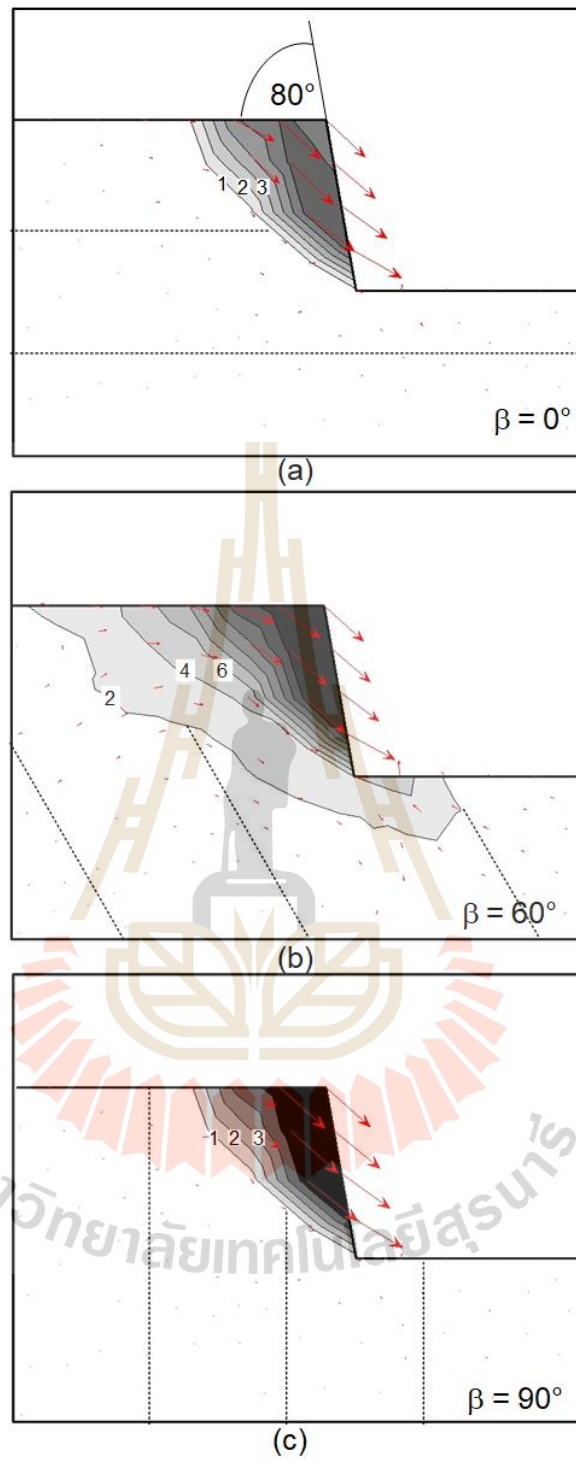


Figure 7.9 Contours of slope displacements (centimeter) with $\beta = 0^\circ$ (a), 60° (b), and 90° (c) at the slope face of 80° .

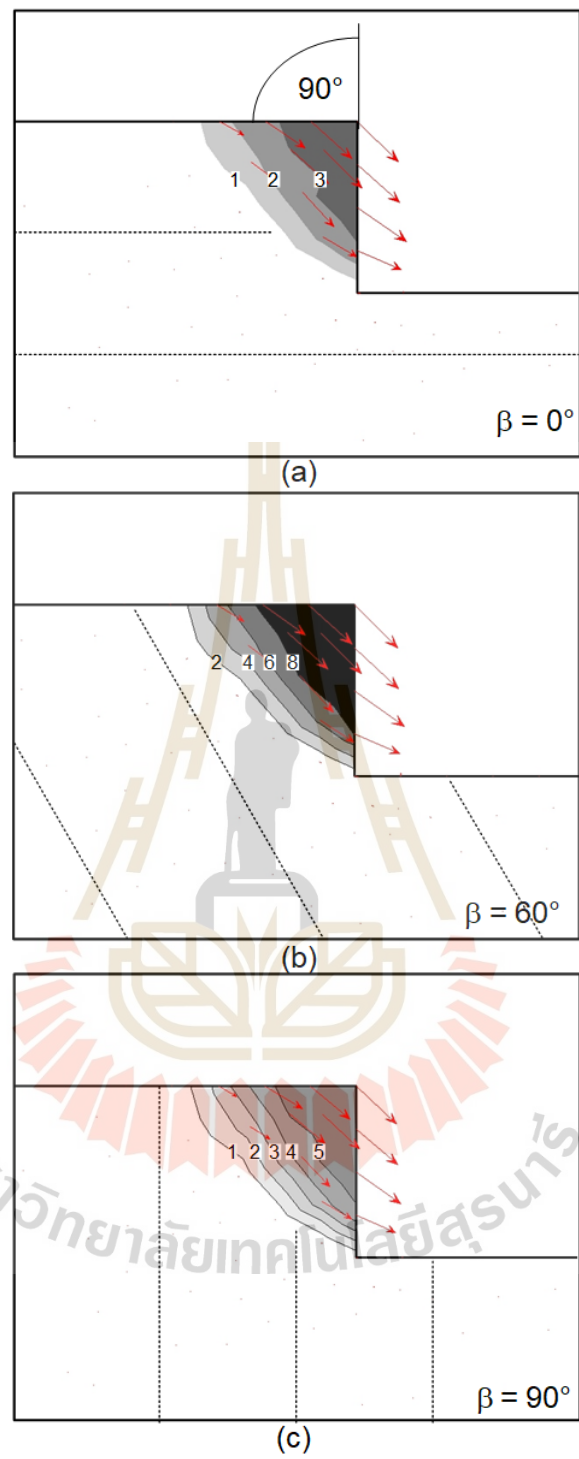


Figure 7.10 Contours of slope displacements (centimeter) with $\beta = 0^\circ$ (a), 60° (b), and 90° (c) at the slope face of 90° .

CHAPTER VIII

DISCUSSIONS AND CONCLUSIONS

8.1 Discussions

In this study, transverse isotropy behavior of gypsum collected from open pit mine in Nakhon Sawan province is studied through laboratory testing. Ultrasonic pulse velocity measurements, triaxial compression, and Brazilian tension tests are carried out on specimens with different bedding plane orientations. Numerical simulation is performed demonstrate the effect of transverse isotropy on rock slope stability.

Both P- and S-wave velocities increase linearly with increasing bedding plane angle from normal to parallel to the wave direction. The wave velocity is minimum when the wave propagates normal to the bedding plane ($\beta = 0^\circ$). It is maximum when the wave propagates parallel to the bedding plane ($\beta = 90^\circ$). This is because of the reflection and refraction of the wave velocity and interface of the bedding plane, which results in wave energy loss. Larger bedding plane angles have fewer interfaces and higher wave velocity. The results obtained from this study agree well with those of Abbas et al. (2020) and Wang and Han (2020) who study the wave velocity as affected by bedding plane orientation.

The compressive and tensile strength tests indicate that the maximum compressive strengths corresponding to the bedding angle (β) equal to 0° are highest for all confining pressures. The minimum strength is obtained at $\beta = 60^\circ$. All bedding plane orientations show the strength increase with increasing confining pressures. When the confining pressure increases, the difference between the maximum ($\beta = 0^\circ$) and minimum ($\beta = 60^\circ$) strengths decreases. The tensile strengths decrease as the bedding plane angle increases. This is due to the failure behavior of specimens. The bedding planes easily slip due to shearing under compression for $\beta = 60^\circ$ and they spit due to tension under $\beta = 90^\circ$.

The elastic modulus parallel to the bedding plane (E) is always higher than the elastic modulus normal to the bedding plane (E') under both compression and tension

conditions. According to Amadei (1987), the degree of anisotropy in the form of the maximum-to-minimum elastic moduli ratio (E/E') can be determined. The degree of anisotropy decreases as the confining pressure increase and may reach the isotropic behavior under larger confinement. This is maybe because the pore space along bedding planes is compacted by confining pressure. The results agree well with those from various rocks obtained elsewhere, as compared in Figure 8.1.

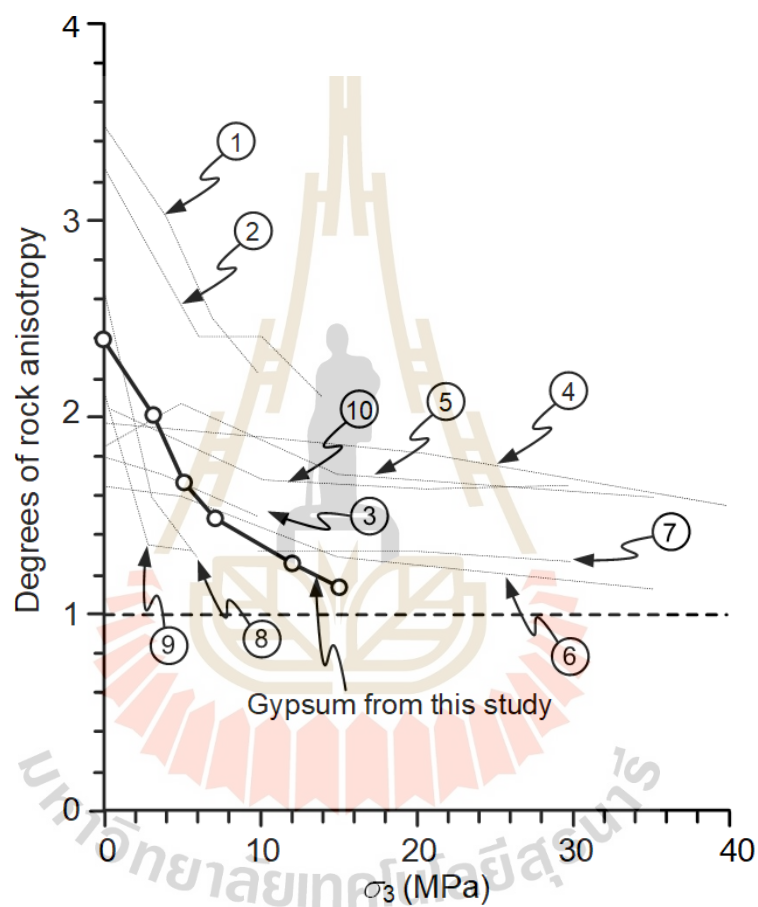


Figure 8.1 Degrees of rock anisotropy (E/E') as a function of confining pressure. ① Hornfel, ② Schist, ③ Garnet hornfel (Fereidooni et al., 2016); ④ Mudstone (Miller et al., 2013); ⑤ Quartzitic schist, ⑥ Biotite schists (Nasseri et al., 2003); ⑦ Phyllite (Xu et al., 2018); ⑧ Meta-siltstone, ⑨ Schist (Usoltseva et al., 2017); ⑩ Sandstone (Hu et al., 2017).

The Coulomb criterion and strain energy density equation show that the friction angles tend to be independent of the bedding plane orientation, where their average value is 26 degrees. The cohesions, however, vary with the bedding plane angles. The distortional strain energy (W_d) increases linearly with the mean strain energy (W_m). The W_d - W_m relation obtained at $\beta = 60^\circ$ shows the lowest trend. Both Coulomb criterion and W_d - W_m relation suggest that the gypsum failure and deformability obtained for $\beta = 60^\circ$, where it exhibits the lowest strength, can be extended to the condition where it mechanically responds as isotropic material under higher confinement beyond the range tested here.

According to the simulations of anisotropic rock slope, the factor of safety decreases gradually as the bedding plane angles increase from 0° to 60° . Then, the factor of safety increases as the bedding plane angle increases from 75° to 90° . The lowest factor of safety is obtained when the bedding plane angle is 60° for all slope angles.

8.2 Conclusions

The effect of transverse isotropy on mechanical properties of gypsum is investigated based on wave velocity, generalized Hooke's law, Coulomb criterion, and strain energy density principle. The following conclusions are drawn.

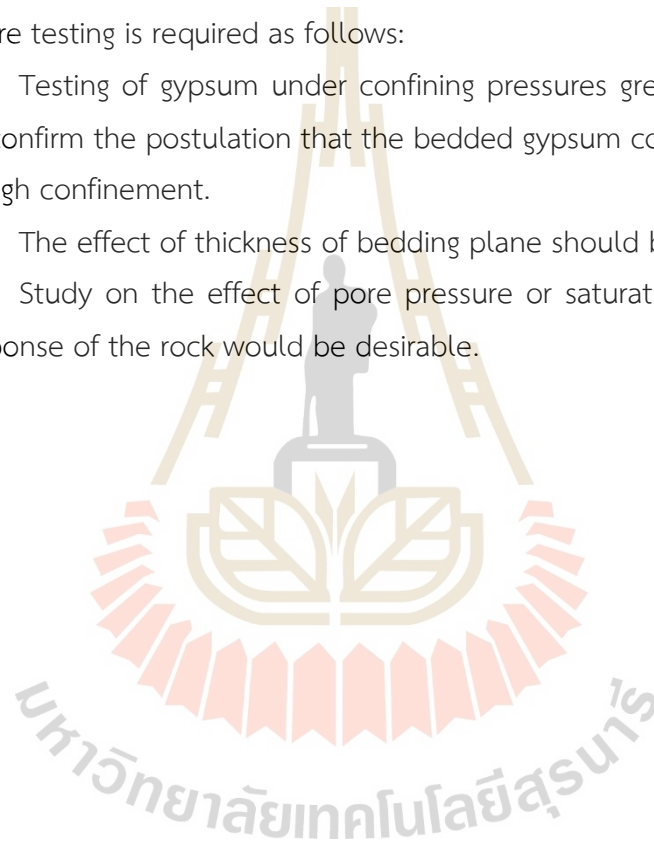
- 1) Wave velocity increases linearly as the bedding plane angles increase from 0° to 90° .
- 2) Compressive strength perpendicular to bedding plane ($b = 0^\circ$) is greater strength than that parallel to the bed ($b = 90^\circ$). The minimum strength is obtained at $b = 60^\circ$. Tensile strength decreases as bedding plane angles increase from normal to parallel with the loading direction.
- 3) Elastic modulus parallel to the bedding plane is always higher than the elastic modulus normal to the bedding plane as suggested by dynamic, compression, and tensile elastic modulus measurements. The apparent elastic moduli agree well with those predicted by Amadei's solutions ($R^2 = 0.989$).
- 4) Increasing the confining pressure decrease the effect of transverse isotropy on strength and elastic modulus of the gypsum. The gypsum tends to behave more isotropic material under increasing confinement. This is probably because the pore spaces in bedding planed are compacted by confining pressure.

5) The slope stability depends on the bedding plane angle. The results suggest that when the bedding plane angle is 60° and dips to the slope face direction, the slope face angle should be more gentle which should lead to sufficiently high factor of safety.

8.3 Recommendations for future studies

The uncertainties of the investigation and results discussed above lead to the recommendations for further studies. To confirm the conclusions drawn in this research, more testing is required as follows:

- 1) Testing of gypsum under confining pressures greater than those used here would confirm the postulation that the bedded gypsum could become isotropic under very high confinement.
- 2) The effect of thickness of bedding plane should be investigated.
- 3) Study on the effect of pore pressure or saturation on the transverse isotropic response of the rock would be desirable.



REFERENCES

- Abbass, H. A., Mohamed, Z., and Yasir, S. F. (2018). A review of methods, techniques and approaches on investigation of rock anisotropy. In **Proceedings of the American Institute of Physics (AIP) Conference** (pp. 020012-1 – 020012-8). Penang, Malaysia.
- Amadei, B. (1996). Importance of anisotropy when estimating and measuring in situ stresses in rock. **International Journal of Rock Mechanics and Mining Sciences & Geomechanics Abstracts**. 33(3): 293-325.
- Amadei, B., Savage, W. Z., and Swolfs, H. S. (1987). Gravitational stresses in anisotropic rock masses. **International Journal of Rock Mechanics and Mining Sciences & Geomechanics Abstracts**. 24: 5-14.
- ASTM C97 (2015). **Standard Test Methods for Absorption and Bulk Specific Gravity of Dimension Stone**. Annual Book of ASTM Standards, American Society for Testing and Materials, West Conshohocken, PA.
- ASTM D2845-08 (2008). **Standard Test Method for Laboratory Determination of Pulse Velocities and Ultrasonic Elastic Constants of Rock**. Annual Book of ASTM Standards, American Society for Testing and Materials, West Conshohocken, PA.
- ASTM D3967-16 (2016). **Standard Test Method for Splitting Tensile Strength of Intact Rock Core Specimens**. Annual Book of ASTM Standards, American Society for Testing and Materials, West Conshohocken, PA.
- ASTM D7012-14e1 (2014) **Standard Test Methods for Compressive Strength and Elastic Moduli of Intact Rock Core Specimens under Varying States of Stress and Temperatures**. Annual Book of ASTM Standards, American Society for Testing and Materials, West Conshohocken, PA.
- Berčáková, A., Melichar, R., and Souček, K. (2020). Mechanical properties and failure patterns of migmatized gneiss with metamorphic foliation under UCS test. **Rock Mechanics and Rock Engineering**. 53: 2007-2013.

- Byun, B. S. (1984). Seismic parameters for transversely isotropic media. **Geophysics**. 49(11): 1908-1914.
- Byun, B.S. and Cheng, S.C.W. (1986). Apparent axial properties of transversely isotropic media. **Geophysics**. 51(4): 1012-1013.
- Chamwan, S. (2020). Correlations between ultrasonic pulse velocities and mechanical properties of rocks. **Master thesis**, Suranaree University of Technology, Nakhon Ratchasima.
- Cheng, C., Li, X., and Qian, H. (2017). Anisotropic failure strength of shale with increasing confinement: behaviors, factors and mechanism. **Materials**. 10(11).
- Clark, I. (2006) Simulation of rock mass strength using ubiquitous-joints. In **Proceedings of the 4th international FLAC symposium on numerical modeling in geomechanics-2006** (pp. 07-08). Madrid, Spain.
- Crampin, S. (1981). A review of wave motion in anisotropic and cracked elastic-media. **Wave Motion**. 3(4): 343-391.
- Dehler, W. and Labuz, J.F. (2007). Stress path testing of an anisotropic sandstone. **Journal of Geotechnical and Geoenvironmental Engineering**. 133(1): 116-119.
- Fereidooni, D., Khanlari, G., Heidari, M., Sepahi, A.A., and Kolahi-Azar, A.P. (2016). Assessment of inherent anisotropy and confining pressure influences on mechanical behavior of anisotropic foliated rocks under triaxial compression. **Rock Mechanics and Rock Engineering**. 49: 2155–2163.
- Grgic, D., Giraud, A., and Schoumacker, L. (2019). Dynamic anisotropic elastic properties of a claystone under variable loading direction and saturation. **Geophysical Journal International**. 216(1): 148-163.
- Hao, X., Wang, S., Xu, Q., Yang, D., Zhang, Q., Jin, D., and Wei, Y. (2020). Influences of confining pressure and bedding angles on the deformation, fracture and mechanical characteristics of slate. **Construction and Building Materials**. vol. 243.
- Harrison, J.P. and Hudson, J.A. (2002). **Engineering Rock Mechanics: Part 2. Illustrative Worked Examples**. Elsevier, Netherlands.
- Heng, S., Guo, Y., Yang, C., Daemen, J. J., and Li, Z. (2015). Experimental and theoretical study of the anisotropic properties of shale. **International Journal of Rock Mechanics and Mining Sciences**. 74: 58-68.

- Hu, S., Tan, Y., Zhou, H., Guo, W., Hu, D., Meng, F., and Liu, Z. (2017). Impact of bedding planes on mechanical properties of sandstone. **Rock Mechanics and Rock Engineering**. 50(8): 2243-2251.
- Ismael, M. and Konietzky, H. (2017a). Integration of elastic stiffness anisotropy into ubiquitous joint model. **Procedia engineering**. 191: 1032-1039.
- Ismael, M., Chang, L., and Komietzky, H. (2017b). **Behavior of Anisotropic Rocks**. Geotechnical Institute, Freiberg University of Mining and Technology, Germany.
- Jaeger, J.C., Cook, N.G.W., and Zimmerman, R.W. (2007). **Fundamentals of Rock Mechanics**. Blackweel, Oxford. 475p.
- Khanlari, G., Rafiei, B., and Abdilor, T. (2014). Evaluation of strength anisotropy and failure modes of laminated sandstones. **Arabian Journal of Geosciences**. 8(5): 3089-3102.
- Kundu, J., Mahanta, B., Sarkar, K., and Singh, T. N. (2018). The effect of lineation on anisotropy in dry and saturated himalayan schistose rock under Brazilian test conditions. **Rock Mechanics and Rock Engineering**. 51(1): 5-21.
- Kuroda, J., Hara, H., Ueno, K., Charoentitirat, T., Maruoka, T., Miyazaki, T., Miyahigashi, A., and Lugli, S. (2017). Characterization of sulfate mineral deposits in central Thailand. **Island Arc**. 26(2).
- Leng, X., Wang, C., Sheng, Q., Chen, J., and Li, H. (2021). An enhanced ubiquitous-joint model for a rock mass with conjugate joints and its application on excavation simulation of large underground caverns. **Frontiers in Earth Science**. 9(765).
- Li, C., Xie, H., and Wang, J. (2020a). Anisotropic characteristics of crack initiation and crack damage thresholds for shale. **International Journal of Rock Mechanics and Mining Science**. vol. 126.
- Li, H., Jian, X., Li, G., Wu, P., Jia, H., Wang, Y., and Xu, M. (2020b). Effects of bedding structures on the propagation characteristics of acoustic waves in shales at operating frequencies of acoustic logging. **AIP Advances**. 10(8).
- Liao, J. J., Hu, T. B., and Chang, C. W. (1997). Determination of dynamic elastic constants of transversely isotropic rocks using a single cylindrical specimen. **International Journal of Rock Mechanics and Mining Sciences**. 34(7): 1045-1054.
- Ma, T., Peng, N., Zhu, Z., Zhang, Q., Yang, C., and Zhao, J. (2018). Brazilian tensile strength of anisotropic rocks: review and new insights. **Energies**. 11(2): 304.

- Mahjoub, M., Rouabhi, A., Tijani, M., and Granet, S. (2015). A damage model for transversely isotropic materials. In **Proceedings of the Petrus 2015 Conference** (pp. 46-53). France.
- Meng, L., Li, T., Liao, A., and Zeng, P. (2018). Anisotropic mechanical properties of sandstone under unloading confining pressure at high temperatures. **Arabian Journal for Science and Engineering**. 43(10): 5283-5294.
- Miller, D., Plumb, R., and Boitnott, G., (2013). Compressive strength and elastic properties of a transversely isotropic calcareous mudstone. **Geophysical Prospecting**. 61(2): 315-328.
- Mokhtari, M., Bui, B. T., and Tutuncu, A. N. (2014). Tensile failure of shales: impacts of layering and natural fractures. In **Proceedings of the SPE western north american and rocky mountain joint meeting**. Denver, Colorado.
- Nasseri, M.H.B., Rao, K.S., and Ramamurthy, T., (2002). Anisotropic strength and deformational behavior of Himalayan schists. **International Journal of Rock Mechanics and Mining Sciences**. 40(1): 3-23.
- Ramamurthy, T. (2010). **Engineering in Rocks for Slopes, Foundations and Tunnels**. Rajkamal Electric Press.
- Ramamurthy, T., Venkatappa, R.G., and Singh, J. (1993). Engineering behaviour of phyllites. **Engineering Geology**. 33: 209-225.
- Sainsbury, B. L. and Sainsbury, D. P. (2017). Practical use of the ubiquitous-joint constitutive model for the simulation of anisotropic rock masses. **Rock Mechanics and Rock Engineering**. 50(6): 1507-1528.
- Sainsbury, B., Pierce, M., and Mas Ivars, D. (2008) Analysis of caving behavior using a synthetic rock mass (SRM)-ubiquitous-joint rock mass (UJRM) modeling technique. In **Proceedings of the 1st southern hemisphere international rock mechanics symposium (SHIRMS)**. Nedlands, Australia.
- Saroglou, H. and Tsiambaos, G. (2008). A modified Hoek–Brown failure criterion for anisotropic intact rock. **International Journal of Rock Mechanics and Mining Science**. 45:223–234.
- Singh, J., Ramamurthy, T., and Rao, G.V. 1989. Strength anisotropies in rocks. **Indian Geotechnical Journal**. 19: 147–166.
- Singhal, B.B.S. and Gupta, R.P. (2010). **Applied Hydrogeology of Fractured Rocks**. Springer Science & Business Media, Germany.

- Utha-aroon, C. and Rattanajaruraks, P. (1996). A new concept in gypsum geology of Thailand. In **Proceedings of the Annual Technical Meeting** (pp. 1-11). Thailand.
- Song, I. and Suh, M. (2014). Effects of foliation and microcracks on ultrasonic anisotropy in retrograde ultramafic and metamorphic rocks at shallow depths. **Journal of Applied Geophysics**. 109: 27-35.
- Song, I., Suh, M., Woo, Y. K., and Hao, T. (2004). Determination of the elastic modulus set of foliated rocks from ultrasonic velocity measurements. **Engineering Geology**. 72(3-4): 293-308.
- Tan, X., Konietzky, H., Frühwirt, T., and Dan, D. Q. (2015). Brazilian tests on transversely isotropic rocks: laboratory testing and numerical simulations. **Rock Mechanics and Rock Engineering**. 48(4): 1341-1351.
- Tsvankin, I., 2001. **Seismic Signatures and Analysis of Reflection Data in Anisotropic Media**. Pergamon Press. 436p.
- Turner, F.J. and Weiss, L.E. (1963). **Structural Analysis of Metamorphic Tectonites**. McGraw-Hill, New York.
- Usoltseva, O.M., Tsoi, P., and Semenov, V.N. (2017). Effects of structure on deformation and strength characteristics of transversely isotropic man-made geomaterials. In **Proceedings of the IOP Conference Series: Earth and Environmental Science** (vol. 53). Novosibirsk, Russia.
- Vales, F., Nguyen-Minh, D., Gharbi, H., and Rejeb, H. (2004). Experimental study of the influence of the degree of saturation on physical and mechanical properties in Tournemire shale (France). **Applied Clay Science**. 26(1-4): 197-207.
- Vervoort, A., Min, K. B., Konietzky, H., Cho, J. W., Debecker, B., Dinh, Q. D., Frühwirt, T., and Tavallali, A. (2014). Failure of transversely isotropic rock under Brazilian test conditions. **International Journal of Rock Mechanics and Mining Sciences**. 70: 343-352.
- Walhstrom, E. E. (1973). **Tunnelling in Rock**. Elsevier, Amsterdam.
- Wang, M., Li, P., Wu, X., and Chen, H. (2016). A study on the brittleness and progressive failure process of anisotropic shale. **Environmental Earth Sciences**. 75(10): 1-7.
- Wang, S. Y., Sloan, S. W., Tang, C. A., and Zhu, W. C. (2012). Numerical simulation of the failure mechanism of circular tunnels in transversely isotropic rock masses. **Tunnelling and Underground Space Technology**. 32: 231-244.

- Wang, Y. and Han, J.Q. (2020). Geomechanical and ultrasonic characteristics of black shale during triaxial deformation revealed using real-time ultrasonic detection dependence upon bedding orientation and confining pressure. **Geotechnical and Geological Engineering**. 38(6): 6773-6794.
- Wendai, L. 2000. **Regression Analysis, Linear Regression and Probit Regression, In 13 chapters**. SPSS for Windows: statistical analysis: Publishing House of Electronics Industry, Beijing, China.
- Wu, Q., Kou, Z., and Wan, S. (2012). Numerical Simulation for the Effect of Joint Inclination to the Stability of Stratified Rock Slope. In **Proceedings of the 2012 International Conference on Computer Application and System Modeling**. Atlantis Press.
- Xiao W.M., Deng, R.G., Zhong, Z.B., Fu, X.M., and Wang, C.Y. (2014). Experimental study on the mechanical properties of simulated columnar jointed rock masses. **Journal of Geophysics and Engineering**. 12: 80–89.
- Xu, G., He, C., and Chen, Z. (2019). Mechanical behavior of transversely isotropic rocks with non-continuous planar fabrics under compression tests. **Computers and Geotechnics**. vol. 115.
- Xu, G., He, C., Su, A., and Chen, Z. (2018). Experimental investigation of the anisotropic mechanical behavior of phyllite under triaxial compression. **International Journal of Rock Mechanics and Mining Sciences**. 104: 100-112.
- Yang, S.Q., Yin, P.F., Huang, Y.H., and Change, J.L. (2019). Strength, deformability and X-ray micro-CT observations of transversely isotropic composite rock under different confining pressures. **Engineering Fracture Mechanics**. 214: 1-20.
- Yaşar, E. (2001). Failure and failure theories for anisotropic rocks. In **Proceedings of the 17th International Mining Congress and Exhibition of Turkey-IMCET** (pp. 417-424). Ankara, Turkey.
- Zhang, C.L., Armand, G., and Conik, N. (2015). Investigation on the Anisotropic Mechanical Behaviour of the Callovo Oxfordian Clay Rock. **Technical Report**, prepared under contract No. 059844 with The French National Agency for Radioactive Waste Management (ANDRA). French.
- Zhou, S. H., Zhou, S. K., Zhang, J. C., and Tan, X. (2021). Effect of bedding orientation and spatial variability of stratification shear strength on stability of transversely isotropic rock slope. **Frontiers in Physics**. vol. 9.

BIOGRAPHY

Miss Laksikar Sitthimongkol was born on September 6, 1989 in Chiang Rai Province, Thailand. She received her Bachelor's Degree in Engineering (Geotechnology) from Suranaree University of Technology in 2017 and received her Master's Degree in Engineering (Geotechnology) from Suranaree University of Technology in 2019. For her post-graduate, she continued to study with a Doctor of Philosophy Program in the Geological Engineering Program, Institute of Engineering, Suranaree university of Technology. During graduation, 2017-2022, she was a part time worker in position of research associate at the Geomechanics Research Unit, Institute of Engineering, Suranaree University of Technology.

